Development of an Actively Cooled Large Aperture Laser Amplifier at the GSI Helmholtzzentrum

Patrizio, Marco

(2020)

Development of an Actively Cooled Large Aperture Laser Amplifier at the GSI Helmholtzzentrum

Entwicklung eines aktiv gekühlten Laserverstärkers großer Apertur am GSI Helmholtzzentrum

Zur Erlangung des Grades eines Doktors der Naturwissenschaften (Dr. rer. nat.)
genehmigte Dissertation von Marco Patrizio aus Hanau
Tag der Einreichung: 31.10.2019, Tag der Prüfung: 16.12.2019
Darmstadt — D 17

1. Gutachten: Prof. Dr. Markus Roth
2. Gutachten: Priv. Doz. Dr. Vincent Bagnoud

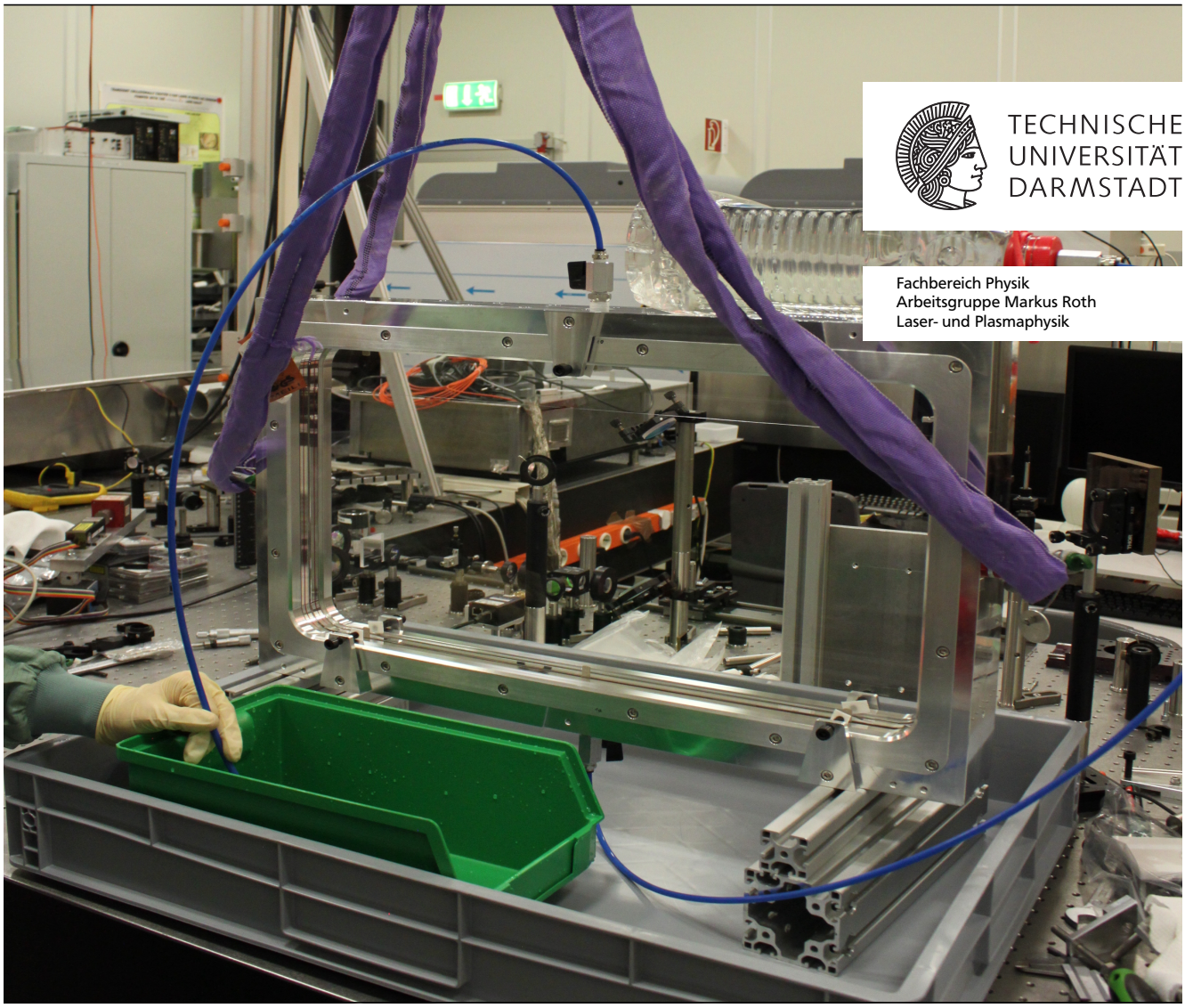

TECHNISCHE UNIVERSITÄT DARMSTADT

Fachbereich Physik
Arbeitsgruppe Markus Roth
Laser- und Plasmaphysik

Development of an Actively Cooled Large Aperture Laser Amplifier at the GSI Helmholtzzentrum
Entwicklung eines aktiv gekühlten Laserverstärkers großer Apertur am GSI Helmholtzzentrum

Genehmigte Dissertation von Marco Patrizio aus Hanau

1. Gutachten: Prof. Dr. Markus Roth
2. Gutachten: Priv. Doz. Dr. Vincent Bagnoud

Tag der Einreichung: 31.10.2019
Tag der Prüfung: 16.12.2019

Darmstadt — D 17

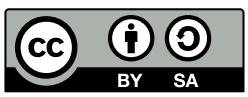

Erklärung gemäß §9 Promotionsordnung

Hiermit versichere ich, dass ich die vorliegende Dissertation selbstständig angefertigt und keine anderen als die angegebenen Quellen und Hilfsmittel verwendet habe. Alle wörtlichen und paraphrasierten Zitate wurden angemessen kenntlich gemacht. Die Arbeit hat bisher noch nicht zu Prüfungszwecken gedient.

Darmstadt, der 30. Oktober 2019

_____

(Marco Patrizio)

Zusammenfassung

Die Entwicklung von Lasern der Petawatt-Klasse über die letzten Jahrzehnte hat zu einer Reduktion von Größe und Preis der Systeme geführt. Diese Entwicklung begünstigte eine weltweite Verbreitung derartiger Laser an verschiedensten Anlagen zur Untersuchung von extremen Materiezuständen. Aufgrund der mit Petawatt Lasern erreichbaren Energiedichten, können diese für die Beschleunigung von Teilchen, als Treiber in der Trägheitsfusionsforschung und zur Strahlenterapie verwendet werden. Des Weiteren finden diese Systeme Anwendung als sekundäre Quellen zur Erzeugung von Röntgenstrahlung, Ionen, Elektronen, Protonen und Neutronen.

Dieses breite Anwendungsfeld führte zur Verwendung von Lasern der Petawatt-Klasse in staatlichen, sowie in universitären Einrichtungen. Hohe Repetitionsraten der Lasersysteme sind dabei sowohl für die Verwendung als direkte Quellen als auch als indirekte Quellen notwendig, um eine schnelle Reproduktion der Ergebnisse und belastbare Statistiken der Messdaten zu gewärleisten.
Während Niederenergie-Petawatt-Laser mit Pulsenergien unter 100 J bereits in kommerzieller Form zur Verfügung stehen und Repetitionsraten größer als 1 Hz bereitstellen, ist die Repetitionsrate von Hochenergie-Petawatt-Lasern mit Pulsenergien über 100 J durch das Kühlverhalten der verwendeten Verstärkermaterialien begrenzt. Die meisten Hochenergie-Petawatt Systeme verwenden in ihren Hauptverstärkerelementen auf Glas basierende Verstärkermedien mit Aperturen über 20 cm, um die auftretenden Intensitäten im System zu minimieren und der Beschädigung optischer Elemente vorzubeugen. Die niedrige Wärmeleitfähigkeit von Glas führt dabei zu thermischen Equilibrationszeiten der Verstärkermedien im Bereich von Stunden, welche mit einer niedrigeren Repetitionsrate korrespondieren.

Ziel dieser wissenschaftlichen Arbeit ist die Entwicklung eines glasbasierten Verstärkerelements für Hochenergie-Petawatt-Laser, welches über ein aktives Kühlverfahren die thermische Equilibrationszeit des Verstärkermediums reduziert um eine Verbesserung der Repetitionsrate des Lasers zu erreichen. Die angestrebten Repetitionsraten liegen dabei im Bereich von $1/5\,\mathrm{min}^{-1}$ bei einem Verstärkungsfaktor von 1.5, mit einem Fokus auf einer hohen Qualität und Reproduzierbarkeit der transmittierten Wellenfront.
Zu diesem Zweck wurde ein Konzept verwendet, welches einen laminaren Kühlmittelfluss zwischen zwei Verstärkerscheiben nutzt, um die thermische Last der Scheiben zu reduzieren.
Eine Reihe von Kühlmitteln wurde auf ihre thermischen, kinematischen, chemischen und optischen Eigenschaften untersucht, um ihre Eignung für die Verwendung im Prototypen zu bestimmen.
Weiterhin zeigten Simulationen des Kühlprozesses im Prototypen die Ausbildung eines Gleichgewichtzustands zwischen Erwärmung und Kühlung des Verstärkermediums. Dieser konnte genutzt werden, um in den Simulationen reproduzierbare Wellenfronten bei Repetitionsraten von $1/5\,\mathrm{min}^{-1}$ zu ermöglichen.
Experimentelle Untersuchungen eines Prototypenmodells im Maßstab 1:1 ermöglichten außer-

dem die Dichtigkeit der Kühlmitteldichtungen zu bestimmen und erste qualitative Messungen der transmittierten Wellenfronten durchzuführen.

Abstract

The development of petawatt-class lasers during the last decades has resulted in a reduction of the size and cost of such systems. This development has lead to the adoption of petawatt-class lasers at facilites world-wide for the study of matter in extreme states. The energy density achieved by such systems has lead to their use as direct drivers for particle acceleration, research on inertial confinement fusion and radiation therapy. Further uses for these systems were found in their application as secondary sources for X-rays, ions, electrons, protons and neutrons.

This range of applications has lead to the use of petawatt-class lasers in national as well as university laboratories. The operation as direct and indirect sources requires high repetition rates to ensure the rapid reproducibility of respective results and increased statistics.
While low energy petawatt lasers featuring pulse energies below 100 J are commercially available with repetition rates greater than 1 Hz, the repetition rate of high energy petawatt systems above 100 J pulse energy is limited by the cooling behaviour of their amplifier materials. Most high energy petawatt lasers utilize glass based gain media at apertures above 20 cm in their power amplifier elements. These large apertures are chosen to minimize the occuring intensities in the system and prevent damages to optical elements. However, the low thermal conductivity of glass leads to thermal equilibration times of the gain medium in the range of hours, thus featuring low repetition rates.

The goal of this scientific work is the development of a glass based power amplifier element for high energy petawatt lasers featuring an active cooling scheme to reduce the thermal equilibration time of the gain medium to improve the repetitionrate of the laser. The targeted repetition rates are in the order of $1/5\,\mathrm{min}^{-1}$ for a gain factor of 1.5 with a focus on the high quality and reproducibility of the transmitted wavefront.
To this end, a concept was used that utilizes a laminar coolant flow between two discs of the gain medium to reduce the thermal load on the discs. A set of coolants was investigated to determine their thermal, kinematic, chemical and optical properties to qualify them for use in the prototype. Simulations of the cooling process in the prototype further lead to the discovery of a steady state between the heating and cooling of the gain medium between consecutive pulses. This steady state could be used to enable repeatable wavefront patterns at repetition rates of $1/5\,\mathrm{min}^{-1}$ in the simulations.
Experimental investigations of a full scale prototype model were further used to determine the leak tightness of the coolant seals as well as to conduct the first qualitative measurements of transmitted wavefronts.

Contents

1 Introduction **9**
1.1 Thesis Structure . . . 11

2 Laser Amplification **13**
2.1 Pulse Amplification . . . 13
2.2 Nd:Phosphate Glass . . . 15
2.2.1 Neodymium . . . 16
2.2.2 Host Materials . . . 16
2.3 Optical Pumping . . . 18
2.3.1 Flash Lamps . . . 18
2.3.2 Xenon Lamp Spectrum . . . 19

3 Thermal Effects and Beam Quality **21**
3.1 Heat Sources . . . 21
3.2 Heat Transport . . . 22
3.3 Thermally Induced Optical Response . . . 23
3.3.1 Thermo-Optic Effect . . . 24
3.3.2 Elasto-Optic Effect . . . 24
3.4 Beam Quality . . . 25
3.4.1 Optical Path Distortion . . . 25
3.4.2 Wavefront . . . 26
3.4.3 Aberrations . . . 27

4 Cooled Amplifier Design **31**
4.1 Initial Concept . . . 31
4.2 Coolant Flow . . . 33
4.3 Prototype Design . . . 36
4.3.1 Spacers and Nozzles . . . 37
4.3.2 Amplifier Discs . . . 38
4.3.3 Coolant Sealing . . . 39
4.3.4 Coolant Management . . . 41

5 Coolant **43**
5.1 Thermal and Kinematic Properties . . . 44
5.2 Chemical Compatibility . . . 45
5.3 Optical Properties . . . 46
5.3.1 Absorption Losses . . . 47
5.3.2 Reflection Losses . . . 48
5.3.3 Transmission . . . 52

5.4 Conclusion 55

6 Simulated Prototype Operation 57
6.1 Thermal Distributions 57
6.1.1 Coolant Temperature Profile 57
6.1.2 Simulation of Thermal Distributions 58
6.2 Optical Path and Wavefront 63
6.2.1 Optical Path Distortion 63
6.2.2 Wavefront Analysis 63

7 Prototype Testing 69
7.1 Coolant Seal Tightness 69
7.2 Wavefront Measurements 71
7.3 Simulated Disc Deformation 73

8 Summary and Conclusion 79

9 Future Prospects 81
9.1 Design Improvements 81
9.2 Development of Peripheral Elements 82
9.3 Validation Tests 83

Acknowledgements 85

Bibliography 92

List of Abbreviations 93

List of Figures 97

List of Tables 99

Curriculum Vitae 101

1 Introduction

The research of matter at extreme physical conditions is of vital importance to the understanding of the formation and structure of compact astrophysical objects such as stars, brown dwarfs and planetary interiors [Fortov, 2010] as well as the continued research into nuclear fusion technology [Miller et al., 2004][Cavailler et al., 2004].
The field of *Warm Dense Matter* (WDM) is of special interest to this endeavor, describing pressures between 1 to 100 Mbar at temperatures of 1 to 10 eV corresponding to the interior of giant planetary bodies [Fortov, 2010]. This regime lies at a transition from ordinary condensed matter physics to classical plasma physics where neither of these classical theories are sufficient to describe the experimental results and observations. Therefore, in order to develop the necessary theoretical models for understanding the physical effects in the WDM regime, such as the metallization of hydrogen [Celliers et al., 2018][Knudson et al., 2015] as well as the general interactions of particles at WDM conditions, intensive research is required [Graziani et al., 2014].

To validate different models for this regime, a range of experimental methods have been developed to create WDM conditions in a laboratory. These methods consist of quasi-static procedures, such as the compression of matter by diamond anvil cells [Tateno et al., 2010] which can reach up to 6 Mbar of pressure [Dubrovinsky et al., 2012] as well as transient methods to access even higher pressures of up to 100 Mbar and temperatures of $\approx$1 eV [van Thiel et al., 1966].
These transient methods achieve compression and heating via processes such as explosion compression or high velocity impacts which can be created using light gas guns or ablation driven projectiles.
An additional tool for the transient creation of WDM conditions is the fast process of laser driven shock compression which can be achieved with lasers featuring intensities of 10^{13} W/cm^2. Using laser driven shock compression, the *National Ignition Facility* (NIF) was able to reach pressures exceeding 1 Gbar [Kritcher et al., 2014a].

Further difficulties arise from the need for diagnostic tools with sufficient spatial and temporal resolution to measure the physical conditions of a WDM sample. While surface measurements are accessible by *pyrometric* measurements of the surface radiation and *interferometric* techniques to derive the surface velocity [Celliers et al., 2004], volumetric measurements require the use of penetrating methods. Since WDM is in general optically opaque, high energy radiation is required for probing the depth of the sample. This high energy radiation can be provided in the form of highly energetic particles such as ions, electrons and neutrons [Roth et al., 2013] as well as energetic X-rays.
A common technique for using X-ray probing of WDM in *Inertial Confinement Fusion* (ICF) experiments is X-ray backlighting which enables the assessment of the density and hydrodynamic evolution of the samples [Park et al., 2008]. Modern powerful X-ray backlighter sources are created by using supra-thermal electrons created by the relativistic interaction between a secondary target and a high energy short pulse laser featuring intensities in excess of 10^{17} W/cm^2

[Crane et al., 2010][Blanchot et al., 2013].

The new *Facility for Anti-proton and Ion Research* (FAIR), currently under construction at the *GSI Helmholtzzentrum für Schwerionenforschung GmbH in Darmstadt*, Germany, will have the ability to investigate matter under a variety of extreme conditions by using heavy ion beams from its SIS-100 synchrotron [Spiller et al., 2008]. These heavy ion beams enable the research of quark-gluon plasmas, anti-protons and nuclear synthesis as well as WDM. Using either the HIHEX [Tahir et al., 2019a] or LAPLAS [Tahir et al., 2019b] scheme, the ion beam can be used to create homogenous millimeter-sized samples of WDM in a quasi-steady-state over time periods which are long compared to their thermal equilibration time.
The creation of these WDM samples at FAIR will be conducted at the experimental area of the *Atomic Plasma Physics and Applications* (APPA) collaboration [Neumayer et al., 2014]. This area, called the *APPA cave*, will house the target chamber for the creation of WDM as well as the necessary diagnostic tools.
Due to the use of highly energetic heavy ion beams it is possible to generate large WDM samples at the APPA cave. These sample sizes require a set of highly penetrating diagnostic tools to enable volumetric investigations of the physical states inside the samples. These tools include a proton microscope called *PRIOR* [Varentsov et al., 2016] for proton radiography of the samples as well as a laser driven X-ray backlight source delivering photon energy in excess of 100 keV. The laser for this backlighter source is called the *Helmholtz Beamline* and is required to deliver focused intensities of $>10^{18}\,\mathrm{W/cm^2}$. This system will also be able to serve as a source for secondary protons [Snavely et al., 2000], electrons [Rosmej et al., 2019] and neutrons [Roth et al., 2013] to complement the radiography capabilities.

To develop and test the technology required for the Helmholtz beamline a smaller, lower intensity laser system will be used for early experiments at the APPA cave, called the 100 J *diagnostic laser*. This lower intensity system will deliver frequency doubled pulses of 100 J at 527 nm wavelength with pulse durations between 100 ps and 100 ns to the target. The focused intensities of such a system would be in the range of 10^{12} to $10^{16}\,\mathrm{W/cm^2}$, enabling the generation of 10 keV X-rays for backlighting and scattering experiments.
To provide the necessary resistance to optically induced damages for scaling the 100 J amplifier to the intensities of the Helmholtzbeamline requires the use of large aperture optics.

One critical technology to be developed for the Helmholtz beamline are actively cooled main amplifier modules with the ability to provide homogeneous cooling for the required large apertures. This technology is necessary to enable the laser systems to match the repetition rate of the synchrotron at the APPA cave at one pulse every three to five minutes. Further emphasis of the development is placed on a high quality of the laser focus over consecutive pulses to repeatedly provide high intensities.
These considerations lead to the funding of the development of the actively cooled main amplifier by the *Bundesministerium für Bildung und Forschung* (BMBF) which is the subject of this thesis. Since neither the Helmholtz beamline nor the 100 J laser were projected to be operational before 2024, the ***P**etawatt **H**igh-**E**nergy **L**aser for heavy **I**on e**X**periments* (PHELIX), in operation at GSI since 2008, was chosen to serve as the testbed for the new amplifier design. This laser system features pulse energies of 1 kJ at 10 ns or 120 J at 400 fs [Bagnoud et al., 2010] and would thus be able to operate in the same intensity range as the planned systems, with the

new amplifier modules further serving as potential upgrades to the existing amplifer setup at PHELIX.

1.1 Thesis Structure

To solve the problem of increasing the repetition rate of high energy short pulse lasers by the introduction of actively cooled amplifiers it is first necessary to understand the factors that have limited the repetition rate of such systems to around one pulse every 90 minutes [Bagnoud et al., 2010].
The following chapter thus deals with the amplification of relatively short laser pulses to understand the various processes involved. In section 2.2 the properties of the gain medium proposed for the Helmholtz beamline and the 100 J diagnostic laser as well as the associated host material are discussed. While section 2.3 deals with the properties of the pump sources required for the operation of the gain medium.

Chapter 3 will discuss the sources of heating of the gain medium due to these properties as well as the conduction of heat inside the medium.
With section 3.3 further delving into the thermally induced response of the material and section 3.4 discussing the impact of these thermally induced optical effects on the quality of the beam as well as the quantification of the observable changes.

The design considerations taken to reduce these thermal effects in the gain medium will be discussed in chapter 4. With the included sections discussing the initial considerations on the heating of the gain medium as well as the concept chosen to efficiently reduce its thermal load, followed by the optimization of the coolant flow inside the amplifier and the considerations behind the design of the modular amplifier parts to realize the cooling concept.

The research into the properties and viability of various potential coolants for the amplifier will be discussed in chapter 5. The properties were sectioned off into the classical coolant properties of the thermal and kinematic behaviour of the coolants, their chemical compatibility with the gain medium and their optical properties. With the latter including the experiments conducted to measure the absorption and refraction characteristics of certain coolants to calculate their transmission performance.

Chapters 6 and 7 show the beginning validation of the amplifier design by simulations of the thermally loaded optical design of the amplifier module at the proposed repetition rates as well as preliminary tests and evaluation of the mechanical and optical properties of a full scale prototype module.

2 Laser Amplification

The general process by which monochromatic light can be amplified in an optically active medium has been known since the late 1950s [Schawlow and Townes, 1958] and has been applied since the early 1960s when Maiman developed the first laser [Maiman, 1960]. While early lasers created their beam characteristics and beam power in a single stage, modern high performance lasers separate the pulse generation and amplification. This allows for the creation of a low power seed beam in the oscillator with well defined characteristics such as beam divergence, spectral width and in the case of pulsed applications the pulse shape. The amplifier stage subsequently boosts the energy and power of the beam while retaining the beam characteristics set in the oscillator [Koechner, 1999]. This development in conjunction with the development of the *chirped pulse amplification* process [Strickland and Mourou, 1985] opened the door for high peak power lasers which offer various applications in the field of plasma physics and beyond. In the 1970s, development began on such systems to drive inertial confinement fusion experiments [Brown, 1981], since then their fields of application have been expanded to include the use in X-ray laser sources, studies of plasma physics and equation of state, material studies and laser-driven ion beams as well as recent developments in laser driven neutron sources [Roth et al., 2013]. While these modern systems benefit from roughly half a century of development the basic principles discovered by Scharlow and Townes have stayed the same. The following chapter will discuss the amplification of short laser pulses inside a solid amplifier medium as presented in [Koechner, 1999], the characteristics of the amplifier medium and pump source used in this project as well as their impact on the repetition rate of such a system.

2.1 Pulse Amplification

Laser is an acronym for **L**ight **A**mplification by **S**timulated **E**mission of **R**adiation. The *stimulated emission* is the core process of the amplification inside a laser. In this process, an incoming photon can cause an excited electron in the *gain medium*, with a stored energy close to the photons frequency, to release its energy and create a second photon with the exact same characteristics as the incoming photon.
To operate a medium as a coherent light amplifier it is necessary to disturb its electron distribution from the thermal equilibrium. In the thermal equilibrium, the electron population is concentrated in the ground state and the medium will act as an attenuator by absorbing incoming light. In a configuration, where the majority of the electrons is located in an energy level above the ground state the medium can create more stimulated photons than are being absorbed. This configuration is called an inverted electron population. Two archetypes of energy level structures in materials exist that enable the generation of an inverted electron population. The three-level system, shown in figure 2.1a, can be used to achieve the inverted electron population between the ground state and the upper laser level ② by exciting electrons from the

ground state into the pump band ③. In the three-level system electrons in the pump band feature a far shorter spontaneous emission life time than in the upper laser level thus increasing the electron population in ② compared to the ground state, creating the population inversion. The four-level system, shown in figure 2.1b, operates similarly to the three-level system but features a second laser level called the lower laser level ① which is seperate from the ground state compared to the three-level system where ground state and lower laser level are identical. Electrons in the lower laser level feature a lower life time compared to electrons in the upper laser level thus enabling the creation of a population inversion by pumping. The separation of the lower laser level and the ground state leads to a disconnect of the laser operation from the electron population in the ground state. This leads to the four-level system being capable to operate at lower pump rates as the population inversion only has to be a relative inversion between the upper and lower laser levels [Koechner, 1999].

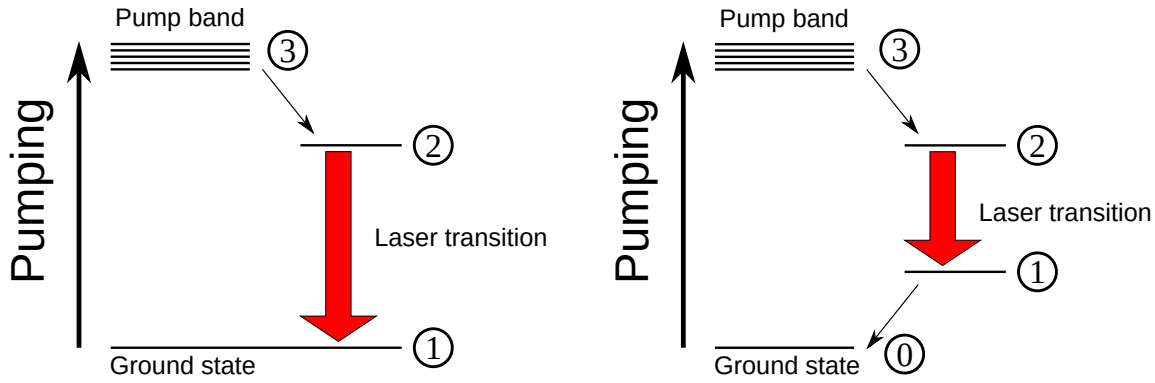

(a) Energy level structure of a three-level system.

(b) Energy level structure of a three-level system.

Figure 2.1: Energy level structure of the two archetypes of electron configurations for gain media.

The dynamic behaviour of electron populations in a gain medium can be described using a set of coupled rate equations representing the various energy levels. By focusing on the amplification process of pulsed input signals with pulse lengths far shorter than the pumping rate W_p and the spontaneous emission time τ_f the system can be viewed as quasi-stable. In this state, it is assumed that the amplification is dominated by the energy stored in the upper laser level prior to the arrival of the input pulse. Thus, the rate equation describing the evolution of the electron population in the upper laser level can be simplified to

$$\frac{\partial n}{\partial t} = -\gamma n c \sigma \phi, \tag{2.1}$$

as the effects of fluorescence and pumping can be neglected [Koechner, 1999]. Here n describes the inverted population density, c the speed of light in the active medium, σ the stimulated emission cross-section, ϕ the photon density and γ is used to differentiate between three and four-level systems, with $\gamma = 2$ for a three level-system and $\gamma = 1$ for a four-level system. The evolution of the photon density can be described by a second differential equation, the photon-transport equation:

$$\frac{\partial \phi}{\partial t} = cn\sigma\phi - \frac{\partial \phi}{\partial x}c. \tag{2.2}$$

Solving equations (2.1) and (2.2) for n and ϕ, *Frantz* and *Nodvik* [Frantz and Nodvik, 1963] found a solution for a square pulse of duration t_p and an initial photon density of ϕ_0 resulting in the amplified photon density $\phi(x,t)$. By time integrating this photon density in an amplifier of length l the gain G of the amplifier can be derived as

$$G = \frac{1}{\phi_0 t_p} \int_{-\infty}^{\infty} \phi(l,t)dt = \frac{E_{sat}}{E_{in}} \ln\left(1 + \left[\exp\left(\frac{E_{in}}{E_{sat}}\right) - 1\right] G_0\right) \tag{2.3}$$

with

$$E_{in} = c\phi_0 t_p h\nu \tag{2.4}$$

$$E_{sat} = \frac{h\nu n}{\gamma\sigma n} = \frac{J_{st}}{\gamma g_0} \tag{2.5}$$

$$J_{st} = g_0 E_{sat}. \tag{2.6}$$

Here equation (2.3) describes the gain of an amplifier over the entire range of possible input signals, from very small signals up to saturation. (2.4) represents the fluence of the incoming signal with (2.5) describing the saturation fluence and (2.6) the stored energy per unit volume, while $g_0 = n\sigma$ is the small-signal gain coefficient [Koechner, 1999].
In the case of a very small input signal ($E_{in} \ll E_{sat}$, $G_0 E_{in}/E_{sat} \ll 1$), (2.3) can be simplified to

$$G \approx G_0 = \exp(g_0 l) = \exp(n\sigma l) \tag{2.7}$$

which is called the small signal gain and only depends on the inverted population density, the stimulated emission cross-section and the length of the amplifying medium l. In this case, saturation effects can be ignored but if the amplification raises the output signal to a level where $G_0 E_{in} \ll E_{sat}$ no longer holds true, (2.7) no longer applies.
In the case of very high input fluences ($E_{in} \gg E_{sat}$), (2.3) can be approximated by

$$G \approx 1 + \left(\frac{E_{sat}}{E_{in}}\right) g_0 l \tag{2.8}$$

Thus, showing an exponential growth of the gain factor in the small-signal regime with respect to the length of the gain medium, with the amplification evolving into a linear growth once saturation effects can no longer be ignored at higher input fluences.

2.2 Nd:Phosphate Glass

With the gain factor of a laser amplifier depending on the ability of the gain medium to store optical energy in its electronic structure, an investigation into one of the most common amplifier materials for high energy solid state lasers is needed. Since the early days of solid-state laser development, trivalent neodymium (Nd^{3+}) has been been known to exhibit a very favourable combination of features for optical amplification. It offers a satisfactorily long fluorescence lifetime with narrow emission lines and its laser transitions are separated far enough from the ground state to operate the laser at varying temperatures with little impact on the amplification.

Over the years, a variety of host materials have been tested but only yttrium aluminium garnet (YAG) and a select number of glass materials have shown the necessary properties to host trivalent neodymium without negative impact on its line structure or disadvantageous physical properties [Koechner, 1999]. To understand the features of Nd-doped glass it is necessary to understand the spectral charactersitics of trivalent neodymium as well as the advantages and disadvantages provided by different host materials.

2.2.1 Neodymium

Neodymium is a rare-earth element, as such it features sharp flourescent transitions in the near infra-red range [Koechner, 1999]. These sharp transitions are a result of its favourable electron configuration. In its ground state the electron configuration consists of a core which is identical to the xenon configuration with all three inner shells completely filled as well as some additional electrons in higher shells. As a dopant neodymium is available in its Nd^{3+} state in which there are only three electrons left in the fourth shell of the atom which are used for the laser transitions. However, additional electrons remain in the higher fifth shell and provide shielding for the transition electrons which causes the sharp line features of neodymium [Koechner, 1999].
Despite the variety of transitions in Nd^{3+} depicted in figure 2.2, only the ${}^4F_{3/2} \rightarrow {}^4I_{11/2}$ transition at 1064 nm is of practical use. This is due to the ${}^4F_{3/2} \rightarrow {}^4I_{9/2}$ transition beeing resonant and thus being absorbed as well as it is emitted, while ${}^4F_{3/2} \rightarrow {}^4I_{15/2}$ and ${}^4F_{3/2} \rightarrow {}^4I_{13/2}$ are absorbed in most of the common host materials [Brown, 1981].
Figure 2.2 shows that Nd^{3+} forms a four-level system with ${}^4F_{3/2}$ and ${}^4I_{11/2}$ as the respective laser levels and ${}^4I_{9/2}$ as the ground state. Pumping is usually broad band and excites many of the higher levels of which most decay into the ${}^4F_{3/2}$ state. The life time of the ground state transition ${}^4I_{11/2} \rightarrow {}^4I_{9/2}$ depends on the host material, doping concentration and temperature but is usually in the range of several tens of nanoseconds [Brown, 1981].
The large energy gap between the lower laser level and the ground state offers the advantage of operating neodymium based gain media over a wide temperature range as thermal excitations from the ground state will not contribute significantly to the population in the lower laser level [Koechner, 1999].

2.2.2 Host Materials

Rare earth gain materials like neodymium are usually doped into secondary materials to enable the practical use of the gain medium in an optical amplifier. The secondary materials are called host materials and their interaction with the dopant can change the gain behaviour of the compound. A common choice of host materials for rare earth dopants are crystalline and glass hosts, which offer distinct properties determining their respective field of use.
Crystals offer far better thermal conductivity and lower laser thresholds while glass has wider emission lines and can be doped to much higher concentrations. This leads to the use of neodymium doped crystals in very high repetition rate amplifiers which benefit greatly from the high thermal conductivity. Neodymium doped glass is usually used in short pulse high power systems where the spectral width of the emission lines is necessary to achieve very short

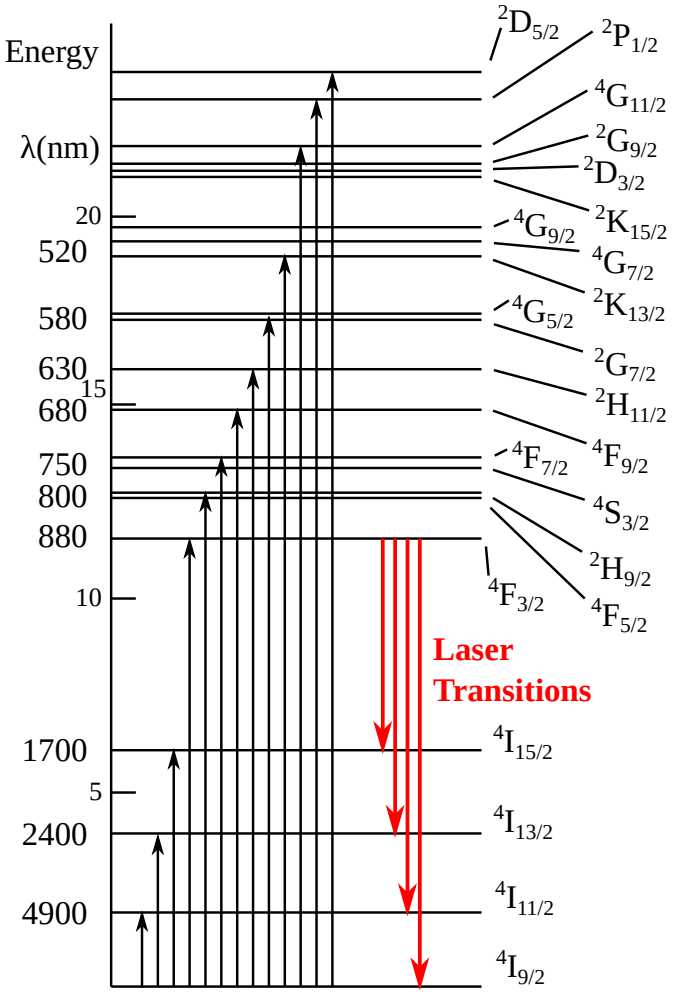

Figure 2.2: Energy levels and transitions in Nd^{3+} [Brown, 1981].

laser pulses.
Glass also features a much more isotropic distribution of the dopant compared to crystals. These anisotropic dopant distributions in a crystal are caused by its growth process in which the different sizes of dopant and regular lattice ions leads to a discrimination during the lattice formation. In the case of Nd:YAG the Nd^{3+} is larger than the Y^{3+} and thus the neodymium is preferentially retained in the melt. Since crystals are usually grown from a single melt this leads to an increase in neodymium concentration in the outer layers of the crystal [Koechner, 1999].
This also makes large crystals increasingly brittle and complicates the growth of crystals larger than 10-15 cm in diameter while glass disks have been manufactured in sizes of up to 90 cm in diameter and several centimeters in thickness due to their amorphous nature.
Of the glass hosts for neodymium usually only silicate (SiO_2) and phosphate (P_2O_5) glass are commercially available. While neodymium doped silicate glass offers a slightly wider spectral width of the emission lines compared to neodymium doped phosphate glass, the emission cross-section of phosphate glass is typically 50% higher ($\sigma = 3.7–4.5 \times 10^{-20}$ cm^2) [Koechner, 1999]. This has lead to the adoption of Nd:phosphate glass in many large laser systems for fusion research [Stokowski et al., 1981] as large diameter disks are necessary to keep the fluence below the damage threshold while increasing the energy.

2.3 Optical Pumping

Chapter 2.1 has shown the dependence of laser amplification process on the inverted electron population compared to the thermal equilibrium. This population inversion can be created by the pumping process which deposits energy in the gain medium at the appropriate transition energies.
A variety of pump sources exists, which can be used to excite different types of gain media. While gaseous media such as CO_2 and Helium-Neon mixtures can be excited using collision excitation induced by electrical fields and diode lasers use direct electrical excitation from applied currents, dye and solid-state lasers, such as neodymium doped glass, are pumped using light from optical pump sources.
These optical pumps can be differentiated in line emitting sources, black body sources and mixed sources. Line sources feature monochromatic spectra and have to be tailored specifically for the gain medium. This category includes light emitting diodes (LED) and pump lasers. The advantage of these pump sources is their high efficiency, since the energy used to operate these sources is converted much more efficiently into light of wavelengths which can be absorbed by the gain medium. However, their price and complexity over the other sources has hindered their wide spread adoption.
Blackbody sources such as filament lamps emit light in a broad spectrum depending on the temperature of the emitting surface. Due to their broad-band emission only a small fraction of the emitted light is of wavelengths which can be used in the gain medium to achieve the population inversion, while the remaining optical energy is mostly converted into thermal energy, resulting in heating of the gain medium.
Mixed sources such as flash lamps emit a blackbody spectrum with additional line features. They offer a compromise between the efficient coupling of their optical energy into the gain medium by line emitters and the low cost and simplicity offered by blackbody sources [Koechner, 1999]. These features lead to the decision to use flash lamps as the pump source for this project.

2.3.1 Flash Lamps

As flash lamps offer a high optical radiation output at a comparetively low price per unit, this makes them ideal for the use in large scale solid-state laser amplifiers like those used in facilities like the *National Ignition Facility* (NIF) in the United States of America [Miller et al., 2004] or the *Laser Mégajoule* (LMJ) in France [Cavailler et al., 2004] which utilize large arrays of flash lamps.
Flash lamps are usually constructed as a linear or helical quartz tube, depending on the design of the amplifier, filled with a nobel gas which can be ionized by electrodes at either end of the tube. An array of capacitors is used to create a pulse of electric energy which is discharged between the electrodes of the lamp, exciting the noble gas into the plasma state. The radiation from the plasma is used to pump the laser medium but is also partially absorbed by the quarz tube of the lamp resulting in the heating of the tube. Further heat loading of the flash lamps is incurred by the electric losses at the electrodes and contact with the plasma. This heat loading reduces the lamps life time and excessive heat can lead to immediate damages. Different cooling schemes are possible to mitigate the problem depending on the systems requirements.

Free-air convection cooling can dissipate about $5\,W/cm^2$ while forced-air cooling achieves up to $40\,W/cm^2$. Liquid cooling and a water jacket around the flashtube offer dissipation rates of $300\,W/cm^2$ [Koechner, 1999] which become necessary at higher repetition rates.
Despite the heat losses the overall efficiency is rather high for flash lamps, with measurements finding that 65 to 80% of the applied electrical energy are converted into radiation in the spectral region of 0.35-1.1 m, depending on the gas filling, applied current and pressure. [Brown, 1981].
A common gas filling of the flash lamps in facilities such as NIF and LMJ is xenon, which is chosen due to its higher radiation output for a given input energy compared to other gas fillings and the overlap between its emission spectrum with the absorption spectra of neodymium based gain media [Brown, 1981].

2.3.2 Xenon Lamp Spectrum

The spectrum emitted by a xenon filled flash lamp is highly dependent on the power density inside the plasma. This leads to the spectrum shown in figure 2.3 to be dominated by line features for power densities as low as $1\,kA/cm^2$, which is caused by transitions between bound energy states of the ions in the plasma. While the spectrum becomes increasingly dominated by the continuum radiation of a black body for higher power densities, resulting from the recombination radiation of free electrons to the ions and bremsstrahlung from free electron collisions with ions.

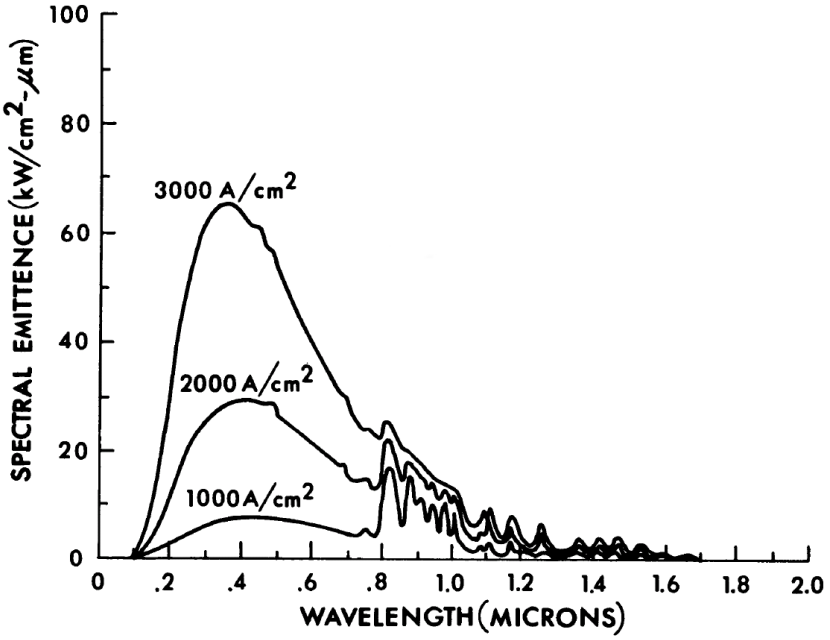

Figure 2.3: Example of an emitted spectrum for a xenon flash lamp at current densities of 1, 2 and $3\,kA/cm^2$ [Brown, 1981], showing the transition from a line dominated spectrum to a black body dominated spectrum with increasing current densities.

Further influences on the spectrum are the pressure of the gas filling and the geometry of the flash lamp. The tubing material of the flash lamp also plays a crucial role in its performance. The material determines how much of the radiation emitted from the plasma is absorbed in

the glass and how much is reflected back into the plasma to be absorbed and reemitted. Since flash lamps emit radiation in all directions they are usually mounted inside an elaborate reflector geometry to guide the emitted radiation into the laser material as efficiently as possible [Brown, 1981].

3 Thermal Effects and Beam Quality

In pulsed laser systems the repetition rate is often limited by their ability to reproduce certain beam characteristics (i.e. focus size, pointing, etc.) over consecutive pulses due to the presence of temperature gradients inside their optical components. In an optical amplifier, these gradients are caused by inhomogenous heating of the optical material due to anisotropic absorption of pumplight in the medium either for geometric reasons or anisotropic distributions of absorption centers. Further gradients are introduced by the limitations of applied cooling schemes to extract the heat isotropically from the medium. This chapter will explore the mechanisms by which heat is introduced and distributed inside the gain medium and the potential coolant, the thermally induced changes to the optical properties of the gain medium and the resulting impact on the beam quality.

3.1 Heat Sources

While the energy responsible for the heating of the gain medium is provided by the pumplight (chp. 2.3), there are four major mechanisms by which optical energy is converted into heat inside the gain medium which will be discussed below.
A large contribution to the thermal excitation of the gain medium is the absorption of pumplight in the host material. In glass, this absorption occurs mainly in the IR and UV range [Koechner, 1999] and is especially important when using pumplight from blackbody or mixed sources due to their wide spectral range (see chp. 2.3). Pump sources which are tailored to the absorption band of the gain medium, such as pump diodes or secondary lasers, can be used to mitigate this heating mechanism.
Another source of heating is the *quantum defect* heating which occurs due to the energy difference between the absorption band of the active ions and the upper laser level (i.e. fig.2.2). These transitions can decay via multi-phonon decay and thus lose their energy as heat to the hosts lattice structure instead of photon radiation [Koechner, 1999].
The same effect occurs at the energy gap between the lower laser level and the ground state of the active ions in a four-level laser. This relaxation to the ground state is also a non-radiative transition and thus contributes to the heating of the host material [Koechner, 1999].
Excited active ions can also transfer energy to ions in their vicinity. If the receiving ion is another active ion, the process is called *diffusion* and the energy is lost via stimulated emission or fluorescence. If the receiving ion is a lattice ion, this effect is called *quenching* and the lattice ion will lose its energy via thermal processes, thus contribution to the heating of the gain medium. The effect of quenching is strongly dependent on the concentration of active ions in the host material and also reduces the fluorescence life time of the laser transition [Brown, 1981]. Doping concentration therefore has to be a compromise between energy storage capability, fluorescence life time and heat generation.
Further heating of the gain medium occurs due to uncooled flash lamps as thermal radiation and

convection from the lamps also imparts heat on the medium. In water-cooled flash lamps this effect is suppressed by the absorption of thermal radiation in the water [Koechner, 1999].

3.2 Heat Transport

In an amplifier, the effects discussed in chapter 3.1 are not applied isotropically to the medium. The reasons for anisotropic heating are manyfold but are usually caused by anisotropic irradiation of the gain medium by the pumplight as well as uneven doping concentrations which impact the absorption. This leads to thermal gradients inside the gain medium which can be equilibrated via the mechanisms of thermal conduction, thermal radiation and convection in fluids [Meschede et al., 2015].

Thermal conduction is a process by which thermal energy is transported through a material without macroscopic movement of the material. It is caused by molecular collisions due to thermal motion and always occurs along thermal gradients. On a macroscopic level, the heat transport can be described by the *thermal conduction equation*

$$\vec{j} = -\lambda \cdot \nabla T \tag{3.1}$$

where $\vec{j}$ is the thermal flux density, λ is the thermal conductivity of the material and ∇T is the thermal gradient. The resulting thermal flux $\dot{Q}$ can be calculated by integrating over the cross section $\vec{A}$ through which the thermal energy is transported:

$$\dot{Q} = \int \vec{j} \cdot d\vec{A} \tag{3.2}$$

In the case of a linear one-dimensional thermal gradient (fig. 3.1), equation (3.2) can be expressed as

$$\dot{Q} = A \cdot \lambda \cdot \frac{\Delta T}{l} \tag{3.3}$$

where $\Delta T = T_{\text{hot}} - T_{\text{cold}}$ is the temperature difference between the hot and cold material and l is the thickness of the material [Meschede et al., 2015].

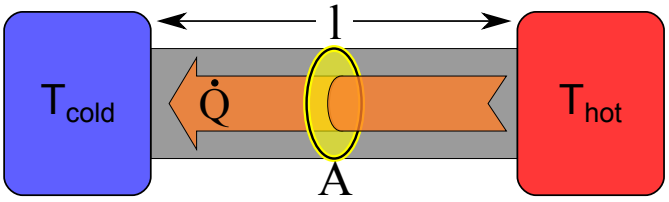

Figure 3.1: Conduction of thermal energy from a hot to a cold area of equal size.

Thermal conduction is highly dependent on the mean free path of phonons in the material and thus varies widely for different materials with diamonds featuring thermal conductivities of $\approx 180\,\mathrm{Wm^{-1}K^{-1}}$ [Slack, 1964] while phosphate glass usually reaches $\approx 0.56\,\mathrm{Wm^{-1}K^{-1}}$ [Hu et al., 2014].

The time it takes for a material to return to its thermal equilibrium is called the *thermal relaxation time*. This relaxation time for thermal conduction can be calculated by

$$\tau = \frac{d^2 \varrho c_p}{\lambda} \tag{3.4}$$

which depends on the spatial dimension of the thermal gradient d, the density of the material ϱ, the specific heat capacity of the material c_p and the thermal conductivity λ. With ϱ, c_p and λ further depending on the temperature [Meschede et al., 2015].

The transmission of heat from one medium to another can be described in terms of the emitted and aborbed thermal radiation at the boundary surface between the two media. Using the *Stefan-Boltzmann law* it is possible to define the thermal flux caused by radiation as

$$\dot{Q} = \dot{Q}_{\text{amb}} - \dot{Q}_{\text{surf}} = \sigma A \left(T_{\text{amb}}^4 - T_{\text{surf}}^4 \right) \tag{3.5}$$

where σ is the *Stefan-Boltzmann constant* and T_{amb} and T_{surf} are the temperatures of the ambient material and the hot surface respectively.
For large differences between T_{amb} and T_{surf} the thermal flux can be written as

$$\dot{Q} \approx 4\, \sigma\, T_{\text{surf}}^3 A\, \left(T_{\text{amb}} - T_{\text{surf}} \right). \tag{3.6}$$

This gives us *Newton's cooling law* with $4\sigma T^3 \approx 6$ W m^{-2} K^{-1} at room temperature for a black body [Meschede et al., 2015].

In fluids, heat can also be transported via a process called *convection*. Convection relies on the macroscopic motion of volumina of different temperature to transport heat. It can be separated into *natural convection* which is caused by density changes in the fluid due to heating and *forced convection* which is a process where the motion of the fluid is externally driven. Convection is usually considered to provide a much higher thermal flux at moderate temperatures compared to thermal conduction or radiation [Meschede et al., 2015]. However, the movement patterns of these fluid volumina are very complex and 3-dimensional thermal transport in fluids is usually calculated using computer algorythms.

3.3 Thermally Induced Optical Response

In high repetition laser systems, it might be necessary to launch pulses faster than the thermal relaxation time of the gain medium. This will lead to the presence of residual thermal gradients in the medium during the pulse. The optical response of the medium to these thermal gradients leads to changes of the optical properties of the medium. The changes to the refractive can be described via a direct dependence of the refractive index on the temperature of the medium in the *thermo-optic effect* and an indirect dependence in the refractive index changes caused by thermally induced stresses described in the *elasto-optic effect*.

3.3.1 Thermo-Optic Effect

Studies on the thermo-optic behaviour of semiconductors and insulators, such as glass, have shown that the thermally induced refractive index changes observed in these materials can be traced to electronic and lattice effects [Lines, 1993]. The cause is an increase in temperature broadening the Fermi-distribution leading to increases of the resonance frequency of optical phonons in the lattice, thus increasing the likelyhood of band-band transitions. These effects lead to higher absorption and subsequently increase the refractive index of the material [Fieberg, 2014].
To quantitively describe the thermo-optic effect over a wide range of temperatures, the refractive index can be calculated using the *Sellmeier* representation:

$$n^2 - 1 = \frac{E_d E_0}{E_0^2 - \omega^2} - \frac{E_1^2}{\omega^2} \tag{3.7}$$

in which ω is the photon energy and E_d, E_1 and E_0 are the Sellmeier energies depending on the structure and temperature of the material [Lines, 1993]. However, for small temperature variations it is possible to describe the thermally induced changes to the refractive index via the linear thermo-optic coefficient dn/dT and the temperature difference ΔT:

$$\Delta n = \frac{dn}{dT} \cdot \Delta T \tag{3.8}$$

3.3.2 Elasto-Optic Effect

Temperature gradients also cause mechanical stress in a material due to uneven thermal expansion. These stresses also influence the refractive index in a process called the *elasto-optic effect*. This effect is highly directional as uneven distributions of stress cause different changes to the refractive index depending on the stress vectors. To represent this mathematically, the refractive index can be expressed by the linear optical indicatrix. The indicatrix is generally an ellipsoid which can change its shape, size and orientation due to stress and strain [Koechner, 1999]. These changes to the indicatrix can be expressed by the coefficients

$$\Delta B_{ij} = P_{ijkl}\varepsilon_{kl} \qquad (i,j,k,l = 1,2,3) \tag{3.9}$$

which can be derived from the fourth-rank elasto-optic tensor P_{ijkl} and the second-rank strain tensor ε_{kl}. Under the assumption of a circular beam geometry and stresses in radial and tangential directions, it is advantageous to express the elasto-optic changes to the refractive index n_0 in cylindrical coordinates [Nye, 1957].

$$\Delta n_r = \frac{1}{2} n_0^3 \Delta B_r \tag{3.10}$$

$$\Delta n_\phi = \frac{1}{2} n_0^3 \Delta B_\phi \tag{3.11}$$

resulting in expressions for the radial n_r and tangential n_ϕ components of the refractive index change, which can be expressed as as superposition of both components

$$\Delta n_s = \Delta n_r + \Delta n_\phi. \tag{3.12}$$

These directional components of the refractive index can lead to stress induced *birefringence* in otherwise isotropic media [Lines, 1993].

3.4 Beam Quality

The performance of high intensity laser systems depends strongly on their ability to focus the laser beam which can be impacted by the presence of thermal gradients in the optical medium and the resulting refractive index variations caused by the *thermo-optic* and *elasto-optic* effects. The limits of focusability in an optical system are determined by the diffraction limits of the optics, the geometry of the optics and the complex wavefunction of the beam itself. Thus, the ideal beam is commonly referred to as the *diffraction-limited* beam, which therefore defines the maximum beam quality in terms of focusing capability [Wyant and Creath, 1992]. Deviations of the spatial phase of a real beam from the ideal beam are called *aberrations*, they can be caused by faulty optics, misalignment of optical components, environmental factors and thermal effects [Ohland, 2018]. This section will discuss the optical path distortions as a result of the *thermo-optic* and *elasto-optic* effects, the *wavefront* as a property of the beam and how various aberrations impact its shape and peak intensity in the far field.

3.4.1 Optical Path Distortion

The thermo-optic and thermally induced elasto-optic effects have shown how thermal gradients impact the refractive index of materials. These changes to the refractive index influence the *optical path* of a beam which describes the distance for which a beam of light propagating in a vacuum would take the same amount of time as a beam propagating in a medium. The optical path L_{opt} can be calculated as a product of the physical distance l a beam has to propagate through a medium and the refractive index n of said medium,

$$L_{\text{opt}} = l \cdot n. \tag{3.13}$$

Since the refractive index as well as the length of a specimen depend on the temperature of the material, thermal gradients in the medium can lead to optical path differences between various partial beams of a spatially extended beam.
The dependence of the physical length of a sample on its temperature distribution at the position of a partial beam can be described by the linear thermal expansion [Koechner, 1999]:

$$l(\vec{r}) = \alpha_0 l_0 [T(\vec{r}) - T_0] \tag{3.14}$$

with the linear thermal expansion coefficient α_0, the base length of the expanding specimen l_0 and the temperatures at the position of the partial beam $T(\vec{r})$ and the beam center T_0.
Combining the thermal expansion (3.14), the thermo-optic effect (3.8) and the elasto-optic effect (3.12) a description of the optical path can be found for each partial beam in a thermally loaded medium [Lines, 1993]:

$$\begin{aligned} L_{\text{opt}}(\vec{r}) = &\int_0^d \frac{dn}{dT}(T(\vec{r},z) - T_0) \cdot [1 + \varepsilon_z(\vec{r},z)]dz \\ &+ \int_0^d \Delta n_s(\vec{r},z) \cdot [1 + \varepsilon_z(\vec{r},z)]dz \\ &+ \int_0^d [n_0 - 1] \cdot \varepsilon_z(\vec{r},z)dz - z_0(\vec{r}) \end{aligned} \tag{3.15}$$

where the first term contains the optical path modified by the thermo-optic effect, the second term the modifications due to the elasto-optic effect and the third term accounts for deformations of the optical material.

3.4.2 Wavefront

Describing a beam of light as a bundle of rays has been useful for describing the effect of thermal effects on the optical path of each partial beam. However, the behaviour of light in the focal plane of an optic is generally not accurately described by the purely geometric behaviour of rays. Instead wave optics has to be used to describe effects like diffraction which are dominant in this region.
The key to this representation is the *Helmholtz wave equation*

$$(\nabla^2 + \mu\epsilon\omega^2)\vec{E} = 0 \tag{3.16}$$

$$(\nabla^2 + \mu\epsilon\omega^2)\vec{B} = 0 \tag{3.17}$$

which describes the behaviour of electro-magnetic waves and can be derived from the *Maxwell equations* [Jackson and Witte, 2006]. Due to the connection between the electric and the magnetic field of the wave, it is sufficient to describe the electro-magnetic wave by either one of the two fields. Since the amplitude of the electric field can be measured in the form of the intensity ($|E|^2$) it is common to choose the electric field representation of the wave. Depending on the geometry of the system, several solutions of the wave equation exist, such as the *plane wave* or the *gaussian beam*. The following pragraph will focus on the solution of a mono-chromatic top-hat beam at a circular aperture, since it features the closest semblance to our application:

$$E(r,\rho,t) = E_0(r,\rho)e^{i\left(-\omega t+\phi\frac{r}{\rho}\right)} \tag{3.18}$$

with the amplitude of the electric field

$$E_0(r,\rho) = \begin{cases} E_0 & \text{for } r \leq R \\ 0 & \text{for } r > R \end{cases}, \tag{3.19}$$

the spatial phase $\phi(r,\rho)$ and the radius of the aperture R [Born et al., 1999].
The behaviour of a general monochromatic wave can usually be described in two regimes, the *near field* directly in front of diffracting or refracting elements, where small angle and *Fresnel approximations* are valid [Born et al., 1999], and the *far field* at large distances behind the optics which is also referred to as *Fraunhofer diffraction*. The propagation of a wave from its near-field to the far field can be modeled as a *Fourier transformation* over the complex electric field. The field consists of the real amplitude of the electric field and a complex phase denoting the oscillation state of the field (see (3.18)). Points of the three-dimensional electric field at the same oscillation state can be grouped into a surface which is called the *wavefront*. This method loses the information about the absolute value of the phase, however, since the observable in most experiments is the intensity ($|E|^2$), any complex factors such as the phase factor $e^{i\phi}$, do not impact the observable. Since the absolute value of the phase can not be observed, descriptions of the near field usually use the wavefront for its intuitive representation (fig. 3.2).

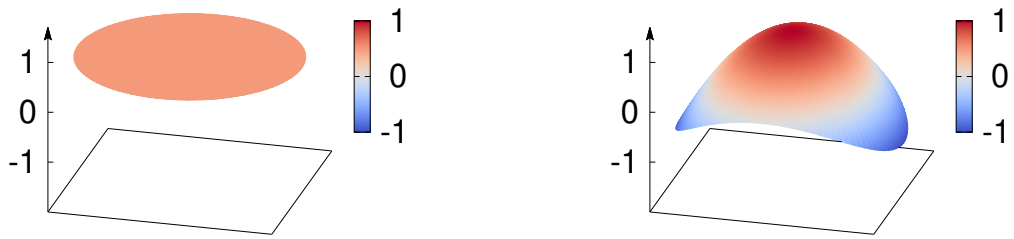

(a) A plane wavefront, which is usually considered ideal for laser applications

(b) Wavefront with arbitrary aberration features

Figure 3.2: Examples of two wavefronts with various wavefront features.

3.4.3 Aberrations

Most laser applications seek to maximize the intensity in the focus of the beam. This can be achieved by using a beam profile approximating a plane wavefront (fig. 3.2a), such as a top-hat profile, which can be focused to the highest intensity possible compared to other wavefront profiles [Born et al., 1999]. In laser optics, the plane wave is therefore considered the ideal case when evaluating the quality of the beam.
In an amplifier, this ideal case is rarely achieved as the optical path of the beam is locally modified by thermal effects (see chp. 3.3). The resulting local phase shifts can be calculated using

$$\Delta\phi(x,y) = \frac{2\pi}{\lambda} \cdot \Delta L_{\text{opt}}(x,y) \tag{3.20}$$

with the laser wavelength λ and the shift in the optical path ΔL_{opt} [Lines, 1993]. These local shifts lead to deformations of the wavefront which diminish the quality of the beam and are called *aberrations*.
By expanding the wavefront in a power series in polar coordinates it is possible to assign each of the resulting terms to a type of aberration [Wyant and Creath, 1992]:

$$\Phi(r,\theta) = A_1 r\cos(\alpha_1+\theta) + A_2 r^2 + A_3 r^2\cos^2(\alpha_3+\theta) + A_4 r^3\cos(\alpha_4+\theta) + A_5 r^4 \ldots \tag{3.21}$$

where A_{1-5} are the wavefront aberration coefficients, $\alpha_{1,3,4}$ are the orientations of the angular dependent aberration components, r is the radial and θ the angular coordinate of the beam. The five aberrations which can be identified in (3.21) are called *Seidel aberrations*, their distinct profiles have been compiled in figure 3.3.

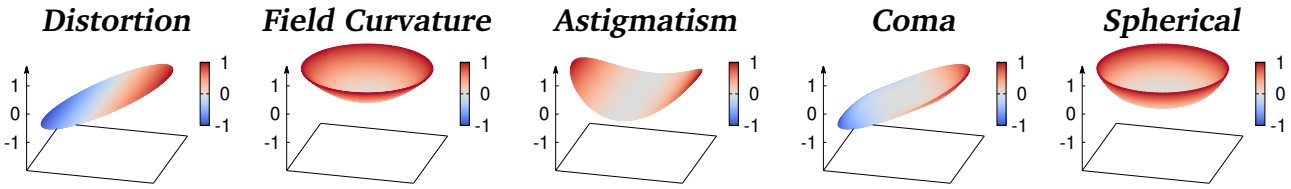

Figure 3.3: Seidel aberrations of the wavefront with their associated functional terms and wavefront profiles.

However, using the Seidel aberrations for analyzing the wavefront can be problematic, as *distortion* and *field curvature* only lead to a spatial shift of the intensity profile, while *astigmatism*, *coma* and the *spherical* aberration cause more complex deformations. These complex deformations lead to intensity profiles where the location of maximum intensity is shifted out of the focal plane. To avoid the problem of shifting foci it is possible to choose a different mathematical representation. By expanding the wavefront in an orthogonal base on the unit circle it is possible to find a set of polynomials whose wavefront representations resemble the observable Seidel aberrations but without changes to the focus position.
One set of polynomials that fulfills these criteria are the *Zernike polynomials* which are useful for describing the wavefront of circular beams due to their rotational symmetry [Wyant and Creath, 1992]. In polar coordinates Zernike polynomials can be written as a product of a radial term $R_n^m(\rho)$ and a periodic angular term $G_m(\theta)$:

$$Z_n^m(\rho,\theta) = R_n^m(\rho)G_m(\theta) \tag{3.22}$$

with the radial coordinate ρ and the angular coordinate θ. The indices m and n are integers representing the angular and radial degree of the polynomial respectively. They follow the condition $m = n-2k$ where k is a non-negative integer and $n \geq |m|$. In [von Zernike, 1934] the angular term is defined as

$$G_m(\theta) = \begin{cases} m \geq 0; & \cos(m\theta) \\ m < 0; & \sin(m\theta) \end{cases} \tag{3.23}$$

while the definition of the radial term under the normalization $R_n^m(1) = 1$ is

$$R_n^m(\rho) = \sum_{k=0}^{\frac{n-|m|}{2}} (-1)^k \binom{n-k}{k} \binom{n-2k}{\frac{n-|m|}{2}-k} \rho^{n-2k} \quad . \tag{3.24}$$

For easier handling of the polynomials, for example in software, they can be indexed using an indexing scheme proposed by [Noll, 1976] which is defined by

$$\begin{aligned} j_u < j_v \quad &\forall \quad n_u < n_v, \\ j_u < j_v \quad &\forall \quad |m_u| < |m_v| \wedge n_u = n_v, \\ j &= \begin{cases} m > 0; & \text{even} \\ m < 0; & \text{odd} \end{cases} \quad . \end{aligned}$$

By comparing the Zernike aberrations (fig. 3.4) to the Seidel aberrations (fig. 3.3) it is apparent that the goal of recreating the observable wavefront distortion of the Seidel aberrations can be achieved by the use of Zernike polynomials [Wyant and Creath, 1992].

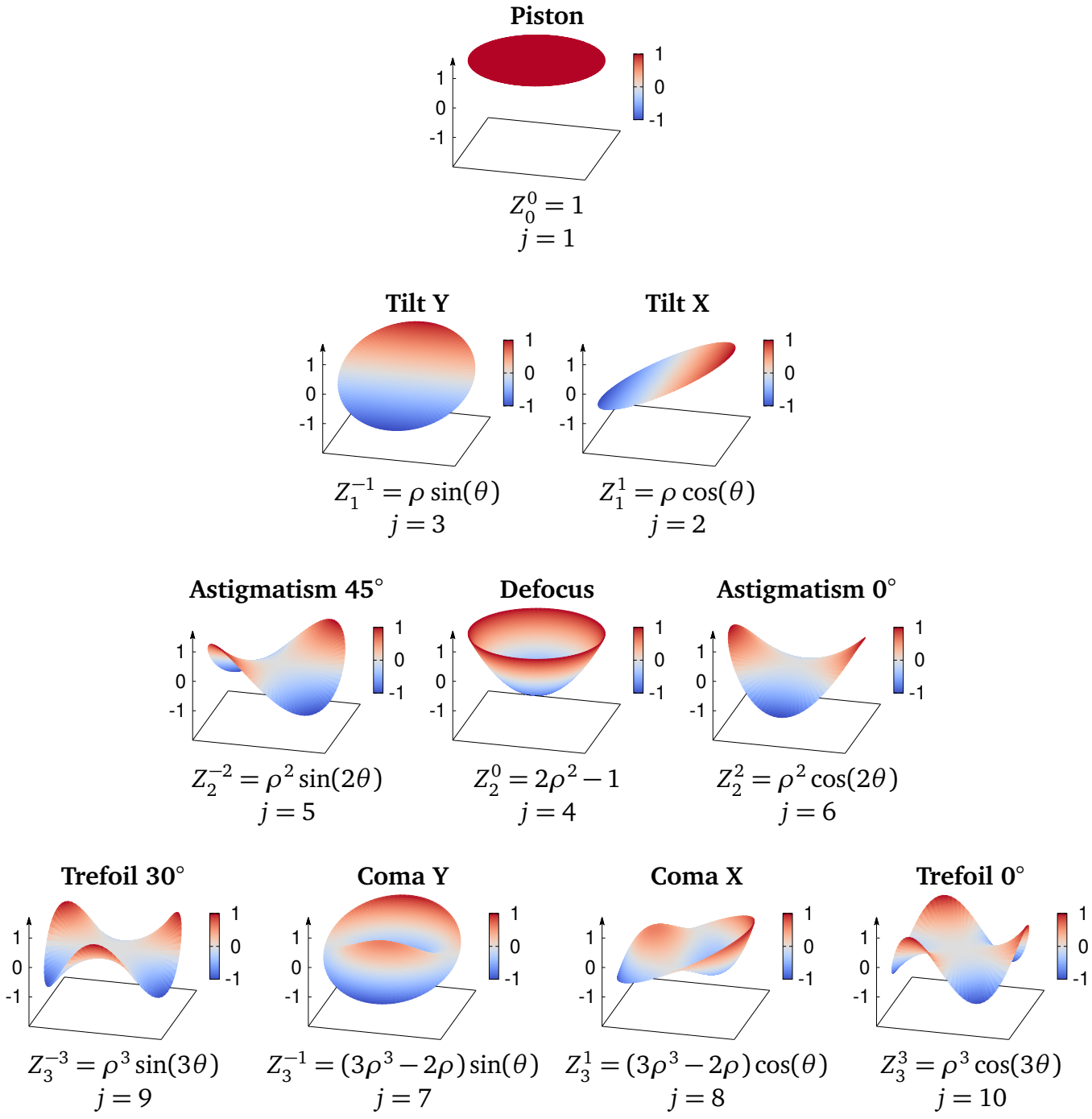

Figure 3.4: Plots of the first 10 Zernike aberrations for the $|R_n^m(1)| = 1$ normalization with their names, polynomial representation and Noll index [Ohland, 2018].

4 Cooled Amplifier Design

To counter the aberrations caused by thermal loading of the gain medium requires the development of a cooling concept for the laser amplifier. The goal of a pulsed large aperture Nd:Phosphate glass laser at a repetition rate of $^1/_5\,\mathrm{min}^{-1}$ requires a design that enables the active extraction of thermal energy deposited by consecutive pump processes. To enable compatibility with the existing PHELIX infrastructure, serving as both an upgrade to the existing facility and a test bed before integration into the 100 J diagnostic laser and Helmholtz beamline at FAIR, the new concept should be a modification of the legacy setup at PHELIX.

4.1 Initial Concept

To achieve the compatibility with the existing infrastructure, the new amplifier module requires a similar gain factor as the legacy modules at PHELIX with $G_0 \approx 1.5$. Using this gain factor as the target as well as equations (2.7) and (2.6), it is possible to estimate the required stored energy density in the glass as

$$E_{\mathrm{st}} = \frac{h\,c}{\lambda\,l\,\sigma} \ln G_0 = 0.403 \frac{\mathrm{J}}{\mathrm{cm}^3}. \tag{4.1}$$

By assuming that the remaining 89% of the required pump energy is converted into thermal energy in the discs this leads to a thermal energy density of $E_{\mathrm{therm}} = 3.59\,\frac{\mathrm{J}}{\mathrm{cm}^3}$. Using the volumetric heat capacity of typical phosphate glass ($\varrho c_p = 2.21 \frac{\mathrm{J}}{\mathrm{cm}^3 K}$) [Hu et al., 2014] the resulting temperature increase in the affected glass region can be estimated as

$$\Delta T = \frac{E_{\mathrm{therm}}}{\varrho c_p} \approx 1.62\,\mathrm{K}. \tag{4.2}$$

Since this temperature is not isotropically distributed in the glass, the beam quality is adversely impacted (see chp. 3.3 and 3.4) by the resulting thermal gradients. Chapter 3 has shown how these thermal gradients equilibrate within the material and how thermal energy can be be dissipated into the environment to restore the properties of the beam.
Equation (3.3) shows that high thermal conduction rates can be achieved in samples with high thermal conductivity λ, large areas A connected to the heat sink and short distances l to the heat sink. These thermal considerations would thus dictate a gain medium with high thermal conductivity and a large surface area while being as thin as possible (e.g. a thin disc) to reach optimal cooling efficiency.
However, the design of the amplifier needs to take into account more than thermal considerations. The damage threshold of the material requires the use of large beam diameters to reduce the intensity on the gain medium. To enable a homogeneous distribution of the pump energy in the medium for these beams, the pumplight has to be applied to the faces of the medium.

This *face-pumping* also requires thin discs of the gain medium with the faces oriented towards the beam, as this design will provide the most homogeneous distribution of pumplight over the depth of the medium. Since the most efficient cooling can be achieved by placing the heat sink in contact with largest surface of the gain medium, the heat sink thus has to be positioned in the optical path of the laser beam. Placement in the optical path requires the heat sink to be transparent to the laser wavelength as can be seen in figure 4.1. This can be achieved by using either liquid or gaseous coolants featuring the appropriate optical characteristic.

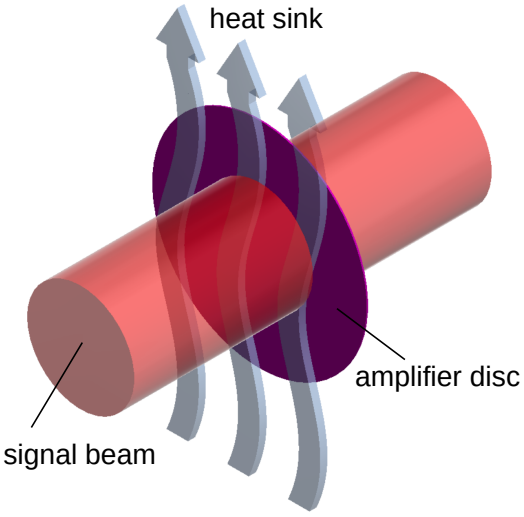

Figure 4.1: Concept of a thin amplifier disc with the coolant in the transmission plane of the laser.

Further geometrical constraints of the gain medium are set by the targeted amplification factor of ≈ 1.5, which depends on the stored energy in the gain medium requiring a certain thickness of the gain medium to propagate through (see (2.7)). From these consideration it is already apparent that there has to be a tradeoff between the thermal conduction and the gain factor as both are contrarily dependent on the thickness of the disc.
As the new amplifier is supposed to reproduce the amplification factor and wavelength of the old setup at PHELIX, the gain medium and overall thickness of the disc are dependent on the old design. The legacy amplifier modules at PHELIX use neodymium doped phosphate glass as the gain medium (discussed in chp. 2.2) with a thickness of 45 mm. Since phosphate glass features a rather low thermal conductivity of $\lambda \approx 0.56 \frac{\mathrm{W}}{\mathrm{m\,K}}$ the thickness of the disc has to be reduced to increase thermal conduction. To keep the amplification volume constant the ideal solution would be to replace the singular disc with several thinner discs of the same overall length in contact with the coolant (fig. 4.2a). A *split disc* design has also been proposed by other groups [Gaul et al., 2018] featuring several thin discs to increase cooling efficiency (e.g. fig. 4.2a). However, this solution is expensive as the procurement cost for amplifier glass discs is dominated by the polishing cost of the optical grade surfaces instead of the material volume.
To reduce procurement cost and complexity of our system, the preliminary concept features two discs of 25 mm thickness each and a single heat sink of forced convective cooling with either liquid or gaseous coolant in between the two discs as shown figure 4.2b. The discs therefore have a combined thickness of 50 mm, while the spatial expansion of the thermal gradient to the heat sink can reach a maximum of 25 mm. The increase in combined thickness compared to the legacy PHELIX system is to offer a potentially higher stored energy and the option to increase

the gain from the discs.
In the chosen concept the glass discs double as the constraining windows for the coolant and their outer surfaces are cooled via passive convective cooling with the ambient nitrogen atmosphere. Omission of cooling the outer surfaces was decided to further reduce the amount of media transitions in the system.

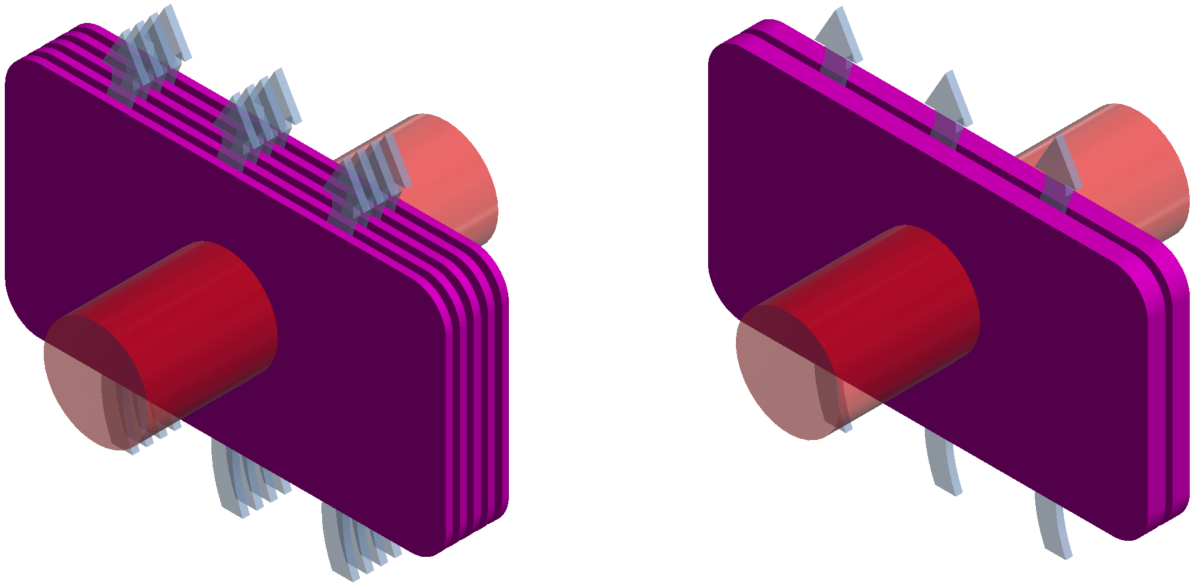

(a) Amplifier concept with five discs of 10 mm thickness each.

(b) Amplifier concept with two 25 mm thick discs.

Figure 4.2: Tow split disc configurations for a total disc thickness of 5 cm, approximating the thickness of the current PHELIX amplifier discs.

4.2 Coolant Flow

To avoid the introduction of lateral thermal gradients in the glass due to uneven cooling, it is necessary to design the coolant flow between the discs to be homogenous over the entire width of the discs.
Early simulations using the commercially available finite element software *CADFEM ANSYS* tested a simple design consisting of an inlet flange at the top, an outlet flange at the bottom and a thin fluid layer between the two amplifier discs. These simulations showed the formation of large vortices close to the center of the amplifier discs (fig. 4.3a) and thus the area most important to the beam quality. The vortices trap heated coolant and thus locally reduce the dissipation of heat from the amplifier discs.
To optimize cooling performance, it is therefore necessary to suppress the creation of vortices in the cavity between the discs and achieve a laminar flow over the entire width of the amplifier discs.
This can be achieved by distributing the flow from a single inlet flange to an array of inlet nozzles spread out over the width of the discs. The new setup creates a reservoir volume between the inlet and the nozzles which is used to hydro-statically distribute the pressure from the inlet. An initial design assumed a single elongated slit nozzle of the same width as the glass discs

to distribute the pressure. However, this concept was dropped due to the simulations showing the requirement of the slit opening to be below 0.5 mm to achieve equal pressure distribution which was deemed too small for reliable manufacturing. By selecting a design with several nozzles where the total area of all inlet nozzles is less than the area of the inlet flange, the pressure in the inlet reservoir is increased and equally distributed to the inlet nozzles. The simulation in figure 4.3b shows that the introduction of a nozzle array between the inlet and the cavity, as well as between the cavity and the outlet achieves a much more homogenous flow and reduces the size of vortices compared to the previous setup.
The nozzle array setup features a coolant flow direction from bottom to top which was chosen to flush bubbles out of the system.
It was further decided to shut off the coolant flow about 30 seconds before each shot to let the coolant settle and avoid the movement to influence the beam.

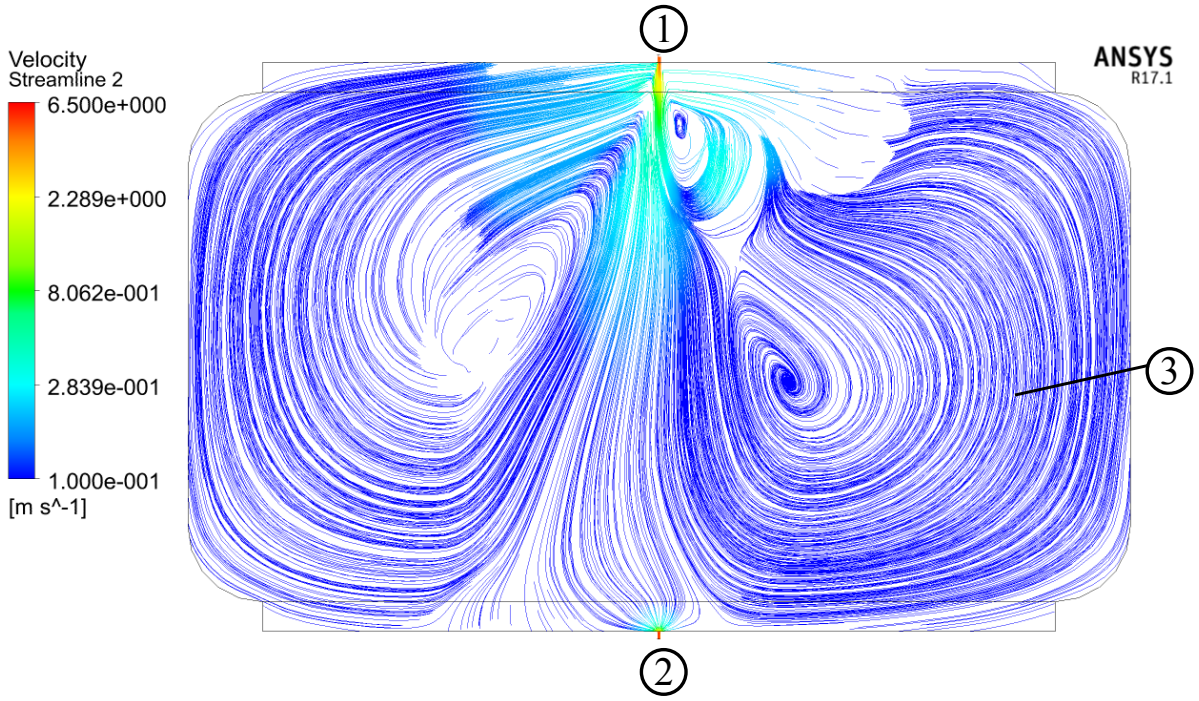

(a) Simulation of turbulence and vortex formation in a simple cavity setup, consisting of an inlet ①, an outlet ② and the cavity between the discs ③.

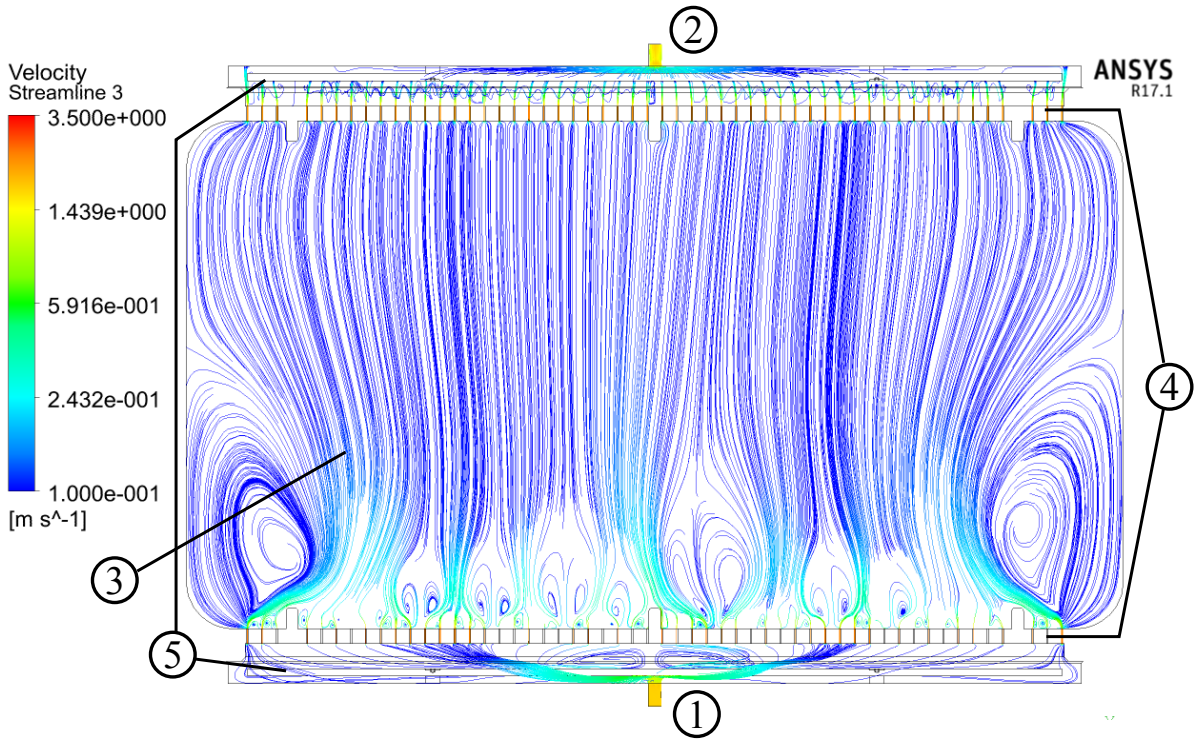

(b) Simulation of turbulence and vortex formation in a cavity equipped with additional nozzles ④ and reservoirs ⑤ for pressure equilibration in a *shower-head configuration*. Flow direction is reversed to flush out potential bubbles in the coolant.

Figure 4.3: Fluid-dynamics simulation of cooling fluids between two amplifier discs using CAD-FEM ANSYS CFX module on varying coolant flow setups. At this stage no suitable coolant had been identified yet and all simulations were conducted using water as a place holder fluid.

4.3 Prototype Design

To test the validity and performance of the proposed cooling concept, the design and construction of a full scale prototype amplifier module was necessary. The design is based on the split disc concept discussed above and features two neodymium doped phosphate glass (chp. 2.2) discs of 25 mm thickness each. The discs are cooled by a homogenous coolant flow created by the same shower-head configuration of nozzles and cavities shown in figure 4.3b.
Further emphasis during the design was placed on the modularity of the prototype to allow for rapid adjustments of various key components during the testing phase without requiring a redesign of the entire prototype.
This modularity is achieved by designing the prototype around a monolithic frame (fig. 4.4) with cutouts for the glass discs and the coolant cavity at its center. Additional cutouts are included in the top and bottom for the nozzle blocks and reservoir cavities. The frame further features mounting positions for the coolant seals as well as mounts for retainer elements for the glass discs, light shields, inlet and outlet adaptor plates and positioning.

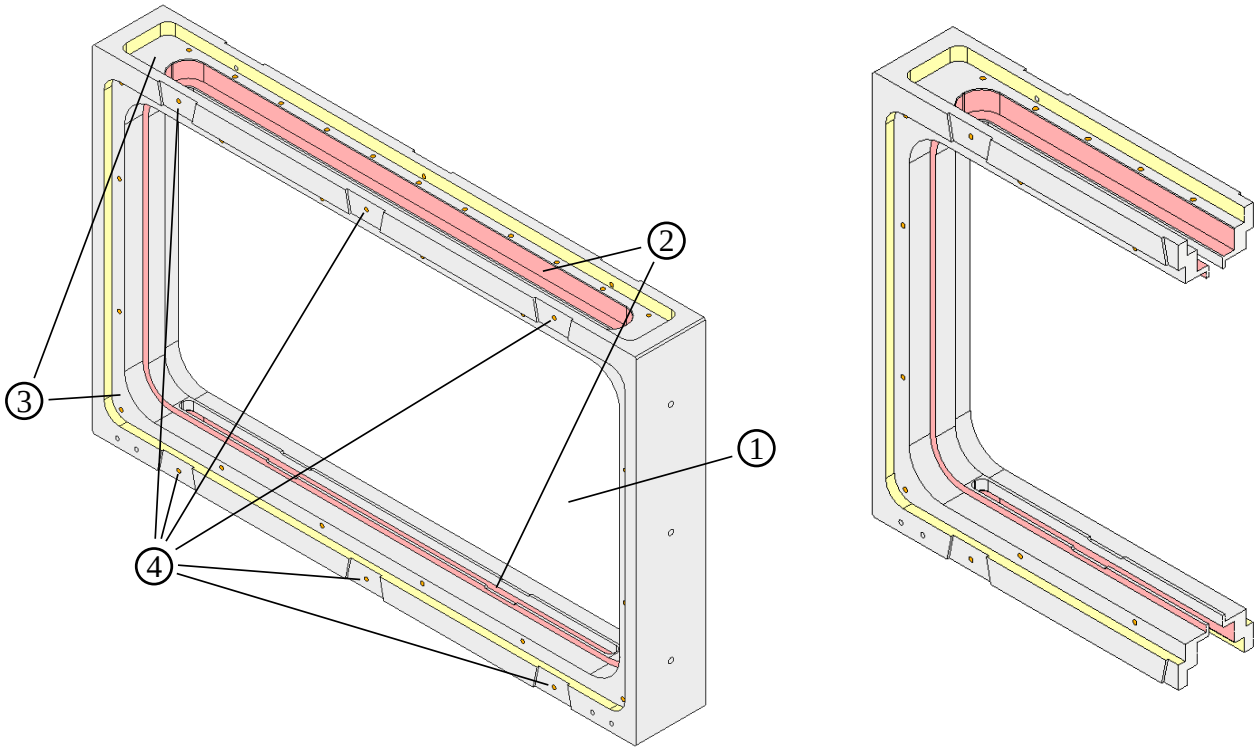

Figure 4.4: Schematic of the prototype module's central frame with its cutouts for the glass and coolant cavity ①, the nozzle and reservoir cavities ② as well as mountings for coolant seals ③ and retainer clamps ④.

4.3.1 Spacers and Nozzles

The coolant cavity is designed as a cutout in the frame and features the same lateral dimensions as the glass discs. This allows the glass discs to freely be moved in and out of the frame to adjust the coolant cavity length in beam direction and thus the thickness of the coolant layer between the discs. By mounting protruding spacers to the nozzle blocks it is possible to assemble the prototype with a predefined cavity length depending on the thickness of the spacers.
The cavity spacers further serve as support points for the discs during assembly and against the tension from the retainer screws on the discs. To avoid bending of the discs due to manufacturing inaccuracies, retainer screws are supposed to be used only at three points on each disc. The distribution of tension introduced by the retainer screws in the glass was simulated using Autodesk Inventor and the solution to minimize the accumulation of tension was found to be an equilateral triangle. This triangle formed the basis for the positioning of the spacers on the nozzle block seen in figure 4.5. To achieve compatibility between the upper and lower nozzle block, both feature spacer mountings in the center between two nozzles as well as one spacer on each side replacing a nozzle to form the base of the triangle.
The nozzle blocks further features mounting positions for additional spacers to prevent the glass discs from settling at the bottom of the cavity, with these spacers only mounted to the bottom nozzle block. This feature was included due to the potential of the settling glass discs to reduce tension on the seals causing coolant leakage at the top of the glass discs (see fig. 4.7).

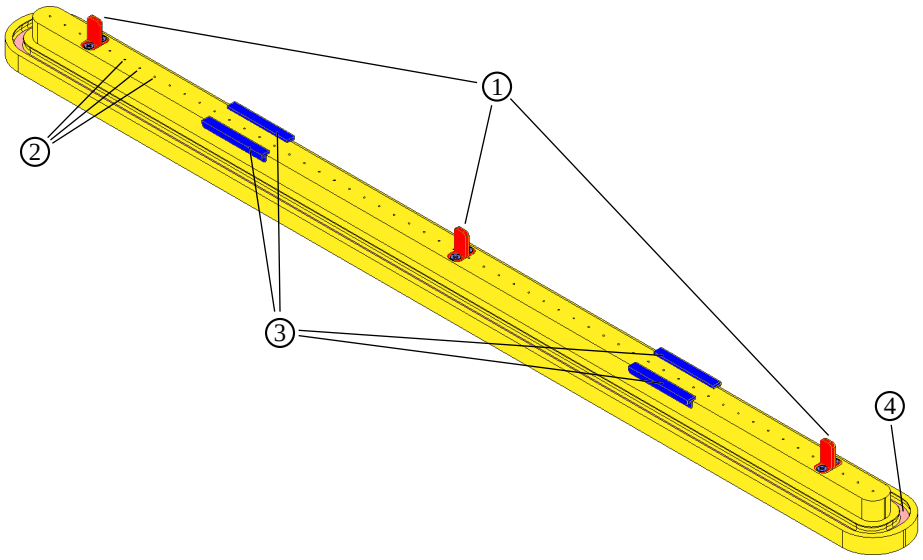

Figure 4.5: Schematic of the nozzle block with attached cavity spacers ①, nozzles ② with 10 mm separation, attached anti-settling spacers ③ for the bottom nozzle block and the O-ring groove ④ for sealing.

Besides hosting the spacers the primary function of the nozzle block is the equal distribution of the inlet pressure over the width of the cavity. To achieve this, the blocks are designed with 54 drill-holes of 1 mm diameter and spaced 10 mm apart along the center line to serve as the nozzles in the *shower-head configuration* (see fig. 4.3b). This design enables easy adjustments of the nozzle configuration by replacement of the modular nozzle blocks without necessitating

the redesign of the amplifier module.
Another important feature is leakage suppression. This is achieved by sealing the blocks against the central frame with an O-ring fixed in place by a groove running around the edge of the nozzle block.

4.3.2 Amplifier Discs

Since the amplifier design is supposed to be operated at the 100 J diagnostic laser at FAIR as well as the existing PHELIX laser, the design of the discs has to be able to accommodate the circular 30 cm diameter beam of PHELIX and the four circular 12 cm beams of the 100 J laser.
Due to the operation of the amplifier in the vicinity of the *Brewster angle* (see chp. 5.3.2 for details), the beam shape at the surface of the discs is a horizontally elongated projection of the original beam shape. The elongation can be described by a factor of $\cos(\theta_{\text{amb}})^{-1}$ which results in an elongation factor of ≈ 1.8 for an amplifier equipped with typical Nd:phosphate glass [Hu et al., 2014].
This elongation effect is further accompanied by the horizontal shift of the beam due to refraction at the ambient-glass and glass-coolant interfaces shown in figure 4.6.

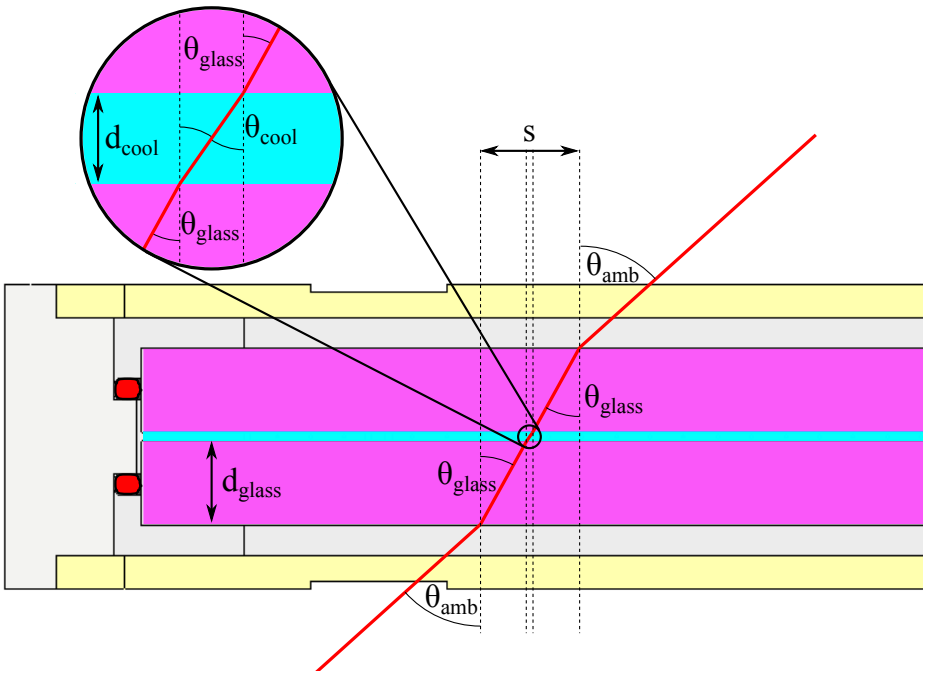

Figure 4.6: Horizontal shift of the beam due to refraction at ambient-glass and glass-coolant interfaces.

The horizontal beam shift in the amplifier module s can be calculated by

$$s = 2\, s_{\text{glass}} + s_{\text{coolant}} = 2\, d_{\text{glass}} \tan(\theta_{\text{glass}}) + d_{\text{cool}} \tan(\theta_{\text{cool}}) \tag{4.3}$$

with the shifts induced by the glass s_{glass} and the coolant s_{coolant} depending on the interior propagation angles in the glass θ_{glass} and coolant θ_{cool} as well as the thickness of the discs d_{glass} and the coolant layer d_{cool}. This shift has to be added to the elongated beam diameter of the beam

profile to gain the minimum horizontal dimensions required of the glass discs and amounts to ≈3.4 cm for the combination of Nd:phosphate glass and water with a coolant gap between the discs of 2 mm.
Combining the effects of horizontal elongation and shift of the beam for the circular beam profile of PHELIX with a diameter of 30 cm, the resulting elliptical beam shape on the amplifier discs features a major axis of 54.6 cm. With the addition of the beam shift, the discs require a minimum horizontal free aperture of roughly 60 cm to operate as part of the PHELIX setup.
The 100 J diagnostic laser at FAIR is planned to multi-pass a 12 cm diameter circular beam four times through different areas on the amplifier discs. To avoid overlap between the depleted areas and consecutive passes of the beams a square clear aperture of 32 cm x 32 cm was proposed. This aperture will be projected on the discs as a rectangel with a width of ≈58.2 cm using the same displacement as above.
From these considerations, the minimum dimensions of the rectangular free aperture for the amplifier could be estimated at a hight of 32 cm, a width of 61.7 cm and a thickness of 2.5 cm. The lateral dimensions of the prototype discs were increased to a hight of 34 cm and a width of 63 cm to accommodate for mounting space and tolerances.
These large lateral dimensions of the amplifier discs require the use of a cladding material at the edges of the discs to absorb spontaneous radiation in the pumped discs, preventing transverse lasing and the loss of stored energy.
The discs were further designed to feature rounded edges with a curvature radius of 32 mm for fitting of a large O-ring to prevent coolant from leaking around the glass discs.
Manufacturing of the amplifier discs was contracted to the *Shanghai Institute of Fine Mechanics* using their N31 neodymium doped phosphate glass [Hu et al., 2014] and a cladding glued to the glass via an index matched epoxy glue.

4.3.3 Coolant Sealing

Containment of the coolant inside the amplifier is provided by sets of O-rings at the nozzle blocks, the inlet and outlet adaptor plates as well as the glass discs. While the O-ring sealing at the adaptor plates and the nozzle blocks is achieved by applying pressure to the O-ring perpendicular to the sealing surfaces, this procedure can not be employed for the glass discs.
These phosphate glass discs are fairly brittle and tension in the discs can lead to stress induced birefringence effects (see chp. 3.3.2 for details). To avoid damages, the discs are to be held in place by screws made from soft materials, such as plastic, which will be thightened just enough to prevent the discs from moving due to the pressure exerted by the coolant. The necessary compression of the O-ring required for sealing therefore cannot be applied using the glass slab as a counteractor to the applied force.
The solution is the use of a solid frame with a protruding extension, shown in figure 4.7, which is mounted to the central frame and dimensioned such that no contact between the frame and the glass discs occurs. The O-ring is placed in a gap between the central frame and the glass discs which extends to the halfway point of the glass discs thickness. By tightening the mounting screws of the frame the protrusion acts like a piston and pushes the O-ring against the central frame. This leads to a compression and deformation of the O-ring, sealing the gap between the central frame and the glass discs (fig. 4.7b). The position of the O-ring at the center of the glass discs leads to a more even distribution of residual forces from the O-ring to the glass.

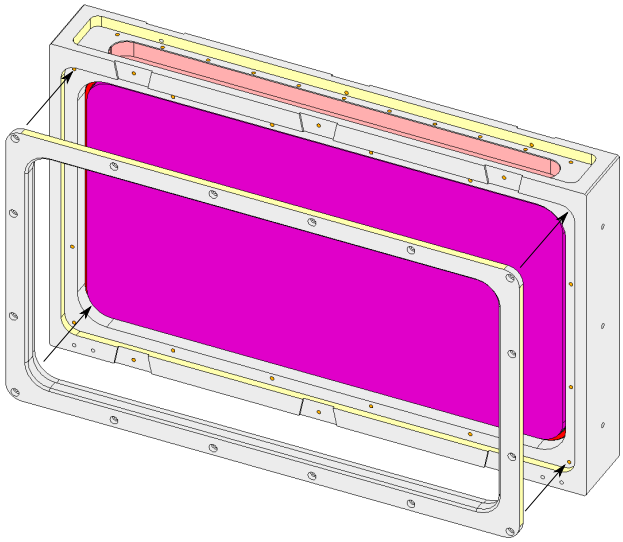

(a) Schematic of the assembly of central frame, piston frame and glass discs.

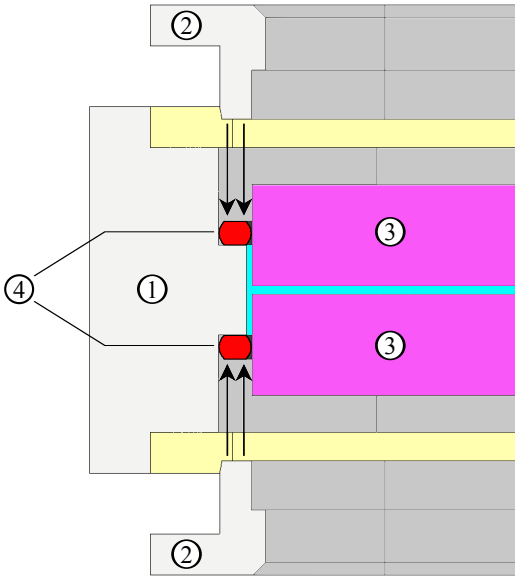

(b) Half cut view of the central frame ① from above, the piston frame ② and the glass discs ③ showing the compression scheme of the O-rings ④ to contain the coolant in the cavity.

Figure 4.7: Schematics of the designed sealing solution to contain the coolant in the cavity between the amplifier discs while reducing the stresses on the glass.

4.3.4 Coolant Management

As discussed in chapter 4.2 it is advantageous to apply a flow direction of the coolant from bottom to top to flush out any potential bubbles forming in the cavity between the discs. This consideration is also included in the design of the coolant supply connected to the amplifier, seen in figure 4.8.

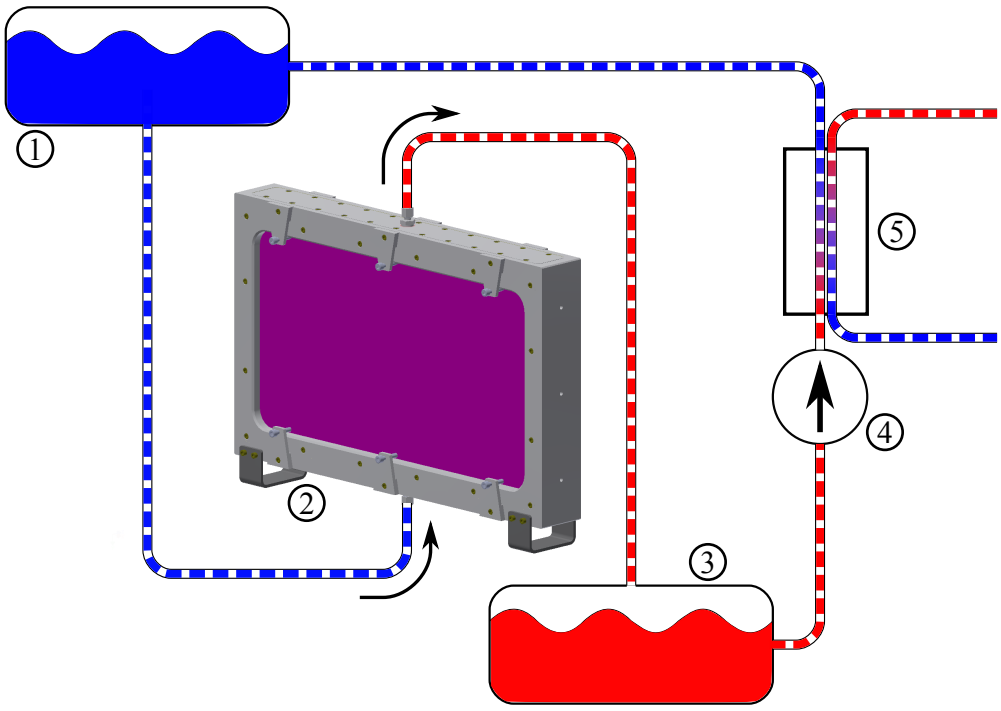

Figure 4.8: Flow diagram of the coolant supply featuring the elevated coolant supply tank ①, the amplifier module ②, the coolant drainage tank ③, the pump ④ to recirculate the coolant and a heat exchanger ⑤ to resupply cool liquid to the supply tank.

The system is designed as a closed cycle cooling system to avoid the loss of expensive coolant. Since vibrations from the coolant pumps can cause misalignment of amplifier parts between two pulses a vibration free methode of supplying the coolant to the amplifier had to be developed. The solution is the use of hydrostatic pressure from an elevated coolant reservoir to supply the coolant to the amplifier, while a reservoir at lower elevation than the module serves as the drain. Coolant can than be pumped from the drain to the supply reservoir using a motorized pump, while passing though a heat exchanger connected to a cooling water supply to cool the heated coolant down to operating temperature. Via this method an effective decoupling of the amplifier module from the vibrating pump can be achieved.
To further reduce the impact of flowing coolant during the operation of the laser, valves at the inlet and outlet of the amplifier module will be closed 30 seconds prior to an amplification event to provide time for the coolant to settle.

5 Coolant

The simulations to optimize the coolant flow used water as a benchmark cooling fluid but optimization of the cooling process as well as optical and chemical constraints required the investigation of additional fluids. To this end, a variety of chemicals were selected by their published data ([Hale and Querry, 1973], [Vargaftik, 1975], [Otanicar et al., 2009], [Kedenburg et al., 2012]), manufacturer's data and supplemented by experimental results measured at GSI and TU Darmstadt. The investigated fluids consisted of

- liquid water,
- dry nitrogen gas,
- ethylene-glycol,
- Cargille S1050,
- F2 Chemicals Flutec PP1,
- F2 Chemicals Flutec PP2,
- F2 Chemicals Flutec PP3,
- F2 Chemicals Flutec PP6 and
- F2 Chemicals Flutec PP80.

Liquid water was chosen as a potential coolant for its large heat capacity, low viscosity and high availability.
Nitrogen gas offers the advantage of chemical stability and low absorption of the laser wavelength and as such it is already in use inside the PHELIX amplifier as a quenching gas. Use of nitrogen gas would also considerably reduce the risk of damages in case of a coolant leakage.
Ethylene-gylcol is already used as a coolant in technical applications such as car engines, thus it was also considered as a potential coolant for our amplifier as it features a considarable heat capacity and a refractive index close to the amplifier discs.
Cargille S1050 is a product by *Cargille Laboratories*, it consists of a liquid blend of siloxane and various aliphatic and alicyclic hydrocarbons but the exact composition is a corporate secret. It was chosen due to its refractive index being close to the refractive index of the amplifier material and its low absorption of the laser wavelength.
The various liquids by *F2 Chemicals* are fully-fluorinated fluorocarbons of differing carbon-chain length, featuring a high chemical and thermal stability.
During this research, three major topics emerged by which to rate potential fluids which will be discussed in this chapter, the *thermal and kinematic properties* of the fluids, their *chemical compatibility* with the gain medium and their *optical properties*.

5.1 Thermal and Kinematic Properties

Thermal and kinematic properties are two important features in a cooling fluid, as they define the behaviour of the coolant in regards to the exchange of thermal energy from the thermally loaded body to the coolant and thus the efficiency of the cooling process.

One important thermal feature of a potential coolant is its ability to absorb large amounts of thermal energy without drastic changes in its temperature. The importance of this can be seen in (3.5), where the thermal energy flux depends on the temperature differential between the coolant and the surface of the thermally loaded body. The dependence of a coolant volume's temperature change on its absorbed thermal energy can be expressed in the *volumetric heat capacity* which can be calculated by multiplying the density of a material with its specific heat capacity (ϱc_p). The volumetric heat capacity should ideally by as large as possible to reduce the impact of coolant heating on the cooling process.
Another important thermal feature of the coolant is the temperature range between its phase transitions. The specification to operate the amplifier at room temperature requires coolants in this temperature range to be either liquid or gasseous with no phase transitions between 0 °C and 50 °C as a safety margin. All chosen coolants for this research have been screened to avoid phase transitions in this temperature range. While evaporation cooling is a possible cooling mechanism, it is however impractical for our application and was thus not investigated.

One kinematic feature important for a cooling system is the viscosity of the fluid. Low viscosity fluids allow for higher flow rates at the same drive pressure compared to high viscosity fluids. This becomes important due to the limited amount of pressure that can be applied to the system without deteriorating the optical performance of the glass discs as will be discussed in chapter 7.3. High flow rates are desirable to provide a rapid exchange of the coolant volume between the discs. This rapid exchange is necessary to mitigate the effect of the coolant absorbing heat in the regions closer to the inlet, therefore providing a less effective heat sink to glass regions further along the coolant path and thus lower thermal exchange rates which will lead to uneven cooling of the amplifier glass.

In practice, viscosity and heat capacity complement each other and the reduced flow rate of high viscosity fluids can be compensated, if they feature an increased heat capacity compared to fluids with low viscosity and low heat capacity. There are, however, limits to this compensation, by using the law of energy conservation the amount of thermal energy which needs to be extracted from the discs and absorbed by the coolant can be calculated as

$$\Delta Q = \varrho c_{p,g} \cdot V_g \cdot \Delta T_g = \varrho c_{p,c} \cdot V_c \cdot \Delta T_c, \tag{5.1}$$

where ΔQ is the thermal energy removed from the glass, $\varrho c_{p,g}$ and $\varrho c_{p,c}$ are the volumetric heat capacities of the glass and coolant respectively, $V_{g/c}$ the volumes and $\Delta T_{g/c}$ the respective changes in temperature.

Coolant	$\varrho c_{p,c}\left(\frac{J}{cm^3K}\right)$	$V_c\left(m^3\right)$	$\eta\ (mPa\,s)$	$v_{\text{cav}}\left(\frac{m}{s}\right)$	Re_{cav}
water	4.173	0.459	0.890	1.22	462.9
nitrogen (gas)	0.117	16.344	0.018	43.24	83,062.9
ethylene-glycol	2.742	0.699	20.810	1.85	33.5
Cargille S1050	1.726	1.111	13.000	2.94	64.7
F2 Flutec PP1	1.833	1.046	0.656	2.77	2,411.6
F2 Flutec PP2	1.722	1.113	1.561	2.95	1,147.1
F2 Flutec PP3	1.760	1.089	1.919	2.88	933.1
F2 Flutec PP6	1.854	1.034	5.100	2.74	349.7
F2 Flutec PP80	1.842	1.040	2.950	2.75	583.4

Table 5.1: Volumetric heat capacity, required exchange volume, viscosity, estimated flow velocity in the cavity of the amplifier and the resulting Reynold's number.

By assuming an increase of the discs' temperature by ≈1.62 K (eqn. (4.2)) due to the pumping process and a maximum permissible increase of the coolant temperature of ≈0.01 K, equation (5.1) can be solved to calculate the necessary exchange volume of the coolant V_c.
The results in table 5.1 show that the low volumetric heat capacity of gasses such as nitrogen compared to the liquid coolants leads to the necessity to provide a far larger coolant volume to absorb the heat stored in the glass discs.
By dividing the exchange volume by the cross section of the cavity $A_{\text{cav}} = 63\,\text{cm}$ x $0.2\,\text{cm}$, the flow velocity and Reynold's number of the coolant between the cavity can be calculated. The Reynold's number serves as an indicator for the laminarity of a flow process, with the critical Reynold's number for the transition from a laminar to a turbulent flow in a tubular geometry usually set at $Re_{\text{crit}} \approx 2300$ [Rotta, 1956]. By comparing the Reynold's numbers in table 5.1 to the critical Reynold's number, the results show a clear tendency of the gasseous coolant nitrogen to exhibit a turbulent flow compared to the liquid coolants. This turbulent flow was regarded as a potential risk to the operation of the amplifier due to the vibrations caused by the turbulences. These vibrations could cause misalignment of the system during the cooling phase, requiring readjustment of the amplifer after each cooling cycle and thus deminishing the gains in repetition rate achieved by cooling. To avoid the issue of flow velocity induced vibrations nitrogen was excluded from any further research into the coolants.

5.2 Chemical Compatibility

Aside from the thermal performance of the fluids, a critical feature of the potential coolants is their chemical compatibility with various components in the amplifier. While the material choice for many parts of the amplifier can be adjusted during the manufacturing phase to fit the coolant, the chemical composition of critical parts such as the gain medium and its cladding are unalterable.
While water has shown the best combination of thermal and kinematic parameters, its chemical features result in corrosion damages to the glass surface. The corrosion process and its sources have been studied in [Li et al., 2018] for the same glass used in this project. Corrosion could be identified to occur in two stages, the first stage consisting of ion-exchange processes between the water and the glass structure while in the second stage the corrosion is dominated by hydrolysis

of some of the glasses chemical constituents. The latter stage causes structural changes to the glass surface in the tens to hundreds of micrometer range. Surface defects of this size range will be detrimental to the beam quality in the short term, while defect growth might render the glass useless in the long term.
A second process by which water can have a destructive effect on phosphate glass is the growth of existing micro-fractures from thermal loading or manufacturing defects. Cracks can propagate from these fractures even at mechanical stress levels below the point of critical failure by stress-enhancing chemical reactions of glass and water at the crack tip [Suratwala et al., 2000]. These cracks will also deteriorate the optical performance of the glass disc as well as causing eventual structural failure after prolonged operation.
From the results of these publications it is apparent that water, though featuring the best combination of thermal and kinematic properties, should not be used as a coolant to preserve the glass discs.

A further chemical constraint on the coolants is set by the application of an absorbant cladding to the amplifier discs. This cladding serves to mitigate the effect of transverse lasing in the discs and is bonded to the glass via an index matched epoxy glue by the manufacturer SIOM (Shanghai Institute of Optics and Fine Mechanics). To avoid the dissolution of the bonding between the glass and the cladding, any potential coolant has to be chemically inert towards the epoxy compound. Since the composition of the epoxy glue is a manufacturer secret, a sample of the Cargille S1050 liquid was sent to SIOM for compatibility testing along an ethylene-glycol sample provided by SIOM. The Flutec liquids were not used in these tests as the inherent chemical inertness of the perfluorinated hydrocarbons was deemed a sufficient safeguard against chemical damages to the glass, cladding or glue.
The tests submersed a sample of cladding attached to the glass in the potential coolant and utilized accelerated aging at 60 °C. The results of these test showed that ethylene-glycol will dissolve the glue, disqualifying it as a potential coolant in the amplifier while Cargille S1050 does not seem to interact with the glue on a chemical level and could thus be used in further investigations.
Cargille S1050, however, did feature known incompatiblities with common construction materials provided in the manufacturers data sheet, resulting in constraints on the materials used in the construction of the amplifier module where the Flutec liquids did not impose any restrictions on the choise of materials.

5.3 Optical Properties

Since the concept of the amplifier, described in chapter 4.1, requires the laser beam to be transmitted through the coolant, further considerations on the optical properties of the coolants and their influence on the laser beam are required. For the amplifier to deliver the required amplification gain, losses in the amplifier have to be kept to a minimum. These losses can be distinguished as absorption losses by attenuation of the beam energy in the coolant and reflection losses at the interfaces between the coolant and the laser glass.

5.3.1 Absorption Losses

Absorption losses occur due to photons of the laser beam being absorbed by coolants as either electron excitations or excitations of rotational or vibrational modes in the coolants molecule. These excitations can either reemit the light in a random direction by spontaneous emission or convert it into thermal energy inside the coolant. The absorption spectra of each coolant are unique to its composition and depend on the wavelength of the incident light.
The attenuation of light in a material can be calculated using the *Beer-Lambert law*

$$T(d) = e^{-\alpha(\lambda)d} \tag{5.2}$$

where the transmittance $T(d)$ of a medium of length d can be calculated from the exponential of d and the wavelength dependent attenuation coefficient $\alpha(\lambda)$.
The Beer-Lambert law shows that an increase in transmittance can be achieved by reducing the thickness of the absorbing material. In the case of the amplifier, this translates into the requirement to design the coolant layer and thus the cavity between the discs as thin as possible.

Absorbance Measurement of Coolants

Equation (5.2) further shows the importance of the wavelength-dependent absorption coefficient on the attenuation of the beam intensity. It is therefore important to gain accurate data on the absorption spectra of the coolants.
Data for widely used liquids such ethylene-glycol is readily available and can be found in [Otanicar et al., 2009]. Although the absorption characteristics of the Cargille S1050 fluid were provided in the data sheet by Cargille [Cargille, 2018], the acquisition of the absorption data for the *Flutec* coolants by F2 Chemicals proved to be more difficult. The company was able to provide absorption data for some of the liquids in the far infrared range but could not provide data for the required wavelength of 1053 nm since none of these liquids had originally been intended for optical applications. To evaluate the suitability of the Flutec liquids as transmissive coolants it became necessary to measure the absorption characterisitics experimentally. By establishing contact with the *Eduard-Zintl-Institut für Anorganische Chemie und Physikalische Chemie* from the Technische Universität Darmstadt, it was possible to gain access to their V-770 UV-Visible/NIR Spectrophotometer. This device is a commercial system by *Jasco*, capable of measuring the absorption spectra of samples in the wavelength range from 190 to 2700 nm, thus covering the required wavelength region of the laser.
By measuring the transmitted intensity with and without a sample present, the device software calculates the spectral absorbance $A(\lambda)$ of the sample. The spectral absorbance is a spectrometric value defined as

$$A(\lambda) = \log_{10}\left(\frac{I_0(\lambda)}{I_s(\lambda)}\right) \tag{5.3}$$

where $I_s(\lambda)$ is the wavelength dependent attenuated intensity while $I_0(\lambda)$ is the unattenuated reference intensity which is measured without a sample at the given wavelength. The absorbance can be related to the absorption coefficient by

$$\alpha(\lambda) = \frac{\ln(10)}{l} \cdot A(\lambda) \tag{5.4}$$

and depends on the irradiated sample length l.
Mesurements were performed on samples of Cargille S1050, the F2 Chemicals Flutec liquids and ethylene-glycol to serve as a reference.

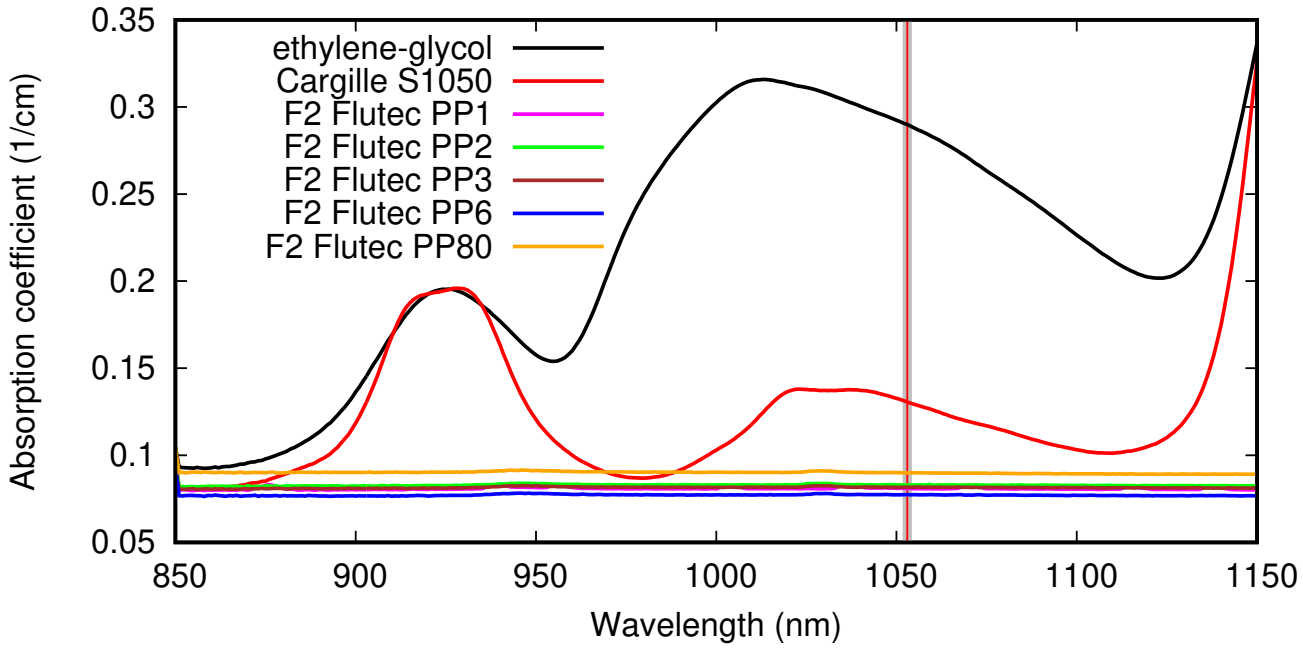

Figure 5.1: Excerpt of the measured absorption spectra for various liquids around the targeted laser wavelength of 1053 nm, denoted by the vertical line. Measurements performed with the Jasco V-770 UV-Visible/NIR Spectrophotometer at the Eduard-Zintl-Institut für Anorganische Chemie und Physikalische Chemie. Absorption accuracy specified as $\pm 0.0035\,\mathrm{cm}^{-1}$ between 0 and $1.15\,\mathrm{cm}^{-1}$.

The results presented in figure 5.1 show a strong absorption of the laser wavelength in ethylene-glycol compared to all other potential coolants.
The Cargille S1050 liquid also features an elevated absorption at 1053 nm to the Flutec liquids which feature consistently low absorption coefficients of less than $0.1\,\mathrm{cm}^{-1}$ over the entire visible and near IR spectrum.
Comparing the Flutec liquids to each other, figure 5.1 shows that PP1, PP2 and PP3 feature almost the exact same absorption coefficients in the spectral region of the laser wavelength as their absorption lines are virtually indistinguishable. Only PP6 and PP80 show slight variations to the other Flutec liquids, with PP80 featuring a slightly higher absorption coefficient while PP6 exhibits a slightly lower absorption in the visible to near IR spectrum.
These measurements lead to the conclusion that F2 Chemicals Flutec PP6 offers the least absorption losses out of all liquids tested for our application.

5.3.2 Reflection Losses

Another process by which beam intensity is lost in the amplifier are reflections which occur at every interface between two media with differing refractive indices. In the amplifier module, these interfaces exist between the surrounding quenching gas and the glass discs as well as the

glass discs and the coolant. Reflection losses denote the beam intensity lost due to primary reflections at each of these interfaces.
The reflectance and transmittance for an interface can generally be calculated using *Fresnel equations* [Driggers, 2003] for normal (s) and parallel (p) polarized light:

$$R_s = \text{abs}\left[\frac{n_i \cos\theta_i - n_t\sqrt{1-\left(\frac{n_i}{n_t}\sin(\theta_i)\right)^2}}{n_i \cos\theta_i + n_t\sqrt{1-\left(\frac{n_i}{n_t}\sin(\theta_i)\right)^2}}\right]^2 \tag{5.5}$$

$$R_p = \text{abs}\left[\frac{n_i\sqrt{1-\left(\frac{n_i}{n_t}\sin(\theta_i)\right)^2} - n_t\cos\theta_i}{n_i\sqrt{1-\left(\frac{n_i}{n_t}\sin(\theta_i)\right)^2} + n_t\cos\theta_i}\right]^2 \tag{5.6}$$

$$T_{s,p} = 1 - R_{s,p} \tag{5.7}$$

with the incidence angle θ_i, the reflectance $R_{s,p}$ and transmittance $T_{s,p}$ as well as the refractive indices $n_{i,t}$ for the incidence and transmittance side of the interface. From (5.5) and (5.6) follows that for given incidence angles the reflectance of systems where n_i and n_t are closely matched approaches zero.

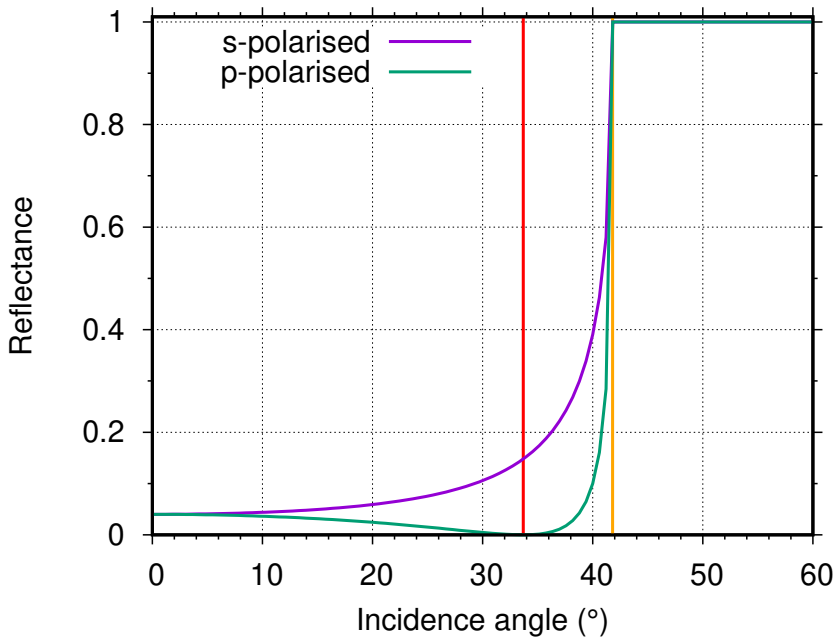

Figure 5.2: Reflectance at the interface of two media with $n_i > n_t$ with the Brewster angle (red) and the critical angle for total reflection (orange).

By plotting the Fresnel equations for $n_i > n_t$ (fig. 5.2) two interesting regions become apparent. One of these regions is the *Brewster angle*, at which p-polarized light does not incur any reflection losses as the reflectance drops to zero.
The second region is the *critical angle* for *total internal reflection*, it defines the minimum angle at which light can no longer pass the boundary between the two media and all energy is reflected. This critical angle is highly dependent on the refractive indices of the media involved and features a sharp change in intensity over a small region of incidence angles thus providing

a sensitive methode for measuring the refractive index.

Total Internal Reflection Refractometer

Since equations (5.5) and (5.6) depend strongly on the refractive indices of the media involved, determining these indices become an important topic. However, as with the absorption spectra of the coolants, data on the refractive index at a wavelength of 1053 nm was not available for all of the liquids and experimental measurements had to be conducted. Since no refractometer was available for measurements of the refractive index at 1053 nm a setup had to be designed.

Using the sensitivity of the intensity under total internal reflection on the incidence angle of the beam, an experimental setup was devised based on the Abbe-refractometer design [Abbe, 1906]. The concept for the experimental setup is displayed in figure 5.3a and consists of a laser diode ① at 1053 nm, a prism ② with a well-known refractive index, a small reservoir made from acrylic glass glued to the prism to hold the liquid ③ and a photo diode ④ to measure the transmitted intensity.

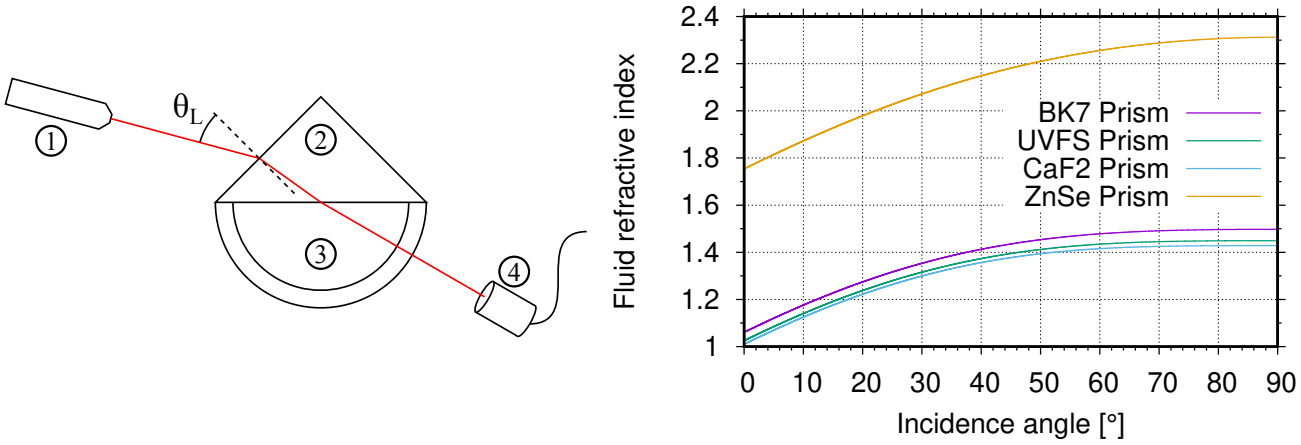

(a) Schematic of the experimental setup for a total internal reflection refractometer.

(b) Plotted response function of the refractometer for various prism materials.

Figure 5.3: Preliminary considerations on the setup and material choices for a total internal reflection refractometer.

By finding the incidence angle corresponding to the critical angle at the glass-liquid interface the refractive index of the fluid can be calculated using *Snells law* and the geometric relations inside a rectangular triangle, yielding

$$n_f = n_p \cdot \sin\left(\frac{\pi}{4} + \arcsin\left(\frac{\sin\theta_L}{n_p}\right)\right) \tag{5.8}$$

where n_f and n_p are the refractive indices of the fluid and the prism respectively, the refractive index of air is assumed to be unity and θ_L is the incidence angle at the prism-air interface (see fig. 5.3a).

To change the incidence angle the prism and reservoir are mounted to a manually adjusted roation stage with the detector mounted to an arm on a second rotation stage to follow the shifting beam exiting the reservoir.
The prism material was chosen from the *Thorlabs* catalog after plotting (5.8) for the refractive indices provided by Thorlabs for BK7, UV fused silica, calcium fluoride and zinc selenide. From figure 5.3b it is apparent that the method is limited to a certain range of measurable refractive indices depending on the choice of prism material.
The index range was set between 1.2 and 1.45 to cover the known refractive index of Flutec PP6 at 589 nm which was provided by the manufacturer as 1.313. It was assumed that index deviations due to the different wavelength of interest at 1053 nm would be small enough to fall within this region. Furthermore, since the remaining Flutec liquids featured similar chemical compositions and absorption behaviour as PP6, it was assumed that the deviations between the Flutec liquids would also be small.
Figure 5.3b shows that the refractive index range between 1.2 and 1.45 can be realiably measured using a BK7 prism.

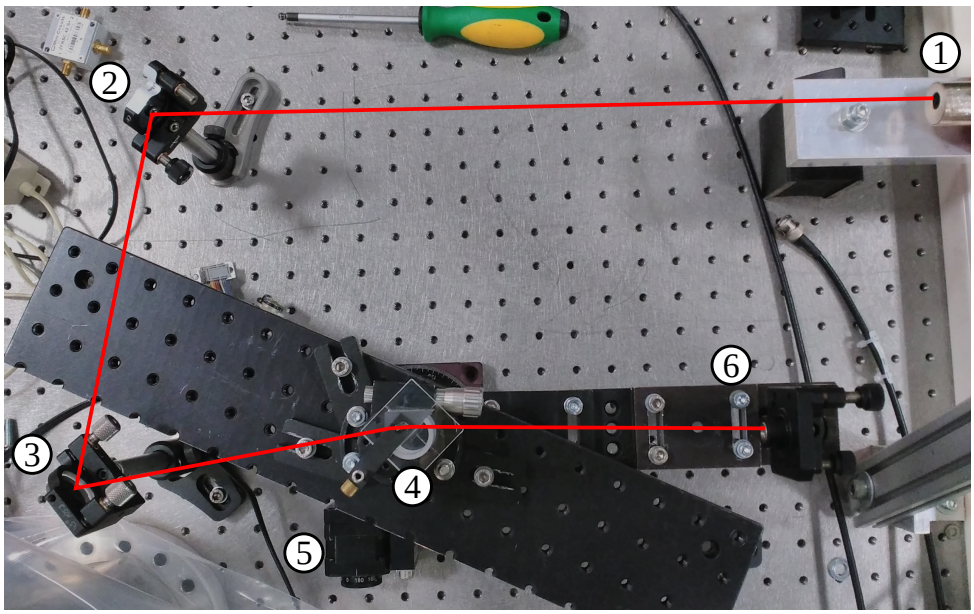

Figure 5.4: Experimental setup of the total internal reflection refractometer consiting of a small cw-laser at 1053 nm ①, two mirrors ② & ③ to adjust the pointing of the beam, the prism with the attached reservoir ④ mounted to a rotating stage, a second rotating stage ⑤ to adjust the position of the detector and an arm holding the detector ⑥.

After the construction of the experimental setup (fig. 5.4) measurements were first conducted on the known liquids water and ethanol to refine the measurement process and validate the methode by comparing the experimental results to the refractive index provided in [Hale and Querry, 1973] and [Kedenburg et al., 2012].
Measurements of Cargille S1050 could not be conducted as the samples had been given to the Shanghai Institute of Optics and Fine Mechanics to test the chemical compatibility with the amplifier glass. However, since the refractive index of Cargille S1050 was well documented in the manufacturers data sheet the omittance of the refractive index measurements on S1050 was deemed acceptable. The unknown refractive indices of the Flutec liquids were finally measured by utilizing the methode described above.

Liquid	n	Δn	$n_{\mathrm{lit}}(1053\,\mathrm{nm})$
water	1.318	±0.009	1.326
ethylene-glycol	-	-	1.423
ethanol	1.355	±0.001	1.355
Cargille S1050	-	-	1.442
Flutec PP1	1.258	±0.003	-
Flutec PP2	1.281	±0.001	-
Flutec PP3	1.290	±0.002	-
Flutec PP6	1.313	±0.002	-
Flutec PP80	1.278	±0.003	-

Table 5.2: Compilation of measured refractive indices and literature data

The measurements conducted with the setup were limited by the accuracy of the manually operated rotation stage and the ability to determine the intensity drop of the transmitted light with the photo diode. The measurement scale of the rotation stage enabled an accuracy of several arcseconds for the incidence angle resulting in an accuracy of the refractive index of < 0.01. From the data presented in table 5.2 it is apparent that the Cargille S1050 liquid and ethylene glycol feature the closest match of all examined liquids to the refractive index of the amplifier glass at 1.53 and would thus feature the lowest reflection losses for a given incidence angle. However, as discussed at the beginning of this chapter, the transmission of the amplifier depends on the interaction between reflection losses and absorption losses, thus a combined analysis is necessary.

5.3.3 Transmission

By operating the laser in p-polarisation and mounting the gain medium at the *Brewster angle*, figure 5.2 shows that the reflectivity of the interface drops to zero thus eliminating the reflection losses. However, a system consisting of media with more than two differing refractive indices involved requires a combined equation to express the transmission without the losses incurred at each of the interfaces. In the case of a liquid cooled amplifier with two discs, the combined equation for the transmittance of a p-polarized beam can be derived by using (5.7) to yield

$$T(\theta_i) = (1 - R_{A\to G}(\theta_i)) \cdot (1 - R_{G\to F}(\theta_G)) \cdot (1 - R_{F\to G}(\theta_F)) \cdot (1 - R_{G\to A}(\theta_G)) \tag{5.9}$$

where $T(\theta_i)$ is the transmittance achieved at the incidence angle θ_i of the beam on the amplifier, $R_{A\to G}$ is the reflectance at the ambient to glass interface, $R_{G\to F}$ is the reflectance between glass and fluid, $R_{F\to G}$ between fluid and glass and $R_{G\to A}$ the reflectance at the glass to ambient interface. By using geometric correlations in the plan-parallel setup of the amplifier (fig. 5.5) and Snells law the incidence angles at each interface can be expressed by the incidence angle of the beam relative to the amplifier:

$$\begin{gathered} n_A \sin\theta_i = n_G \sin\theta_G \quad , \quad n_G \sin\theta_G = n_F \sin\theta_F \\ \Rightarrow n_A \sin\theta_i = n_F \sin\theta_F . \end{gathered}$$

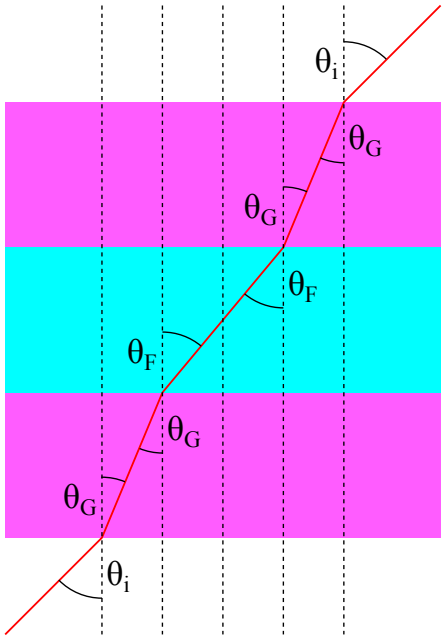

Figure 5.5: Angles and relations in the plan-parallel setup of the glass discs and cooling liquid.

Using these correlations with equation (5.6) one finds that $R_{A\to G}(\theta_i) = R_{G\to A}(\theta_G)$ and $R_{G\to F}(\theta_G) = R_{F\to G}(\theta_F)$. However, the Brewster angles for the Ambient-Glas and Glas-Fluid interfaces are not identical and thus no single angle exists that reduces the reflection losses to zero.
By angeling the amplifier relative to the beam, the beam path through the coolant is changed, thus modifying the absorption losses in the coolant. The transmittance of the coolant described in (5.2), thus has to be modified to account for the incidence angle on the fluid θ_F:

$$T_{\text{cool}}(d, \theta_F) = \frac{I}{I_0} = e^{-\alpha(\lambda)\frac{d}{cos(\theta_F)}} \tag{5.10}$$

Combining (5.9) and (5.10) and expressing all angles in relation to the incidence angle of the beam on the amplifier a combined equation for the transmittance of the amplifier can be derived as

$$T(d, \theta_i) = (1 - R_{A\to G}(\theta_i))^2 \cdot (1 - R_{G\to F}(\theta_i))^2 \cdot T_{\text{cool}}(d, \theta_i). \tag{5.11}$$

By plotting (5.11) using the absorption coefficients presented in figure 5.1 and the refractive indices of the coolants from table 5.2, figure 5.6 shows that an optimum angle exists for maximizing the transmittance of the amplifier, depending on the coolant. The transmittance behaviour with respect to the different coolants exhibits a considerable deviation of the maxima from the Brewster angle, which is especially pronounced in the Flutec liquids. This behaviour shows the necessity to operate the amplifier at a different angle than the Brewster angle to avoid excessive intensity losses in the module.

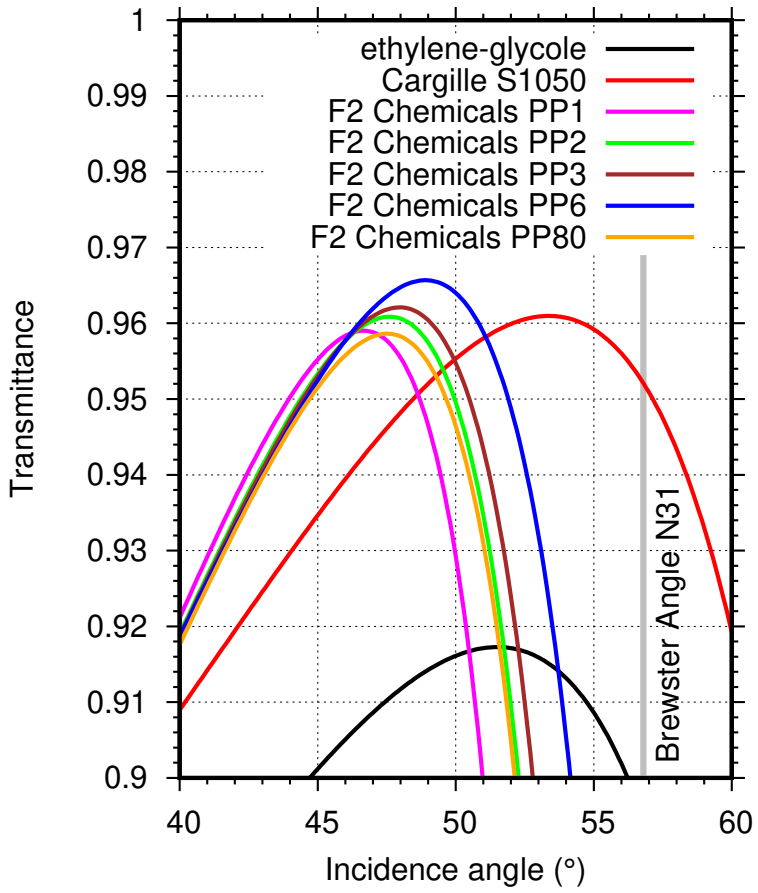

Figure 5.6: Transmittance of the amplifier for a fluid layer of $1.5\,\mathrm{mm}$ and wavelength of $1053\,\mathrm{nm}$. Transmittance calculated from (5.11) using absorption data from fig. 5.1 and refraction data from tab. 5.2. The Brewster angle of the amplifier glass with air is denoted as a grey line.

Figure 5.6 further shows a strong influence of the coolants on the transmittance, with values as high as 96.7% ± 0.1% for Flutec PP6 and as low as 95.9% ± 0.1% for Flutec PP1 at their respective maxima. Ethylene-glycol was again included as a reference and shows the dominance of the high absorption coefficent of ethylene-glycol over its high index matching compared to the other liquids with a transmittance of 91.7% ± 0.1%.
The angular dependence of the transmittance is also influenced by the matching of the refractive index of the coolant and the gain medium. Better matched liquids such as ethylene-glycole and Cargille S1050 feature flatter slopes, while less well matched fluids such as Flutec PP1 through PP80 feature steeper slopes and thus increased dependence of the transmittance on the incidence angle.
From figure 5.6 it is apparent that the absorption losses of ethylene-glycol discovered in figure 5.1 dominate the transmission behaviour of the coolant, while the lower absorption losses of Cargille S1050 seem to be mitigated by its increased refractive index matching (see tab. 5.2). These results show, that the highest transmission performance can be achieved by utilizing the higher order Flutec liquids such as PP3, PP80 and PP6 with the latter exhibiting the best transmission performance of all potential coolants. In these liquids their very low absorption mitigates the pronounced difference of their refractive indices from the amplifier glass at their respective optimum incidence angles.

5.4 Conclusion

Analysing the thermal and kinematic properties of potential coolants it was possible to rule out nitrogen as a coolant due to the necessity to operate it at high flow velocities leading to vibrations in the amplifier.
Further research into the chemical compatibility of the liquid coolants showed the gain medium to be susceptible to dissolution and crack formation by water, while the glue connecting the anti-reflection cladding to the glass was shown to be soluble in ethylene-glycol, thus preventing the use of water and ethylene-glycol as coolants.
By measuring the absorption and refraction characteristics of the coolants it was possible to calculate the optical transmission of the amplifier with the best transmittance of 96.7% being achieved by Flutec PP6.
Comparing the categories of thermal and kinematic properties, chemical compatibility and transmission performance, the liquids *Cargille S1050* and *F2 Chemicals Flutec PP6* emerged as the best coolants for the chosen amplifier setup. While S1050 offers a higher heat capacity and better index matching, PP6 features a lower viscosity, lower absorption and less restraints on the construction materials of the amplifier. The choice was finally made for F2 Chemicals PP6 due to its slightly better transmission performance and lower cost compared to Cargille S1050.

6 Simulated Prototype Operation

To estimate the performance of the prototype design in combination with the Flutec PP6 cooling liquid, a series of simulations and analysis tools were used to analyze the cooling performance as well as the resulting optical performance of the amplifier.
This was achieved using ANSYS simulations of the coolant flow and thermal transport as the basis to calculate the distribution of thermal energy in the glass discs. From these distributions the optical path of partial beams through the amplifier setup can be calculated, resulting in the wavefront profile of the total beam. By analyzing these profiles using a *zernike decomposition* tool developed at PHELIX, the deformations of the wavefront can be identified and potential optimizing solutions can be formulated.

6.1 Thermal Distributions

To simulate the cooling performance of the prototype design the simulations conducted in chapter 4.2 were extended to utilize the exact geometry of the prototype based on the design drawings. The simulations were further improved by adding the thermal properties of the coolants, the glass discs and the ambient gas.
Although the distribution of energy imparted on the glass by the flash lamps is by design mostly homogenous, parts like the light shield will limit the exposure of the discs to certain areas. This inhomogenous exposure to the pump light, thus leads to thermal gradients in the glass which have to be equilibrated for optimum optical performance. The temperature increase of the exposed glass reagions had been calculated in equation 4.2 and amounted to maximum temperature differential of $\Delta T = 1.62\,\mathrm{K}$ in the discs. The cooling of the discs therefore serves to reduce these thermal gradients as well as reducing the accumulation of thermal energy over several consecutive pump events.

6.1.1 Coolant Temperature Profile

A set of preliminary one dimensional simulations were conducted to determine the time frame in which cooling of the amplifier discs could achieve a reduction of thermal gradients to $\Delta T \leq 0.01\,\mathrm{K}$ as this was assumed to reduce the thermally induced aberrations of the beam to within acceptable limits. These simulations used a one-dimensional representation of the amplifier, including the ambient nitrogen gas and were thus mostly dominated by the thermal conduction inside the glass discs. Initially, these simulations used a static temperature of 20 °C for the nitrogen gas and the coolant, which lead to cooling durations larger than ten minutes. To reduce this cooling time and meet the goal set for this project, a temperature profile for the coolant was introduced (fig. 6.1a). The shape of the temperature profile was originally modeled as a step function but was quickly changed to a smoothstep function to simulate the behaviour of a

heating element with its finite rise-time. The goal of this profile was to provide cooling liquid at lower temperatures during the initial phase of a cooling cycle, increasing the thermal gradient between the glass and coolant, thus enabling a higher thermal flux, as described in chapter 3.2. By increasing the coolant temperature at a later stage in the cooling cycle, the temperature of the discs can be stabilized at the target temperature of 20 °C.

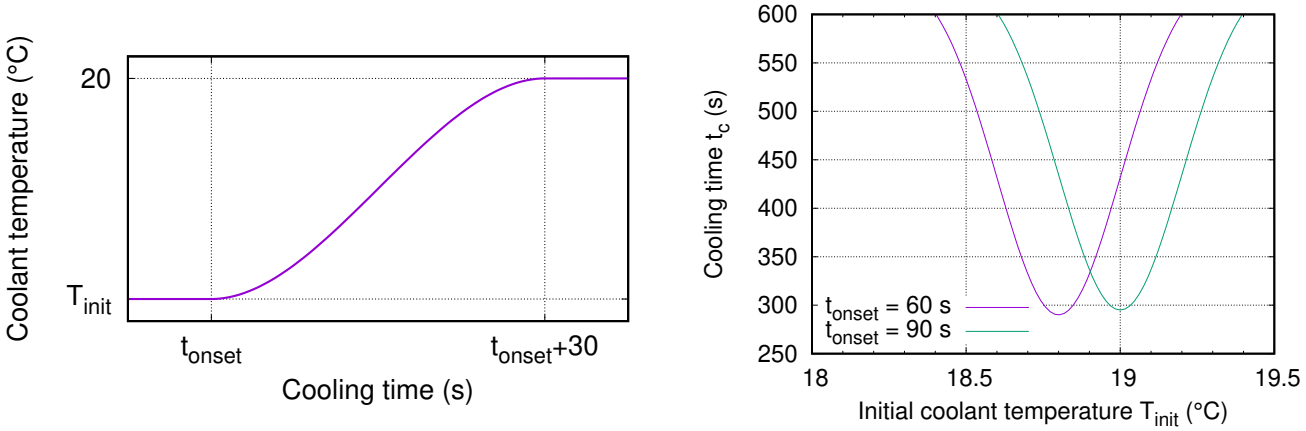

(a) Smoothstep profile of the coolant temperature, chosen to reflect the finite rise-time of thermal control elements.

(b) Dependence of the cooling time on the initial coolant temperature T_{init}

Figure 6.1: Temperature profile of the coolant and its impact on the cooling time in one-dimensional simulations of the amplifier setup.

The time, the system takes to stabilize at the target temperature (fig. 6.1b), depends on the initial coolant temperature T_{init} and the onset of the temperature increase t_{onset}. These simulations show that for certain temperature profiles cooling times of five minutes are potentially feasable. However, figure 6.1b further shows that cooling the amplifier too much, by either using colder coolant or increasing the temperature too late, the relaxation time of the system starts to increase again. This is caused by the temperature distribution in the glass starting to get dominated by the thermal gradients induced by the coolant and not the initial temperature distribution. Since the one-dimensional simulations disregarded higher dimensional effects such as tranversal thermal conduction, these temperature profiles had to be iteratively readjusted for higher-order simulations going forward.

6.1.2 Simulation of Thermal Distributions

To study the removal of thermal energy from the actual geometry of the protoype a set of simulations capable of introducing three-dimensional and transient effects such as transverse thermal conduction in the glass and gradual heating of the coolant were necessary. These simulations were conducted using the CFX module of ANSYS for simulating the fluid dynamics of the coolant as well as the thermal transport.

Setup

The simulation setup utilized the design drawings of the amplifier prototype to define the geometry of the fluid and glass volumes. By limiting the distribution of thermal energy in the glass to an elliptical region at the center of the rectangular discs it was possible to simulate the irradiation of the discs by pumplight from a single pump event passing through the aperture in the light shield. Due to a lack of authentic flash lamp spectra and to save calculation time the absorption of the thermal energy was simplified to a depth independent constant model instead of using the Beer-Lambert law (5.2).
Thermal transport calculations were limited to the fluid and glass volumes, excluding the bulk material of the amplifier frame. This approximation was chosen since the glass discs are only in contact with structural components featuring low thermal conductivity, such as the plastic spacers and the O-rings. The reduced calculation load provided by this approximation helped to reduce the simulation time to about three CPU days.
Additionally, a heat sink was added to the outer surface of the glass discs to simulate convective cooling with the ambient nitrogen gas.
The coolant flow between the discs was set up with an inlet at the bottom and an outlet at the top the flush out any bubbles forming in the cavity, as discussed in chapter 4.2
To increase the performance of the coolant a tailored temperature profile was implemented to utilize the effect discovered in the one-dimensional simulations.
Iterations on the temperature profile lead to an optimum cooling performance at an initial coolant temperature of $T_{\text{init}} = 18\,^{\circ}\text{C}$ and an onset time of $t_{\text{onset}} = 210\,\text{s}$.

Simulation Analysis

From the preliminary simulations, it was discovered that cooling times between five to ten minutes could be achieved with optimized temperature profiles. While the original project proposal had called for a repetition rate of $1/5\,\text{min}^{-1}$ it was assumed that three-dimensional effects in the discs and coolant impact the cooling time negatively. Thus, the maximum permissible cooling time for the temperature differentials of a single pulse was set to 10 minutes.
However, the ANSYS simulations quickly showed that the more or less arbitrarily set goal for the temperature differntials of $\Delta T \leq 0.01\,\text{K}$ defined in the one-dimensional simulations could not be achieved within the 10 minute time frame. Therefore, the simulations were used to analyse the effects leading to the increase in cooling time and to optimize the variable parameters, such as the coolant flux and temperature profile, to minimize the thermal gradients as much as possible within the given time frame.
One cause of the prolonged cooling time is the loss of cooling efficiency due to the gradual absorption of heat by the coolant, seen in figure 6.2a. The heat absorption leads to lower temperature differentials between the coolant and the glass regions farther from the inlet which according to (3.5) leads to a reduction of the thermal flux and thus the observed reduction in coolant efficiency. The result is a thermal gradient between the inlet region of the discs and the regions closer to the outlet seen in figure 6.2b. This effect can be countered by either increasing the flow rate of the coolant in the amplifier or replacing the coolant with liquids featuring a higher volumetric heat capacity.

To drive a higher flow rate the pressure differential between the inlet and outlet has to be increased. An increase in pressure however exerts additional force on the glass discs which can lead to deformations and damages if the pressure is to high. To avoid these effects an upper limit of 300 mbar was set for the pressure differential between inlet and the ambient nitrogen, which corresponds to the pressure at the outlet.
The option of changing the coolant was also considered, however, of the potential coolants (tab. 5.1) only water and ethylene-glycol featured a higher volumetric heat capacity than Flutec PP6 but those had to be ruled out due to their chemical incompatibility with the amplifier discs. The solution of using lower viscosity liquids to boost the flow rate was also discarded as the lower order Flutec liquids featuring lower viscosities than PP6 did not reach the required optical performance.
The second reason for the prolonged cooling time compared to the one-dimensional case can be found in the slow equilibration of thermal gradients in the transverse directions of the discs. Since this equilibration is dominated by the low thermal conductivity of the glass very little could be done to mitigate the problem. Due to the slow equilibration the shape of the initial thermal distribution in the glass can still be identified in figure 6.2b after ten minutes of cooling. To extract as much thermal energy from the discs as possible in the given time frame and thus try to even out the thermal gradients, the coolants' temperature profile had to be optimized. By using the profile for the one-dimensional case as a basis, the onset time and initial coolant temperature could be varied to optimize the reduction of thermal gradients after a ten minute cooling phase. The optimal parameter set found for simulations using PP6 as the coolant at an inlet-outlet pressure differential of 300 mbar was an initial coolant temperature of $T_{\text{init}} = 18\,°\text{C}$ for an onset time of $t_{\text{onset}} = 210\,\text{s}$.

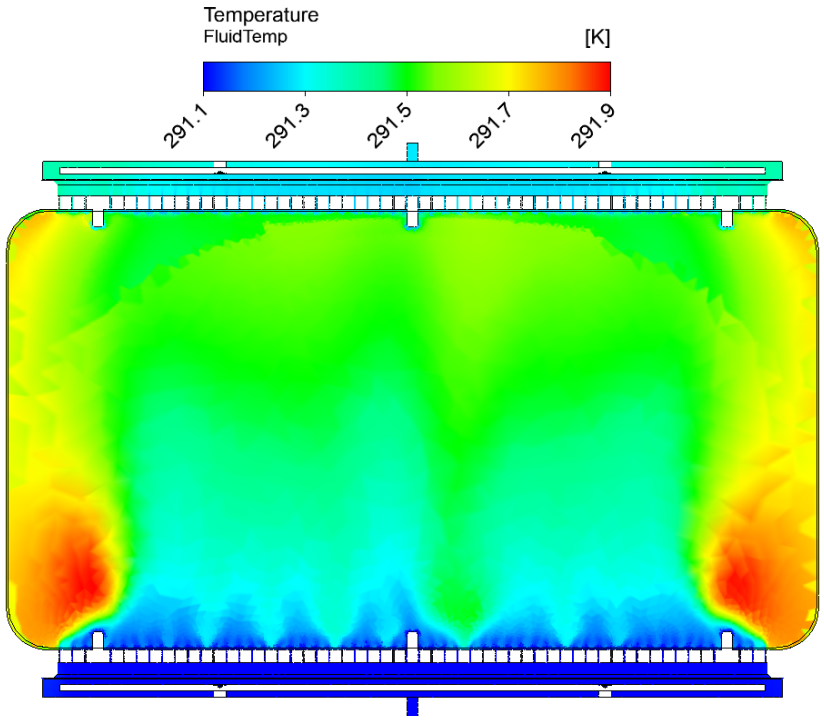

(a) Temperature map of the coolant 60 seconds after the pulse, showing the gradual heating of the cooling liquid during its traverse from the bottom of the amplifier to the top. Also shown are volumes of heated coolant trapped at the edges of the amplifier due to the formation of small vortices (fig. 4.3b).

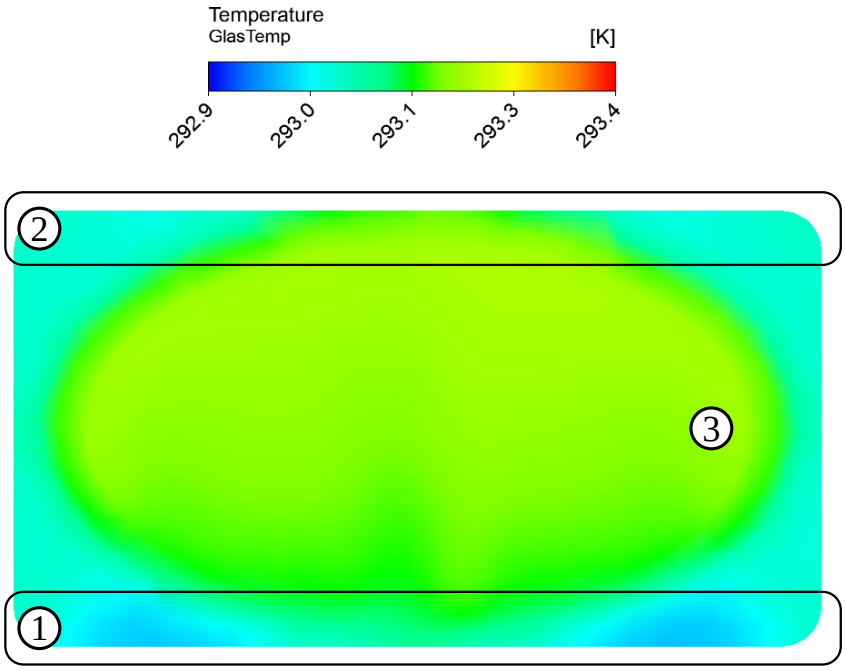

(b) Temperature distribution at the center of the glass disc after a single 10 minute cooling phase. Points of interest are the inlet ① and outlet ② regions as well as the remnant of the original temperature distribution ③.

Figure 6.2: Temperature maps of the coolant and the glass, showing the gradual heating of the coolant and its effect on the cooling process of the amplifier discs.

After optimizing the free parameters for a single cooling phase of ten minutes, the simulations were extended to research the effects of multiple consecutive pump events on the temperature distribution in the glass. These simulations served as a more accurate representation of the actual operation of a repeating laser amplifier and could be used to identify the effects of residual thermal energy on successive cooling cycles.
The simulations for repeated pulses used the same basic setup as the single cooling phase simulations but implemented a periodic increase of the thermal energy in the aperture region every five minutes to simulate the targeted repetition rate of $^1/_5\,\mathrm{min}^{-1}$. The optimized temperature profile of the coolant found in the previous simulations was implemented and repeated for each cycle. The total simulation time was also increased to cover the thermal evolution of the system over ten consecutive cooling cycles.

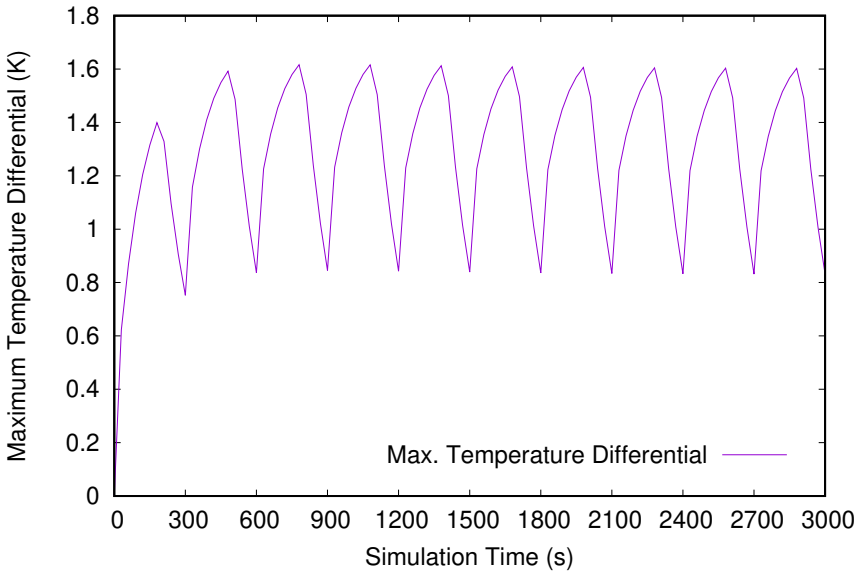

Figure 6.3: Evolution of the maximum temperature differentials observed in the glass discs over consecutive cooling cycles. Pump event occurs every 300 seconds.

With the goal to minimize the thermal gradients in the glass discs, analysis of the evolution of the thermal gradients over successive pump and cooling cycles is necessary. Figure 6.3 shows this evolution of the maximum thermal gradient present in the discs during the simulation.
During a cooling cycle the thermal gradient first increases as glass in closer proximity to the coolant is cooled much quicker than glass regions further from the coolant layer due to the low thermal conductivity of the glass. The gradients decrease once the coolant is switched from its initial temperature to the operating temperature of the amplifier. However, the short cooling time of 300 seconds does not allow the gradients to be extracted completely and successive pump events lead to an accumulation of thermal energy in the glass discs. Figure 6.3 shows that this accumulation lasts for the first two to three cooling cycles until the increase in thermal gradients levels out. This is caused by the increased temperature differential between the heated glass regions and the coolant, thus increasing the thermal flux in these areas. This increase in thermal flux leads to a balance between the heat accumulation in the discs and the cooling

provided by the increased temperature differential. The result is the formation of a steady state for the final thermal distribution in the glass over consecutive pulses.

6.2 Optical Path and Wavefront

Chapter 3.3 has shown how these residual thermal distributions cause changes to the optical behaviour of the amplifier material and ultimately distort the transmitted wavefront. To identify the detrimental effect of the thermal distributions predicted by the simulations, it is necessary to calculate the optical path of a set of rays. From this set of optical paths an analysis of the incurred wavefront aberrations can be conducted.

6.2.1 Optical Path Distortion

To apply the calculation of the optical path distortion (chp. 3.4.1) to the simulated thermal distributions in chapter 6.1.2 a custom post-processing script was necessary as the available ANSYS modules did not offer this feature. The script combined a ray tracing algorithm with an n-Simplex interpolation [Hemingway, 2002] to calculate the optical path of a set of rays which were generated in a rectangular grid with a set grid size of 56 x 32 cm and a resolution of 5 mm to simulate the behaviour of a plane wave.
This rectangular shape allowed for the investigation of the optical path in the disc regions relevant to both the PHELIX setup with its large elliptical beam projection as well as the 100 J diagnostic laser with its rectangular setup of four beams.
The incidence angle of the rays was further set to mimic the experimental setups at $\theta_i = 48°$.
Evaluation of the optical path of each ray commenced in steps of 5 mm from the surface of the discs, using Snell's law to account for refraction of the rays at the ambient-glass and glass-fluid interfaces.
The optical path length of each step was calculated using a discrete application of (3.15). The interpolation algorythm was used to calculate the local temperature of the glass from the ANSYS data at the sampling points of each ray. From these local temperatures the local refractive index and thermal expansion of the glass could be derived to be used in (3.15). Since detailed information on the indicatrix of the glass was not available, stress calculation and thus birefringence effects of the refractive index had to be omitted (see chp. 3.3). By iteratively calculating the optical path length of each ray, as it passes through the amplifier discs, a map of the optical path differences could be created.

6.2.2 Wavefront Analysis

To understand the effects of these optical path differences on the propagation of a beam through the amplifier, it is necessary to derive the resulting wavefront. By sampling the original beam as a set of rays and assuming the use of a monochromatic beam with a planar wavefront as an input beam (see chp. 3.4.2), the optical path differences calculated by the ray-tracing algorithm can be directly translated into localized phase shifts of the wavefront using equation (3.20).
The resulting shape of the wavefronts directly after a single pump event followed by ten minutes of cooling are depicted in figure 6.4. By comparing the wavefront at the beginning of the

cooling cycle to the ideal case of a plane wavefront the impact of the thermal distributions in the glass and the necessity of cooling becomes apparent. This is caused by a shift of the central beam region in the positive phase direction compared to the periphery of the beam. The shift shows an increase of the optical path which can be attributed to the dominance of the positive linear thermal expansion coefficient $\alpha = 115 \times 10^{-7}\,\mathrm{K}^{-1}$ over the negative linear thermo-optic coefficient $dn/dT = -43 \times 10^{-7}\,\mathrm{K}^{-1}$ of the glass [Hu et al., 2014].
By comparing the wavefront of the uncooled amplifier to a ten minute simulation of the legacy setup using passive convective cooling with an ambient nitrogen volume (fig. 6.4b), it is apparent that the low thermal conductivity of the glass paired with the low heat capacity of the ambient nitrogen leads to an insufficient extraction of the thermal gradients in the discs. The result is only a marginal reduction in the deformations of the wavefront after ten minutes of cooling.
The simulated wavefront of the prototype setup (fig. 6.4c) shows a clear improvement to the wavefront distortions over the legacy setup and the uncooled case by significantly reducing the wavefront deformations.

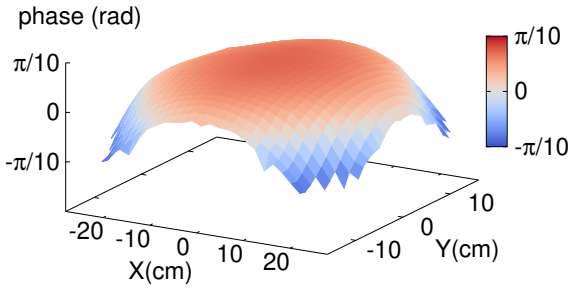

(a) Wavefront evaluated directly after a single pump event.

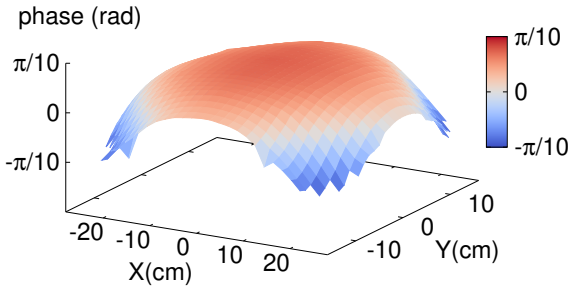

(b) Wavefront after ten minutes of passive cooling in the legacy setup of PHELIX using only the ambient nitrogen gas.

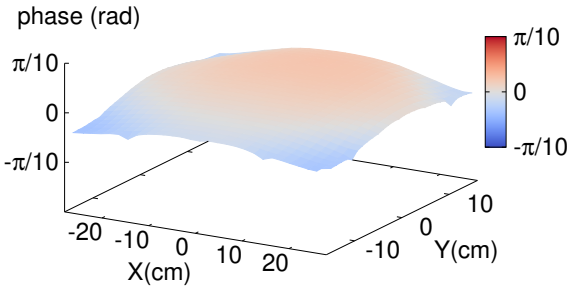

(c) Wavefront after ten minutes of active cooling using the prototype setup.

Figure 6.4: Wavefronts derived from the simulated temperature distributions of a single ten minute cooling phase showing the difference between passive and active cooling on the wavefront evolution.

By increasing the repetition rate to $1/5\,\mathrm{min}^{-1}$, it was shown previously that the maximum thermal gradients in the glass at the end of each cooling cycle approach a steady state (fig. 6.3). Comparing the changes of the wavefront occuring between the end of the first and third cooling cycle (fig. 6.5a), the previously observed increase of thermal gradients over these cycles is shown to impact the evolution of the wavefront quite significantly. However, comparing the wavefront at the end of the third and fifth cycle (fig. 6.5b), a significant decrease in the variations between the two can be seen. The variations between cycles further decrease between the fifth and the tenth cycle (fig. 6.5c) supporting the hypothesis of the formation of a steady state by operating the amplifier prototype at a repetition rate of $1/5\,\mathrm{min}^{-1}$.
While it would be ideal if the temperature differentials in the glass discs could be reduced to an isotropic distribution, the development of a steady state for the wavefront in combination with adaptive optics would enable the operation of the design at the targeted repetition rate without requiring a complete extraction of all thermal gradients from the discs as long as the cycle of pump events is not interrupted.

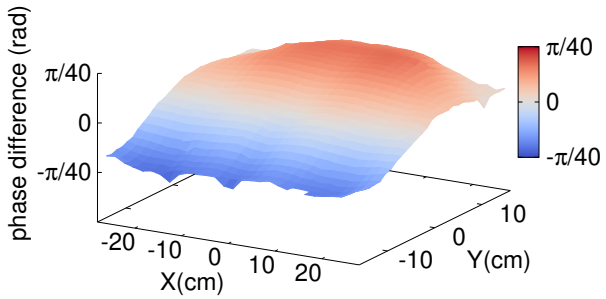

(a) Phase difference profile between the end of the first and third cooling cycle.

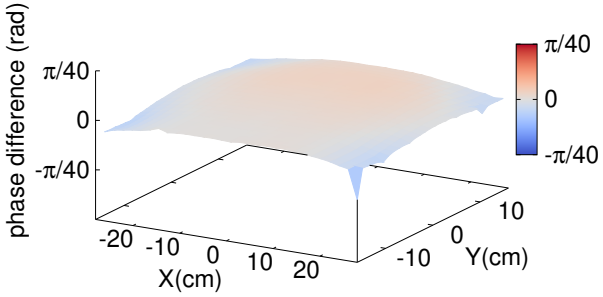

(b) Phase difference profile between the end of the third and fifth cooling cycle.

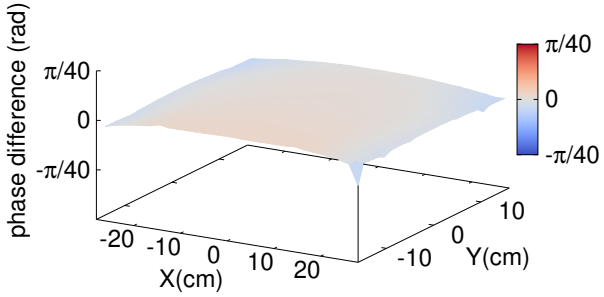

(c) Phase difference profile between the end of the fifth and tenth cooling cycle.

Figure 6.5: Difference profiles between the phase shifts at the end of various cooling cycles during a $1/5\,\mathrm{min}^{-1}$ repetition rate simulation, showing the development of a steady state previously observed in figure 6.3.

To optimize the wavefront transmitted by the amplifier mitigation techniques for the deformations have to the formulated. This requires the quantitative analysis of the aberrations via a *zernike decomposition* of the wavefront. The analysis was conducted using software developed at PHELIX to analyse the phase shift data from the ANSYS and raytracing simulations. By decomposing the wavefront profile into its constituent Zernike polynomials using the $|R_n^m(1)| = 1$ scaling (see chp. 3.4.3), the analysis tool can be used to determine the amplitude of each aberration which can further be used to identify the causes of the aberrations observed in the wavefront.

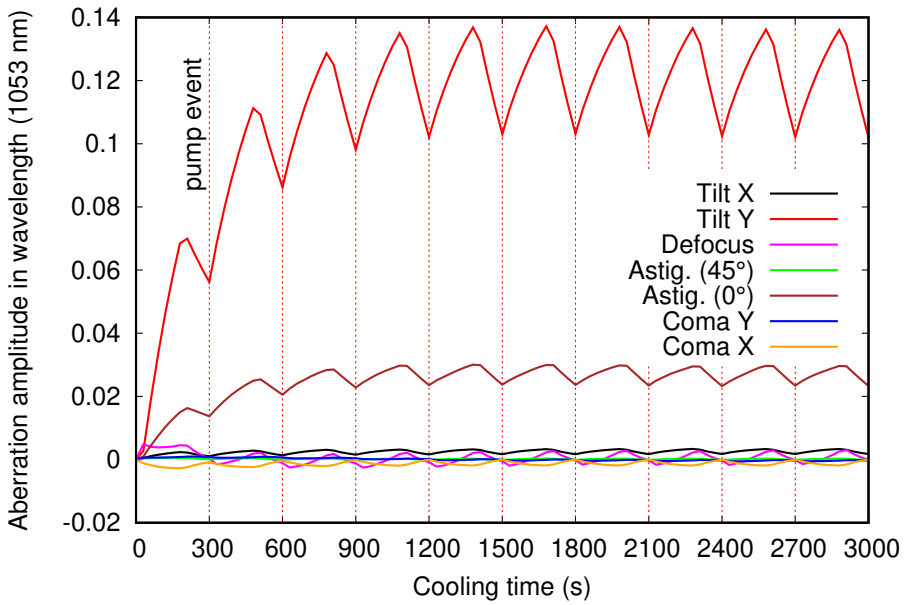

Figure 6.6: Evolution of Zernike aberrations caused by simulated thermal distributions in repeatedly pumped glass discs with pump events every 300 s.

Figure 6.6 shows the evolution of the most prominent Zernike aberrations present in the wavefronts of a simulation at a repetition rate of $1/5\,\mathrm{min}^{-1}$.
The results exhibit the same steady state behaviour over multiple cooling cycles as observed before but the Zernike decomposition further allows the identification of the two dominant aberrations as a tilt in Y-direction and a 0 degree astigmatism.
The occurence of the Y-tilt can be traced to the vertical temperature differential between the lower and upper regions of the glass discs caused by the gradual heating of the coolant already discovered in figure 6.2b. A reduction of the aberration would be possible by either increasing the pressure differential between inlet and outlet, thus increasing the flow rate of the coolant or discovering a suitable coolant featuring a better combination of volumetric heat capacity and viscosity compared to Flutec PP6.
The second most dominant aberration is the 0 degree astigmatism which features a more complex three-dimensional geometry (fig. 3.4) and whose origin can be traced to the elliptical initial thermal distribution in the glass. Due to the elliptical shape of the distribution, coolant passing over the left and right sides of the discs passes heated areas over shorter distances compared to coolant passing over the center line of the discs as shown in figure 6.7.

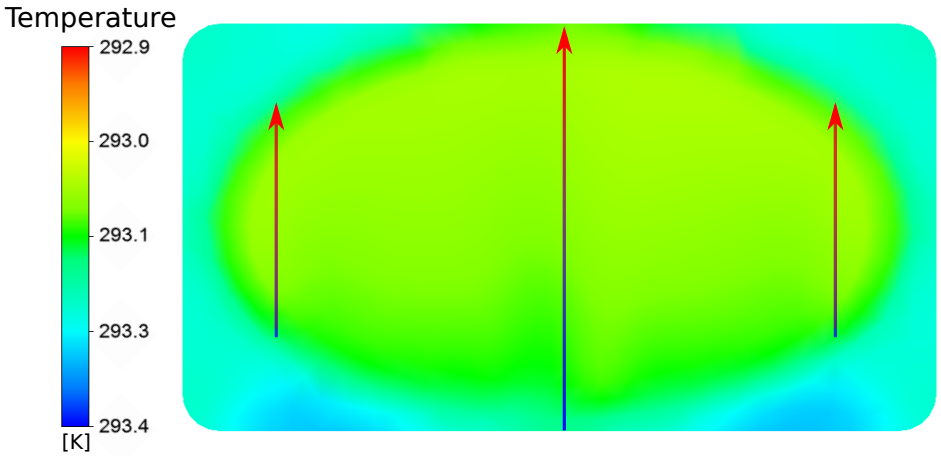

Figure 6.7: Comparison of the different exposure paths of the coolant to the heated glass in the central and side regions of the elliptical thermal distribution.

This difference in coolant heating causes an uneven extraction of heat between the central and the side regions of the heat distribution. The result is a lower temperature at the side regions of the discs at the end of each cooling cycle leading to a difference in the optical paths in these regions and the resulting astigmatism observed in the wavefront profiles.

A way to mitigate this aberration would be an increase in either flow rate or volumetric heat capacity of the coolant to even out the differences between the side and central regions during the cooling phase.

7 Prototype Testing

To validate the simulation results of chapter 6 as well as testing the mechanical viability of the prototype, a test bench was constructed at PHELIX. Testing in the scope of this thesis was limited to the coolant seal tightness and the impact of static deformations of the glass discs on the transmitted wavefront.
As a measure to avoid damages to the expensive amplifier glass discs, a pair of optical grade dummy discs was procured from *Bond Optics* and used in all tests of the amplifier. These discs were made off *Ohara S-BSL7* [OHARA, 2017] glass featuring a slightly lower refractive index than the phosphate glass by SIOM at 1.51 instead of 1.53 and featured no doping.

7.1 Coolant Seal Tightness

One concern surrounding the operation of a liquid cooled amplifier during the concept phase was the potential of coolant leaking from the module and causing damage to equipment in the vicinity, especially electrical components such as the flash lamps. To prevent damage to such components, the first test conducted on the amplifier module tested the tightness of the coolant seals, especially the sealing scheme necessary to reduce bending of the glass discs (see fig. 4.7). For the test, the amplifier was assembled with the dummy discs and positioned upright in a basin to avoid spilling of leaked coolant (fig. 7.1).

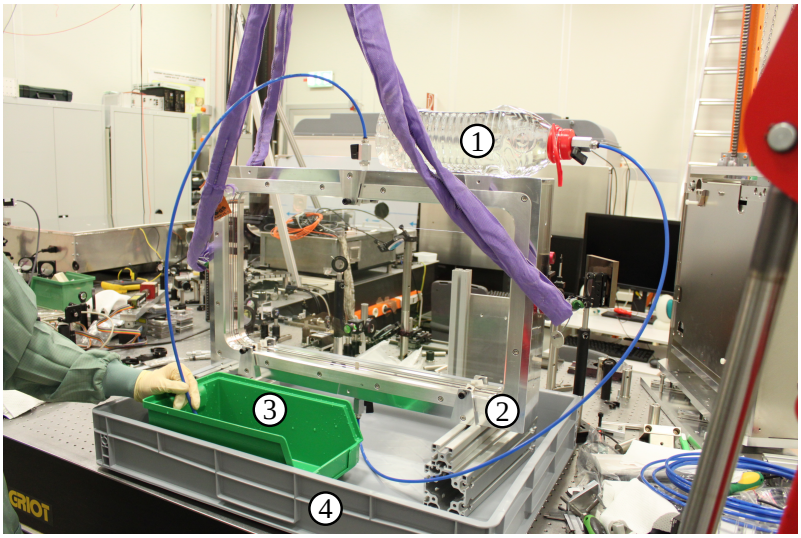

Figure 7.1: Setup for testing the seal tightness, with the water supply reservoir ① elevated above the prototype ② for the hydrostatic feeding of water. Further shown are the drainage tank ③ below the prototype module and the spill basin ④.

Due to the use of the dummy glass discs it was possible to use destilled water for these tests as the risk of chemical damages to the dummy glass was deemed acceptable, contrary to the

amplifier glass which was considered too expensive to take this risk. The choice of replacing Flutec PP6 with water dramatically reduced the cost of these tests and enabled a quicker access to the required amount of liquid.
During the assembley of the prototype it was found that the red colored O-ring for sealing the glass discs was only visible when in direct contact with the dummy discs due to total internal reflection in the glass. This effect was used to confirm that the O-rings were in full contact with the glass discs after tightening the screws on the piston frame (fig. 7.2) by checking the visibility of the O-rings around the circumference of the discs.

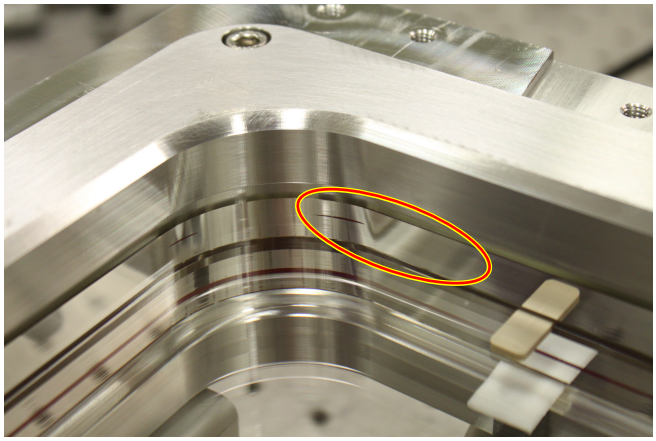

(a) Prototype with uncompressed O-ring seal. The O-ring is only visible in small areas where the bending of the O-ring pushes it against the glass.

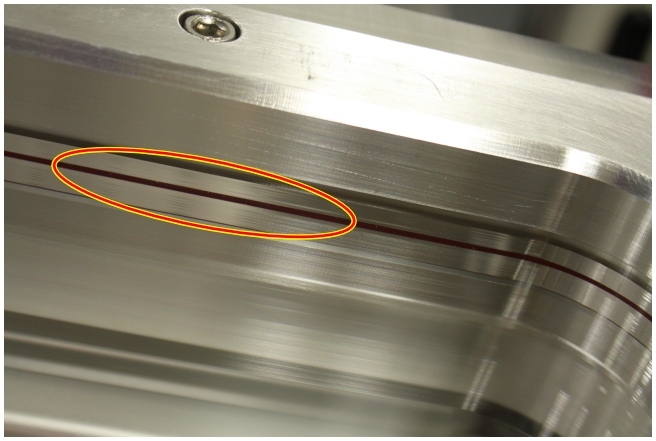

(b) After tightening of the piston frame screws the O-ring is compressed and contact between the ring and the glass discs is achieved over the entire circumference of the disc.

Figure 7.2: Different compression states of the red O-ring seal around the glass discs during assembly. Visibility of the O-ring is used as indication for contact between the seal and the glass.

To test the tightness of the seal a water supply and a drain reservoir were attached to the bottom and top of the module respectively.
Filling the amplifier prototype with water showed that the seals held tight and no leakage was discovered during the process. However, after several assemblies and disassemblies of the amplifier it was found that some leakage could occure due to an inhomogenous compression of the O-ring. The source of this inhomogeneity could be traced to a region of increased stiffness of the O-ring material. It was found that the O-ring was made from a rubber cord whose ends had been connected with the connection point proving to be the cause of the stiffness. To counter the resulting decreased compressibility, the connection point was placed close to one of the mounting screws of the piston frame and torgue applied to this screw was increased compared to the remaining screws. This evened out the compression of the O-ring, thus assuring the tightness of the coolant seal.

7.2 Wavefront Measurements

After ensuring the tightness of the coolant seals, the prototype with the dummy glass discs was placed into the optical test bench to measure the transmitted wavefront. Early optical tests used no coolant to identify effects caused soley by the glass, while later tests used water as a substitude for PP6 to conduct the initial tests of the wavefront behaviour. Due to the good match between the refractive indices of water and PP6 at 1053 nm, this substitution reduced the cost of procurement as well as the complexity of the setup as no recycling system for the coolant had to be implemented at this stage.
The test bench was upgraded with an additional optical setup, shown in figure 7.3a, which enabled the detection of the transmitted wavefront of a double-pass through the prototype via a probe beam provided by a contiuous wave (cw) diode laser at 1053 nm. Further additions included a tent structure around the test bench to reduce the impact of air turbulences on the propagation of the beam. By using a diffusing lense and an off-axis mounted parabolic mirror it was possible to increase the beam diameter of the probe beam to about 20 cm, filling parts of the aperture of the prototype discs (fig. 7.3a). The setup futher featured a zero degree mirror after the prototype module to double-pass the discs and direct the beam back down the beam path (fig. 7.3b) to a beam splitter. The beam splitter was used to decouple the return beam to the Shack-Hartmann-Sensor for analysis of the returning wavefront.
During this thesis, the setup had not yet been optimized and only qualitative measurements of the wavefront could be conducted. The reason was an insufficiently optimized relay imaging of the wavefront from the amplifier to the wavefront sensor. This faulty relay imaging resulted in large shifts of the beam in the sensor's near-field caused by wavefront tilts in the amplifier. The large shifts of the beam required constant readjustment of the system to realign the beam with the wavefront sensor and made reproducibility impossible. These effects were further compounded by large fluctuations in the wavefront caused by motion of the air which could not be entirely suppressed by the tent.
Measurements on a dry amplifier were dominated by these fluctuations, while the observed wavefront in a water filled amplifier showed a prominent line focus feature which dominated the air induced fluctuations. The line focus could also be directly observed in the returning beam as the beam shape had been visibly distorted into a horizontal line.
An explanation for this horizontal line focus was hypothesized to be the deformations of the glass discs under the hydrostatic pressure of the coolant inside the coolant cavity. Since the retainer elements only supported the upper and lower ends of the discs the resulting bulge would feature a cylindrical shape resulting in the line focus.
To test this hypothesis a negative pressure was applied to the outlet end of the amplifier by closing the inlet valve on a toped up coolant cavity and opening the outlet valve leading to the drainage reservoir at lower elevation. Due to the outlet of the amplifier being on the top of the module this did not drain any coolant from the coolant cavity. A qualitative analysis of the transmitted wavefront during the pressure reduction first showed a reduction of the horizontal line feature, with a vertical line feature emerging as the pressure between the discs dropped further.

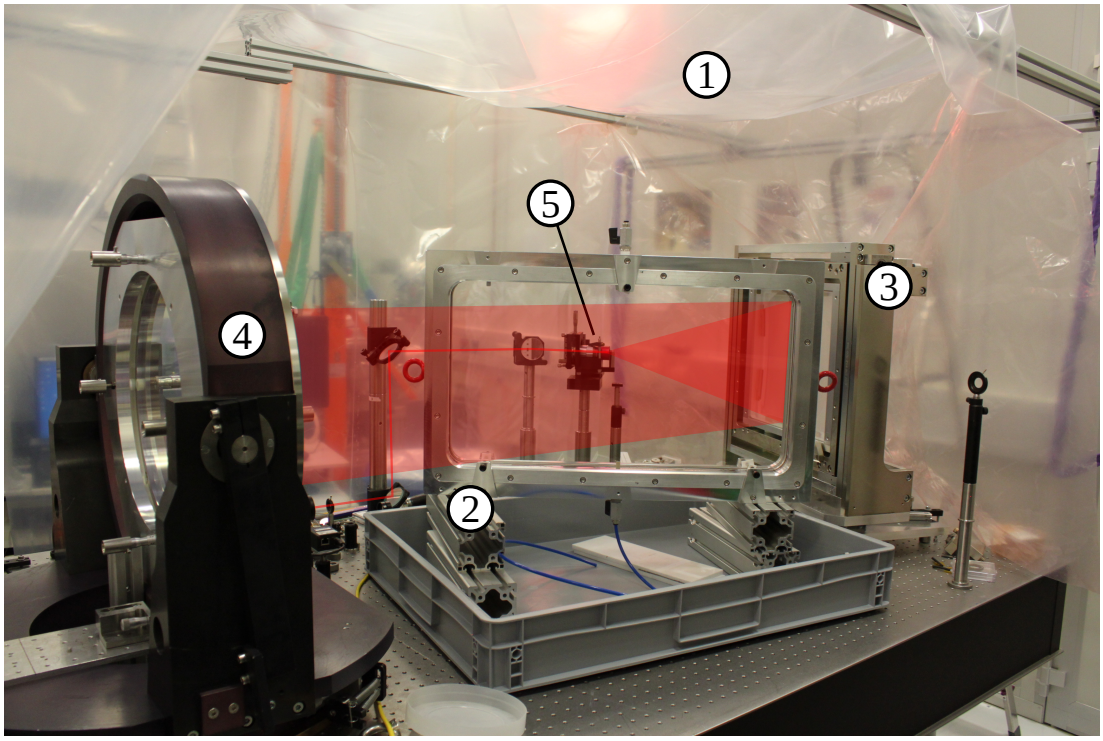

(a) Overview of the test bench setup consisting of the tent structure ①, the prototype module in a spill basin ②, a parabolic mirror ③, a zero degree mirror ④ and a diffusing lense ⑤ with the beam path shown in red.

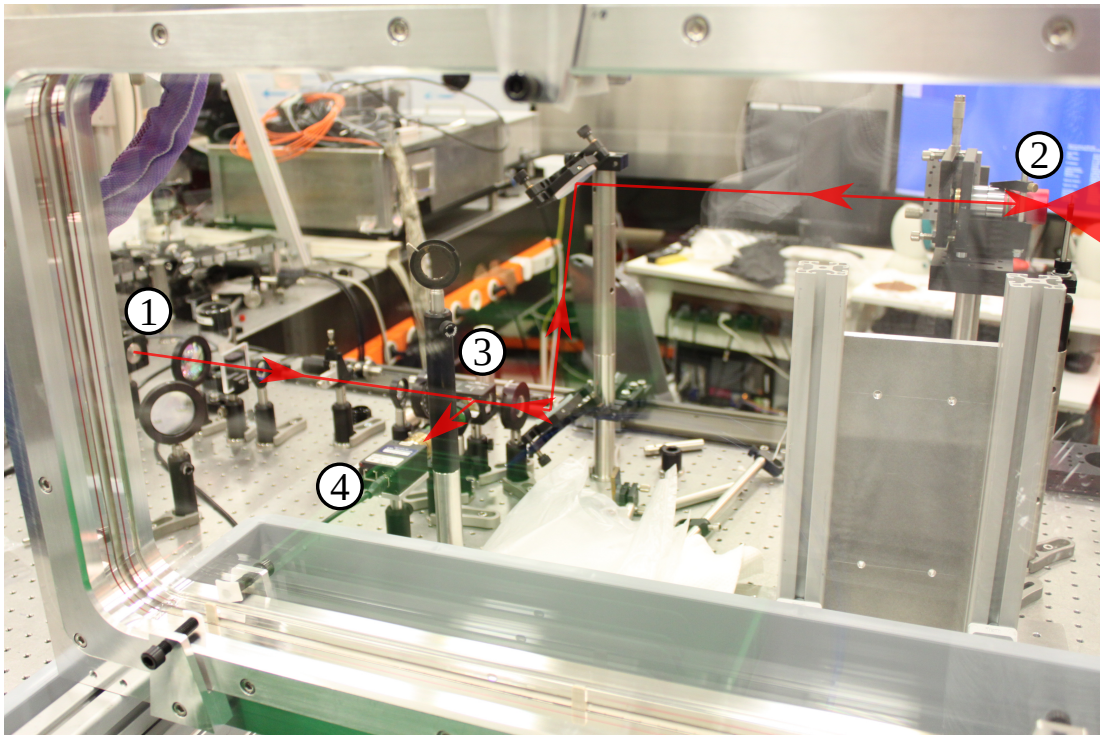

(b) Optics setup for the wavefront analysis with the incident beam ① from the laser source, the diffusing lense ② towards the parabolic mirror, a beam splitter setup for the returning beam ③ and a Shack-Hartmann-Sensor ④ for the detection of the wavefront.

Figure 7.3: Test bench setup showing the general setup with the prototype and the optical setup for the wavefront analysis.

7.3 Simulated Disc Deformation

To gain a better understanding of the glass deformations by the hydrostatic pressure between the discs and to find ways to mitigate these deformations, a series of simulations was conducted. In these simulations ANSYS was used to investigate the topology of the deformations caused by the hydrostatic pressure as well as the application of positive ambient pressure to the coolant. Further simulations were used to explore the impact of new retainer element configurations to mitigate the deformation effects for future iterations of the amplifier prototype.

The setup used in these simulations consisted of the discs, the retainer elements and their corresponding spacers, with the latter two implemented as static support points.
The simulation of the current retainer setup (fig. 7.5a) under the hydrostatic pressure of the coolant yielded a deformation of several micrometers at the center of the discs. The topology of the deformation shown in figure 7.4a exhibits a linear horizontal bulge at the center of the discs. This horizontal bulge results in the formation of a cylindrical lense by the coolant and a subsequent line focus in the transmitted wavefront which matches with the observations at the testbench.
By using Pascal's law [Meschede et al., 2015] to describe the hydrostatic pressure between the discs as

$$p(h) = \rho g h + p_0, \tag{7.1}$$

with the pressure p at depth h depending on the density ρ of the liquid and the gravitational acceleration g, it is apparent that the application of an ambient pressure p_0 at the surface of the coolant can be used to modify the pressure exerted on the discs. By applying a negative ambient pressure, as was done during the prototype tests, it is possible to counter the hydrostatic pressure at a specified depth leading to a net negative pressure above and a net positive pressure below this depth.
A simulation of this setup with a balance between hydrostatic and ambient pressure at the center of the discs can be seen in figure 7.4b showing a reduction of peak deformation by an order of magnitude compared to figure 7.4a. However, the formation of a low and a high pressure region between the discs leads to a S-shape deformation which is further compounded by indentations caused by the retainer elements.
Decreasing the ambient pressure further leads to the formation of two vertial indentations left and right of the central retainer elements seen in figure 7.4c. These indentations cause the formation of a vertically oriented cylindrical lense resulting in the vertical line focus which was also observed during the prototype tests.
To optimize the retainer configurations a set of new retainer setups was introduced in the simulations. These retainer configurations shown in figure 7.5 display the gradual progression from point support structures in figure 7.5a and 7.5b to linear support structures. While additional point support structures are easier to implement in the current prototype design the advantage of linear suport structures is their support of much larger areas of the discs compared to point support.
For each retainer configuration two simulations were conducted, one using only hydrostatic pressure as the source of the deformation and a second featuring the additional application of ambient air pressure to reduce the peak deformation.

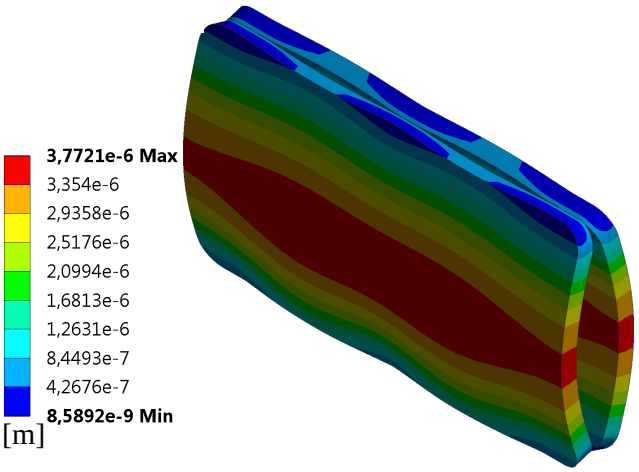

(a) Deformation of the discs under hydrostatic pressure.

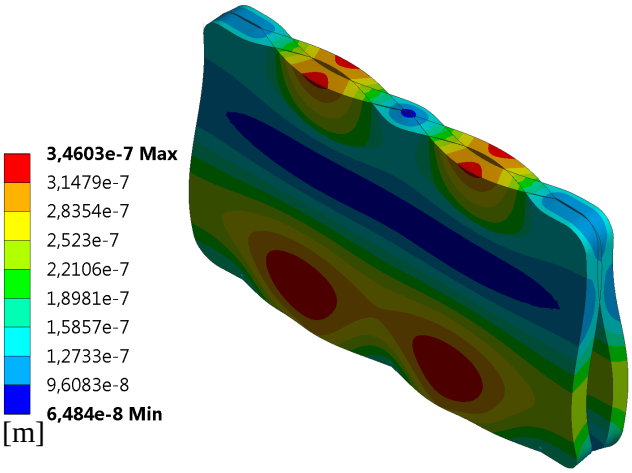

(b) Deformation of the discs under hydrostatic and ambient air pressure. The air pressure outside the discs was adjusted to compensate the hydrostatic pressure at the center of the discs.

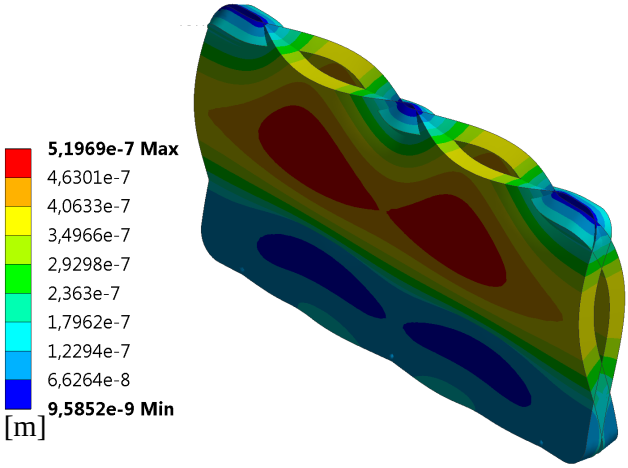

(c) Deformation of the discs under hydrostatic and ambient air pressure. The air pressure outside the discs was adjusted to compensate the hydrostatic pressure at the bottom third of the discs.

Figure 7.4: Simulated deformations of the glass discs under pressure from the coolant and ambient atmosphere using the retainer configuration of the prototype (fig. 7.5a).

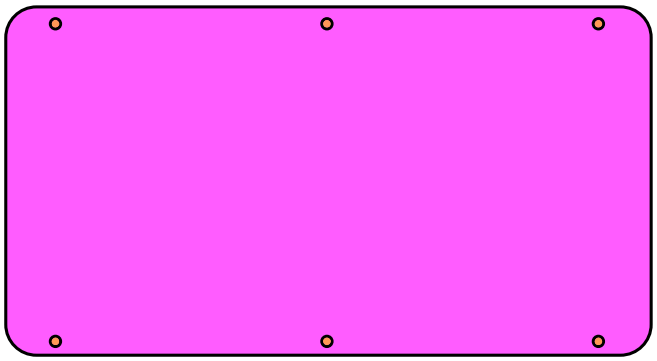

(a) Retainer setup of the current prototype, featuring six plastic screws as support points.

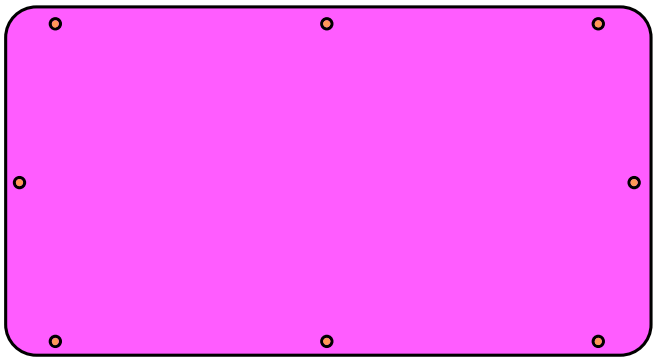

(b) Retainer setup with two additional retainer screws to support the discs.

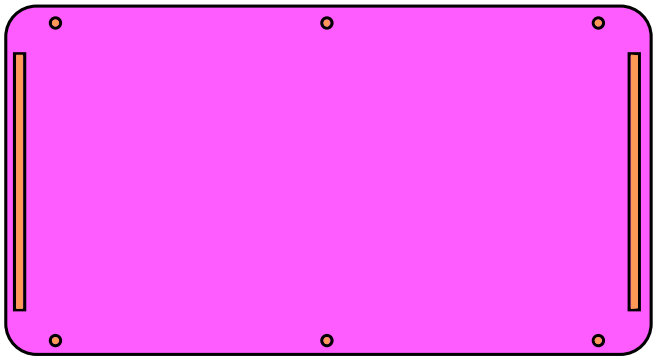

(c) Retainer setup with two additional bars at the sides to broaden the support area.

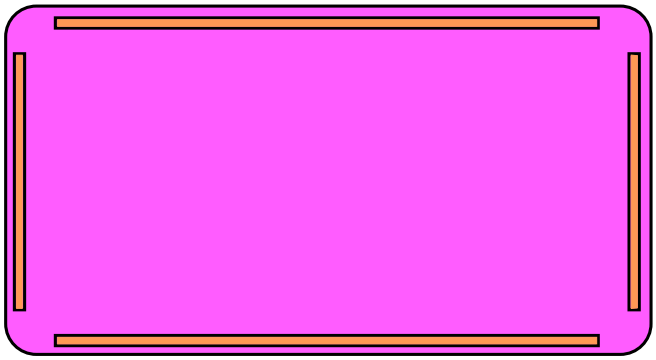

(d) Retainer setup also replacing the original screws with bars.

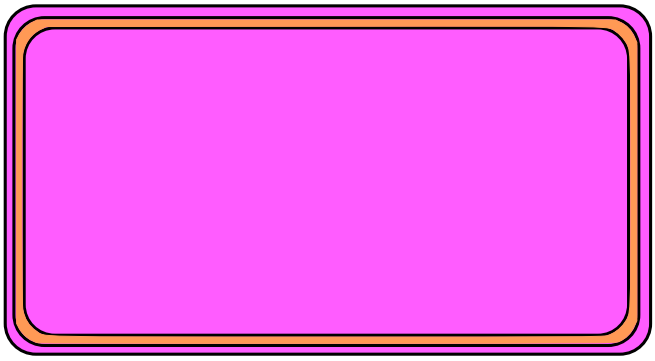

(e) Retainer setup featuring a single bar-frame to maximize the supported area.

Figure 7.5: Retainer setups investigated to understand and improve the disc deformation due to hydrostatic pressure.

By simulating the introduction of additional retainer elements to counter the deformation at the sides of the discs (fig. 7.5b), a change to the geometry of the deformation from a cylindrical lense to a spherical lense (fig. 7.6a) can be observed. While the shape of a spherical lense is not further changed by any of the other retainer configurations (fig. 7.5c - 7.5e), the magnitude of the deformation can be reduced to about one micrometer, a third of the deformation simulated for the current prototype configuration, by using a continuous retainer frame (fig. 7.6b).
Applying negative ambient pressure to the other configurations leads to a further decrease in the magnitude of the deformations with the final setup of a continuous support frame (fig. 7.5e) featuring deformations below one hundred nanometers (fig. 7.6c).
However, utilizing the ambient pressure scheme results in the development of S-shaped deformations of the discs independent of the retainer layout which are similar to those observed in figure 7.4b due to low and high pressure regions in the coolant.
To quantify the wavefront aberrations induced by the dics shapes and to enable comparisons to future prototype tests, the ability to export the deformed disc geometries as optical elements to ZEMAX OpticStudio was demonstrated. However, simulation and analysis of the resulting transmitted wavefronts has yet to be conduct.

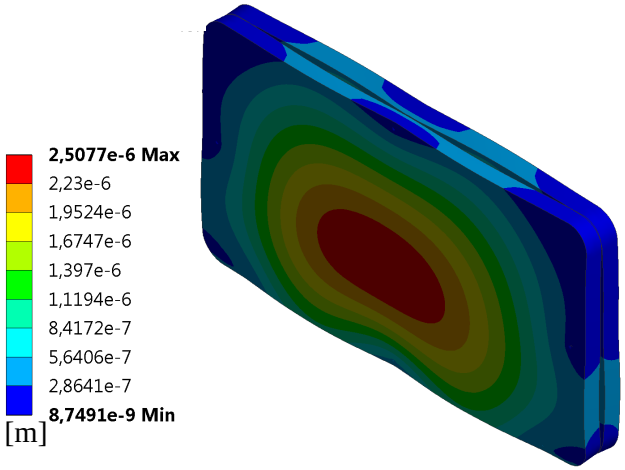

(a) Simulation of the hydrostatic deformation of the retainer setup in fig. 7.5b.

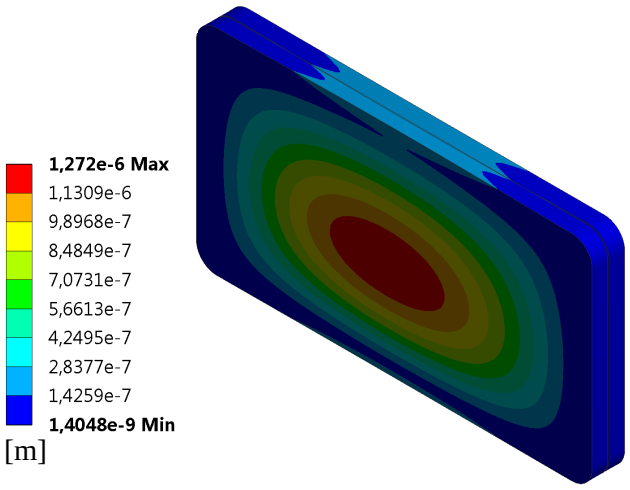

(b) Simulation of the hydrostatic deformation of the retainer setup in fig. 7.5e.

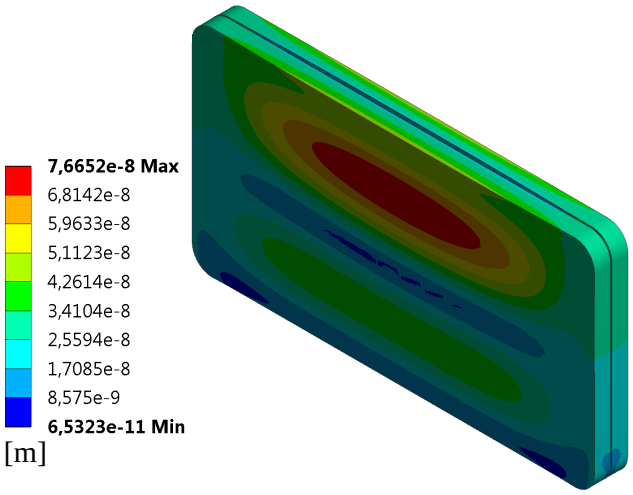

(c) Simulation of the combined hydrostatic and positive air pressure deformation of the single frame retainer setup (fig. 7.5e).

Figure 7.6: Simulated deformations of the glass discs showing the reduction of deformation magnitude by using modified retainer geometries.

8 Summary and Conclusion

The goal of this thesis was the development of a large aperture actively cooled laser amplifier prototype to increase the repetition rate of high energy, high power lasers. The targeted repetition rate of $^1/_5\,\mathrm{min}^{-1}$ of the prototype was chosen to meet the requirements of the planned Helmholtz beamline and the 100 J diagnostic laser at FAIR in addition to serving as a potential upgrade of the PHELIX facility.
The performed investigations mainly focused on overcoming the limiting factors for the repetition rate of such a system. Additionally, a combination of simulations and tests on a full scale prototype module were used to validate and optimize the cooling procedure.

The repetition rate of laser amplifiers is mostly limited by their ability to provide constant focus quality over multiple pulses. This ability is negatively impacted by anisotropic thermal distributions in the gain medium caused by the pumping process which have to be removed or equilibrated between consecutive pulses to regain the focus quality of the system. By assuming a targeted gain factor of 1.5 for the amplifier as a reference, equation (4.2) was used to calculated the thermal gradients expected in the discs, which could reach 1.61 K in the regions exposed to the optical pump.

In this project a split disc amplifier was designed to reduce these thermal gradients in a large aperture glass based amplifier. The developed design features two neodymium doped phosphate glass discs surrounding a cavity filled with a liquid coolant to extract the thermal energy deposited by the pump process via forced convective cooling. To facilitate a homogenous extraction of thermal energy a nozzle design was concieved that enabled a homogenous coolant flux over large parts of the discs by minimizing the size and occurence of vortices. The prototype further featured a modular design to optimize and easily replace various parts to allow the adaption to potential problems discovered during the experimental phase.

The geometry of the chosen split discs design requires the coolant to feature high transmission qualities in addition to its thermal and chemical requirements to enable the optimal performance of the prototype. By comparing the thermal and kinematic properties of the coolants, it was necessary to exclude gasseous coolants for our application as their propensity for turbulence formation in the setup and the resulting vibrations were deemed detrimental to the design.
Research in publications and experimental tests at the *Shanghai Institute of Optics and Fine Mechanics* further showed chemical incompatibilities of several liquids with the amplifier glass and cladding glue ([Li et al., 2018], [Suratwala et al., 2000]).
To compare the optical performance of the coolants, their respective absorption spectra and refractive indices were measured at the *Eduard-Zintl-Institut für Anorganische Chemie und Physikalische Chemie* at the Technische Universität Darmstadt and at GSI. These measurements allowed the calculation of the transmissivity of the amplifier setup at the wavelength of the laser using Fresnel's equations and the Beer-Lambert law. From these calculations the *S1050* liquid by

Cargille with a corresponding transmissivity of 96.2% and the *Flutec PP6* by *F2 Chemicals* featuring a transmissivity of 96.7% emerged as the best coolants investigated for optical transmission. PP6 was then chosen as the final coolant due to its increased optical and thermal performance over S1050 coupled with its lower procurement cost.

Simulations with the software *CADFEM Ansys* were used to investigate and optimize the cooling process using a tailored temperature profile for the coolant. The temperature distributions in the glass resulting from these simulations were further processed by a ray tracing script and zernike decompositions of the wavefronts to calculate the behaviour of the wavefront in the amplifier over consecutive pulses. By analyzing the wavefronts, the impact of various geometric features of the design as well as the development of a steady state for the wavefront aberrations after three to five pulses at the targeted repetition rate of $1/5\,\mathrm{min}^{-1}$ could be revealed.

To validate the simulations of the design experimentally, a full scale prototype was manufactured by the company *VA-Tec* and set up in a test bench at GSI. An early iteration of the test bench was used to prove the mechanical stability of the design as well as the tightness of the coolant seals. An attached Shack-Hartmann-Sensor was further used for qualitative measurements of the wavefront aberrations incurred by the prototype. The observed aberrations showed the formation of cylindrical lenses which could be traced to bulging of the amplifier discs under the hydrostatic pressure of the coolant. Based on this finding, an investigation was launched to develop improved retainer geometries to mitigate these deformations by the hydrostatic pressure.

The conducted research into actively cooled large aperture glass amplifiers in this thesis has thus been able to produce a scalable design for enabling the operation of large aperture optical power amplifiers at increased repetition rates. By supplementing published material data with experimental results, a coolant matching the optical, chemical and thermal requirements of such a design could be identified in the Flutec PP6 liquid by F2 Chemicals. Furthermore, with the help of simulations of the thermodynamic and hydrodynamic properties of the design, a theoretical repetition rate of $1/5\,\mathrm{min}^{-1}$ was achieved by exploiting the development of a steady state in the wavefront aberrations. While the hydrostatic deformation of the amplifier discs lead to additional deterioration of the transmitted wavefronts in the prototype, it could be shown that modifications to the retainer geometries could be used to mitigate these effects in the future.

9 Future Prospects

The results presented in this thesis have shown the theoretical viability of the proposed cooled amplifier design for increasing the repetition rate of short pulse lasers in the hundreds of Joule regime. However, further experimental validation of the design requires additional research and modifications to the existing design and the introduction of peripheral elements to reach an operational state. In the following sections the necessary modifications to the current design and test setup, the required elements to assemble an operational amplifier and the remaining tests to validate the final design will be discussed.

9.1 Design Improvements

During the experimental testing phase of the amplifier prototype a series of short-comings in the design of the prototype as well as the test bench have been discovered, which prohibited the quantitative analysis of the current prototype iteration. To improve upon the current setup, modifications of the optical test bench as well as the retainer elements of the amplifier discs are necessary.

The major improvement to the optical test bench, required to enable a quantitative analysis of the amplifiers transmitted wavefront, is the introduction of an image relaying setup to properly image the transmitted wavefront to the Shack-Hartmann sensor. The current iteration of the test bench was built with image relaying in mind but restrictions of the available physical space for the construction of the test bench lead to compromises which severly limited the quality of the image relaying setup. Therefore, input for further iterations of the prototype design as well as characterizations of the system under thermal loads requires upgrades to the image relaying system of the optical test bench.

The qualitative analysis of the transmitted wavefronts of the prototype in chapter 7.2 has shown that the combination of hydrostatic pressure by the coolant and the current configuration of retainer elements lead to the creation of a cylindrical lense. Solutions to this problem have already been discussed in chapter 7.3 but have yet to be realized on the prototype. The best solution was the continuous frame to distribute the counter force to the hydrostatic pressure evenly. However, this solution is problematic as the exertion of force on the discs from more than three points might cause bending of the discs due to an over-defintion of the support points. By distributing the force from a single primary support point to two secondary support points, as shown in figure 9.1, it is possible to support the discs at more than three points to counter the hydrostatic pressure without over-defining the supports. By stacking several of these so called *seesaw-lever force-balancing suspensions*, the support of the discs can theoretically be scaled to approximate the support by a continuous frame. The construction and implementation of such a system might prove to be necessary in countering the hydrostatic pressure inside the amplifier.

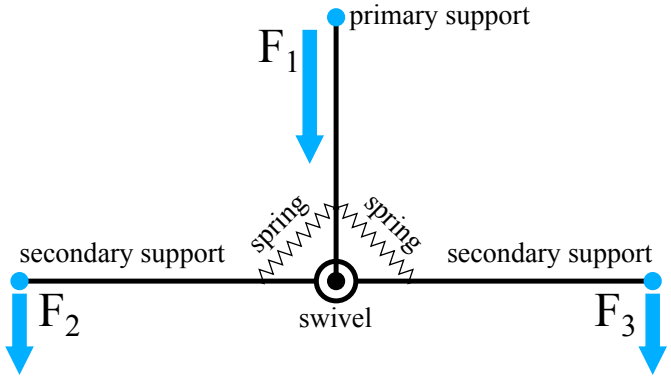

Figure 9.1: Schematic of a *seesaw-lever force-balancing suspension* for the balanced distribution of force on the discs, avoiding over-definition of the support points.

9.2 Development of Peripheral Elements

The development of the amplifier protoype during this project has produced the liquid cooled core element of an amplifier segment. To achieve an operational state of the system, further elements are needed. These elements include the development of liquid cooled flash lamps for pumping, the design and construction of the reflector geometry and housing box of the amplifier as well as the procurement and setup of the closed cooling system with reservoirs, pumps and heat exchangers.

The emitted light from the flash lamps was identified as the primary source of thermal energy for the amplifier discs. However, thermal radiation emitted by the lamps after the pump event further contributes to the heating of discs (see chp. 2.3.1).
To counter this thermal radiation, a cooling jacket around the lamps can be employed which will also be necessary to reduce the thermal load on the lamps at increased shot rates. The development of a water cooled flash lamp array has already begun at GSI with the prototype setup shown in figure 9.2. This setup features ten flash lamps in a vertical array and will be equipped with a reflector on one side and a transmission window on the other.

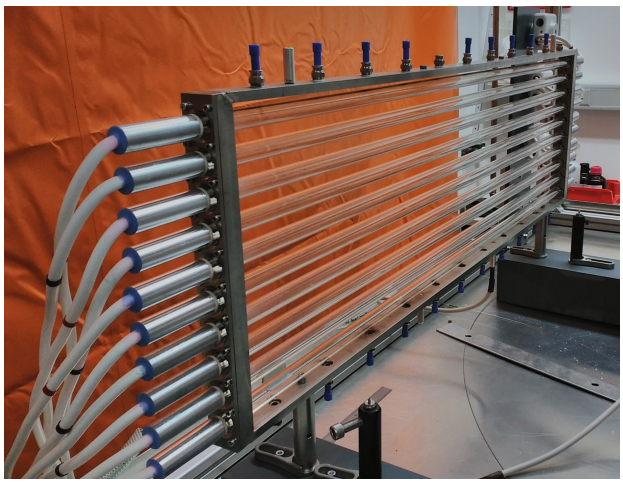

Figure 9.2: Prototype setup of the cooled flashlamps, showing an array of ten flash lamps in a single water jacket.

Water was chosen as the coolant for the flash lamps due to its high heat capacity and high absorption in the infrared range, while offering good transmission qualities at the visible wavelength regions [Kedenburg et al., 2012] required for pumping. The water will therefore provide a shield against the thermal radiation of the hot flash lamps while mitigation of the pump light will be minimal.

The light from the flash lamps is emitted over the full solid angle and has to be guided to the amplifier discs. This requires the design of a housing box for the prototype module, the flash lamps and a reflector geometry for the pump light. While earlier plans called for the use of the legacy reflector design used at PHELIX, it is very likely that the changes to the geometry of the disc mounting structure and the addition of the coolant piping will reduce the pump yield on the discs. Therefore, a mid-term redesign of the reflector geometry to optimize the pump yield would be beneficial to increasing the amplification factor of the module or reduce the strain on the flash lamps by requiring less electrical power for the optical pump.

A further addition to the current setup necessary to test the operation of the cooling system is the implementation of the closed coolant cycle. The schematic in figure 4.8 depicts the basic setup of such a system. While some early investigations of the requirements of the heat exchanger as well as the thermal control unit for driving the coolant temperature profile have been conducted, further development of the coolant supply system is needed to achieve operational status.

9.3 Validation Tests

To reach a conclusion about the performance of the developed liquid cooled amplifier system, tests will have to be performed to determine the cooling behaviour and thus the repetition rate of the system, the amplification gain of the prototype design as well as the transmission behaviour of the fully assembled setup.
A prerequisite to these tests is the optimization of the optical test bench at PHELIX to enable quantitative analysis of the transmitted wavefronts. Using the optical test bench in combination with an artificial heat source, the thermo-optic behaviour of the prototype can be investigated prior to the implementation of the reflectors and flash lamps. However, a realistic measurement of the achievable repetition rate requires the completed configuration since the thermal distribution in the discs depends on the topology of the incomming pump light which will be difficult to emulate using artificial heat sources.
Once the implementation of the flash lamps and reflectors is completed, further testing of the amplification gain and transmission behaviour of the prototype can commence.
One concern with the current design are the reflections at the media interfaces which might cause pre- and post-pulses in the laser. These pre-pulses could be especially problematic for applications sensitive to the temporal contrast of the laser pulse. One possible solution to reduce the reflections would be wedged amplifier discs which would require a more complex manufacturing process and would thus lead to increased costs of the system.
A second concern are the transmission losses by the reflections and absorption in the coolant. These losses could necessitate an adjustment of the pump power of the flash lamps to compensate for the reduction in the effective gain.

Thus, measurements of the wavefront evolution over several pulses, the temporal contrast of the pulses as well as the amplification gain will have to be conducted to validate the prototype for implementation at PHELIX as well as for further operation at the 100 J diagnostic laser and the Helmholtz beamline.

Acknowledgements

Zuerst möchte ich mich bei **Prof. Dr. Markus Roth** für die Aufnahme in seiner Arbeitsgruppe bedanken. Er gab mir die Möglichkeit auf einem für mich völlig neuen und interessanten Thema für meine Promotion zu arbeiten sowie durch sein Netzwerk Kontakte zu knüpfen, welche mir neue Möglichkeiten für meine zukünftige Laufbahn eröffnet haben. Dafür vielen Dank!

Außerdem möchte ich mich bei **Priv. Doz. Dr. Vincent Bagnoud** bedanken, dass er mich in seine Arbeitsgruppe an der GSI aufgenommen hat und mir den Zugang zu Ressourcen der GSI ermöglichte. Insbesondere der Zugang zu CADFEM ANSYS sowie die Nutzung von PHELIX Ressourcen für den Bau des Refraktometers waren von großem Wert für mein Projekt.

Eine weitere große Unterstützung für meine Arbeit war **Dr. Bernhard Zielbauer**, welcher mir mit seiner Betreuung und Rat geholfen hat mich in ein mir unbekanntes Feld einzuarbeiten. Des Weiteren war seine Hilfe essentiell beim Aufbau des optischen Teststands für den Prototypen.

Jonas Benjamin Ohland möchte ich ebenfalls für seine Hilfe danken. Er half mir die Eigenschaften von Wellenfronten zu verstehen und die Analyse der simulierten Wellenfronten mit WOMBAT durchzuführen.

Ein spezieller Dank gilt **Prof. Dr. Christian Hess** und **Dr. Christian Schilling** vom **Eduard-Zintl-Institut für Anorganische und Physikalische Chemie** der Technischen Universität Darmstadt. Ihre Hilfe bei der Untersuchung der Absorptionseigenschaften der Kühlmittel mit ihrem Photospektrometer waren von unschätzbarem Wert für die Wahl des Kühlmittels und der Abschätzung der Transmissionseigenschaften des Verstärkers.

Ebenfalls möchte ich der gesamten **Plasmaphysik Gruppe der GSI** und insbesondere dem **PHELIX Team** für ihre Unterstützung bei verschiedensten Fragen zu Lasern und Plasmen sowie einem tollen kollegialen Verhältnis danken.
Selbiges gilt für die gesamte Arbeitsgruppe von Professor Roth, welche mir trotz meines abgekapselten Themas immer wieder mit hilfreichen Tipps und netter Gesellschaft zur Seite stand.

Ein ebenfalls großer Danke geht an das **Bundesministerium für Bildung und Forschung**, ohne dessen Förderung die Umsetzung dieses Projektes nicht machbar gewesen wäre.

Als letztes möchte ich noch meiner Familie und meinen Freunden danken, welche trotz der stressigen Zeit meiner Promotion stets zu mir gehalten haben und mir mit ihrer emotionalen Unterstützung geholfen haben, dieses Projekt zu seinem vorläufigen Ende zu führen.
Insbesondere gilt dabei mein Dank meinen Korrekturlesern **Simone Aumüller**, **Diana Jahn**,

Jonas Benjamin Ohland, **Martin Schanz**, **Annika Kleinschmidt**, **Jan-Paul Hucka** und **Sharlen Smith**.

Bibliography

[Abbe, 1906] Abbe, E. (1906). *Gesammelte Abhandlungen*, volume 2. Gustav Fischer Verlag.

[Bagnoud et al., 2010] Bagnoud, V., Aurand, B., Blazevic, A., Borneis, S., Bruske, C., Ecker, B., Eisenbarth, U., Fils, J., Frank, A., Gaul, E., et al. (2010). Commissioning and early experiments of the PHELIX facility. *Applied Physics B*, 100(1):137–150.

[Blanchot et al., 2013] Blanchot, N., Behar, G., Berthier, T., Busserole, B., Chappuis, C., Damiens-Dupont, C., Garcia, P., Granet, F., Grosset-Grange, C., Goossens, J.-P., et al. (2013). Overview of PETAL, the multi-petawatt project in the LMJ facility. In *EPJ Web of Conferences*, volume 59, page 07001. EDP Sciences.

[Blanchot et al., 1995] Blanchot, N., Rouyer, C., Sauteret, C., and Migus, A. (1995). Amplification of sub-100-tw femtosecond pulses by shifted amplifying nd: glass amplifiers: theory and experiments. *Optics letters*, 20(4):395–397.

[Born et al., 1999] Born, M., Wolf, E., Bhatia, A. B., Clemmow, P. C., Gabor, D., Stokes, A. R., Taylor, A. M., Wayman, P. A., and Wilcock, W. L. (1999). *Principles of Optics: Electromagnetic Theory of Propagation, Interference and Diffraction of Light*. Cambridge University Press, 7 edition.

[Brown, 1981] Brown, D. C. (1981). *High-Peak-Power Nd:Glass Laser Systems*. Springer Series in Optical Sciences. Springer-Verlag.

[Bulanov et al., 2011] Bulanov, S. V., Esirkepov, T. Z., Hayashi, Y., Kando, M., Kiriyama, H., Koga, J. K., Kondo, K., Kotaki, H., Pirozhkov, A. S., Bulanov, S. S., Zhidkov, A. G., Rosanov, N. N., Chen, P., Neely, D., Kato, Y., Narozhny, N. B., and Korn, G. (2011). Extreme field science. *Plasma Physics and Controlled Fusion*, 53(12):124025.

[Cargille, 2018] Cargille (2018). *Immersion Liquid Code S1050*. Cargille Laboratories.

[Cavailler et al., 2004] Cavailler, C., Fleurot, N., Lonjaret, T., and Di-Nicola, J.-M. (2004). Prospects and progress at LIL and Megajoule. *Plasma Physics and Controlled Fusion*, 46(12B):B135.

[Celliers et al., 2004] Celliers, P., Bradley, D., Collins, G., Hicks, D., Boehly, T., and Armstrong, W. (2004). Line-imaging velocimeter for shock diagnostics at the OMEGA laser facility. *Review of scientific instruments*, 75(11):4916–4929.

[Celliers et al., 2018] Celliers, P. M., Millot, M., Brygoo, S., McWilliams, R. S., Fratanduono, D. E., Rygg, J. R., Goncharov, A. F., Loubeyre, P., Eggert, J. H., Peterson, J. L., et al. (2018). Insulator-metal transition in dense fluid deuterium. *Science*, 361(6403):677–682.

[Crane et al., 2010] Crane, J., Tietbohl, G., Arnold, P., Bliss, E., Boley, C., Britten, G., Brunton, G., Clark, W., Dawson, J., Fochs, S., et al. (2010). Progress on converting a NIF quad to eight, petawatt beams for advanced radiography. In *Journal of Physics: Conference Series*, volume 244, page 032003. IOP Publishing.

[Daiber et al., 1966] Daiber, J. W., Hertzberg, A., and Wittliff, C. E. (1966). Laser-generated implosions. *The Physics of Fluids*, 9(3):617–619.

[Danson et al., 1998] Danson, C., Collier, J., Neely, D., Barzanti, L., Damerell, A., Edwards, C., Hutchinson, M., Key, M., Norreys, P., Pepler, D., et al. (1998). Well characterized 10^{19} W cm^2 operation of VULCAN—an ultra-high power Nd: glass laser. *Journal of modern optics*, 45(8):1653–1669.

[Danson et al., 2015] Danson, C., Hillier, D., Hopps, N., and Neely, D. (2015). Petawatt class lasers worldwide. *High Power Laser Science and Engineering*, 3:e3.

[Driggers, 2003] Driggers, R. G. (2003). *Encyclopedia of Optical Engineering: Las-Pho, pages 1025-2048*, volume 2. CRC press.

[Dubrovinsky et al., 2012] Dubrovinsky, L., Dubrovinskaia, N., Prakapenka, V. B., and Abakumov, A. M. (2012). Implementation of micro-ball nanodiamond anvils for high-pressure studies above 6 Mbar. *Nature communications*, 3:1163.

[Elton, 2012] Elton, R. C. (2012). *X-ray Lasers*. Elsevier.

[Fieberg, 2014] Fieberg, S. A. (2014). *Analyse thermooptischer Effekte zur Absorptionsmessung*. PhD thesis, Albert-Ludwigs-Universität Freiburg im Breisgau.

[Fortov, 2010] Fortov, V. E. (2010). *Extreme States of Matter: on Earth and in the Cosmos*. Springer Science & Business Media.

[Frantz and Nodvik, 1963] Frantz, L. M. and Nodvik, J. S. (1963). Theory of Pulse Propagation in a Laser Amplifier. *Journal of Applied Physics*, 34(8):2346–2349.

[Gaul et al., 2018] Gaul, E., Chériaux, G., Antipenkov, R., Batysta, F., Borger, T., Friedman, G., Greene, J., Hammond, D., Heisler, J., Hidinger, D., Jochmann, A., Kepler, M., Kissinger, A., Kramer, D., Lagron, J., Meadows, A., Rus, B., Trojek, P., Vyhlídka, S., and Ditmire, T. (2018). Hybrid OPCPA/Glass 10 PW laser at 1 shot a minute. In *Conference on Lasers and Electro-Optics*, page STu3M.2. Optical Society of America.

[Graziani et al., 2014] Graziani, F., Desjarlais, M. P., Redmer, R., and Trickey, S. B. (2014). *Frontiers and challenges in warm dense matter*, volume 96. Springer Science & Business.

[Hale and Querry, 1973] Hale, G. M. and Querry, M. R. (1973). Optical Constants of Water in the 200-nm to 200-μm Wavelength Region. *Appl. Opt.*, 12(3):555–563.

[Hemingway, 2002] Hemingway, P. (2002). n-Simplex interpolation. *HP Laboratories Bristol, HPL-2002*, 320:1–8.

[Hu et al., 2014] Hu, L., Chen, S., Tang, J., Wang, B., Meng, T., Chen, W., Wen, L., Hu, J., Li, S., Xu, Y., and et al. (2014). Large aperture N31 neodymium phosphate laser glass for use in a high power laser facility. *High Power Laser Science and Engineering*, 2:e1.

[Jackson and Witte, 2006] Jackson, J. D. and Witte, C. (2006). *Klassische Elektrodynamik; 4th rev. version*. De Gruyter, Berlin.

[Kedenburg et al., 2012] Kedenburg, S., Vieweg, M., Gissibl, T., and Giessen, H. (2012). Linear refractive index and absorption measurements of nonlinear optical liquids in the visible and near-infrared spectral region. *Opt. Mater. Express*, 2(11):1588–1611.

[Kitagawa et al., 2004] Kitagawa, Y., Fujita, H., Kodama, R., Yoshida, H., Matsuo, S., Jitsuno, T., Kawasaki, T., Kitamura, H., Kanabe, T., Sakabe, S., Shigemori, K., Miyanaga, N., and Izawa, Y. (2004). Prepulse-free petawatt laser for a fast ignitor. *IEEE Journal of Quantum Electronics*, 40(3):281–293.

[Knudson et al., 2015] Knudson, M. D., Desjarlais, M. P., Becker, A., Lemke, R. W., Cochrane, K., Savage, M. E., Bliss, D. E., Mattsson, T., and Redmer, R. (2015). Direct observation of an abrupt insulator-to-metal transition in dense liquid deuterium. *Science*, 348(6242):1455–1460.

[Koechner, 1999] Koechner, W. (1999). *Solid-State Laser Engineering*. Springer Series in Optical Sciences. Springer-Verlag, 5th edition.

[Kritcher et al., 2014a] Kritcher, A., Döppner, T., Swift, D., Hawreliak, J., Collins, G., Nilsen, J., Bachmann, B., Dewald, E., Strozzi, D., Felker, S., et al. (2014a). Probing matter at Gbar pressures at the NIF. *High Energy Density Physics*, 10:27–34.

[Kritcher et al., 2014b] Kritcher, A., Döppner, T., Swift, D., Hawreliak, J., Collins, G., Nilsen, J., Bachmann, B., Dewald, E., Strozzi, D., Felker, S., et al. (2014b). Probing matter at Gbar pressures at the NIF. *High Energy Density Physics*, 10:27–34.

[Li et al., 2018] Li, M., Wang, B., Wang, X., Yang, X., Chen, D., Chen, W., and Hu, L. (2018). Water corrosion of commercial neodymium-doped phosphate high-peak-power laser glass. *Journal of Non-Crystalline Solids*, 496:34 – 41.

[Lines, 1993] Lines, M. E. (1993). Physical origin of the temperature dependence of chromatic dispersion in fused silica. *Journal of Applied Physics*, 73(5):2075–2079.

[Maiman, 1960] Maiman, T. H. (1960). Optical and Microwave-Optical Experiments in Ruby. *Phys. Rev. Lett.*, 4:564–566.

[Mayor and Queloz, 1995] Mayor, M. and Queloz, D. (1995). A jupiter-mass companion to a solar-type star. *Nature*, 378(6555):355.

[Meschede et al., 2015] Meschede, D. et al. (2015). *Gerthsen Physik*, volume 25. Springer.

[Miller et al., 2004] Miller, G. H., Moses, E. I., and Wuest, C. R. (2004). The National Ignition Facility: enabling fusion ignition for the 21st century. *Nuclear Fusion*, 44(12):S228.

[Musgrave et al., 2013] Musgrave, I., Boyle, A., Carroll, D., Clarke, R., Heathcote, R., Galimberti, M., Green, J., Neely, D., Notley, M., Parry, B., et al. (2013). Recent developments on the vulcan high power laser facility. In *High-Power, High-Energy, and High-Intensity Laser Technology; and Research Using Extreme Light: Entering New Frontiers with Petawatt-Class Lasers*, volume 8780, page 878003. International Society for Optics and Photonics.

[Neumayer et al., 2014] Neumayer, P., Rosmej, O., Jacoby, J., Blazevic, A., Roth, M., Ulrich, A., and Spielmann, C. (2014). Fair technical design report: Diagnostic instrumentation for plasma physics experiments at the APPA cave. In *Tech. Rep. (HEDge-HOB Collaboration, 2014)*.

[Noll, 1976] Noll, R. J. (1976). Zernike polynomials and atmospheric turbulence∗. *J. Opt. Soc. Am.*, 66(3):207–211.

[Nye, 1957] Nye, J. F. (1957). *Physical properties of crystals : their representation by tensors and matrices / by J.F. Nye*. Clarendon Oxford.

[OHARA, 2017] OHARA (2017). *OHARA Optical Glass - Technical Information*. Ohara GmbH.

[Ohland, 2018] Ohland, J. B. (2018). Improvement of the Adaptive Optics at PHELIX for Operation at higher Repetition Rates and Investigation of Laguerre-Gaussian-like Modes. Master's thesis, Technical University Darmstadt.

[Otanicar et al., 2009] Otanicar, T. P., Phelan, P. E., and Golden, J. S. (2009). Optical properties of liquids for direct absorption solar thermal energy systems. *Solar Energy*, 83(7):969 – 977.

[Park et al., 2008] Park, H.-S., Maddox, B., Giraldez, E., Hatchett, S., Hudson, L., Izumi, N., Key, M., Le Pape, S., MacKinnon, A., MacPhee, A., et al. (2008). High-resolution 17–75 keV backlighters for high energy density experiments. *Physics of Plasmas*, 15(7):072705.

[Perry et al., 1999] Perry, M., Pennington, D., Stuart, B., Tietbohl, G., Britten, J., Brown, C., Herman, S., Golick, B., Kartz, M., Miller, J., et al. (1999). Petawatt laser pulses. *Optics letters*, 24(3):160–162.

[Rosmej et al., 2019] Rosmej, O., Andreev, N., Zaehter, S., Zahn, N., Christ, P., Borm, B., Radon, T., Sokolov, A., Pugachev, L., Khaghani, D., et al. (2019). Interaction of relativistically intense laser pulses with long-scale near critical plasmas for optimization of laser based sources of MeV electrons and gamma-rays. *New Journal of Physics*, 21(4):043044.

[Roth et al., 2013] Roth, M., Jung, D., Falk, K., Guler, N., Deppert, O., Devlin, M., Favalli, A., Fernandez, J., Gautier, D., Geissel, M., Haight, R., Hamilton, C. E., Hegelich, B. M., Johnson, R. P., Merrill, F., Schaumann, G., Schoenberg, K., Schollmeier, M., Shimada, T., Taddeucci, T., Tybo, J. L., Wagner, F., Wender, S. A., Wilde, C. H., and Wurden, G. A. (2013). Bright Laser-Driven Neutron Source Based on the Relativistic Transparency of Solids. *Phys. Rev. Lett.*, 110:044802.

[Rotta, 1956] Rotta, J. v. (1956). Experimenteller Beitrag zur Entstehung turbulenter Strömung im Rohr. *Archive of Applied Mechanics*, 24(4):258–281.

[Rouyer et al., 1993] Rouyer, C., Mazataud, E., Allais, I., Pierre, A., Seznec, S., Sauteret, C., Mourou, G., and Migus, A. (1993). Generation of 50-TW femtosecond pulses in a Ti: sapphire/Nd: glass chain. *Optics letters*, 18(3):214–216.

[Sazegari et al., 2010] Sazegari, V., Milani, M. R. J., and Jafari, A. K. (2010). Structural and optical behavior due to thermal effects in end-pumped Yb:YAG disk lasers. *Appl. Opt.*, 49(36):6910–6916.

[Schawlow and Townes, 1958] Schawlow, A. L. and Townes, C. H. (1958). Infrared and Optical Masers. *Phys. Rev.*, 112:1940–1949.

[Slack, 1964] Slack, G. A. (1964). Thermal conductivity of pure and impure silicon, silicon carbide, and diamond. *Journal of Applied Physics*, 35(12):3460–3466.

[Snavely et al., 2000] Snavely, R., Key, M., Hatchett, S., Cowan, T., Roth, M., Phillips, T., Stoyer, M., Henry, E., Sangster, T., Singh, M., et al. (2000). Intense high-energy proton beams from petawatt-laser irradiation of solids. *Physical review letters*, 85(14):2945.

[Spiller et al., 2008] Spiller, P., Blell, U., Boine-Frankenheim, O., Fischer, E., Franchetti, G., Hagenbuck, F., Hofmann, I., Kauschke, M., Kaugarts, J., Kirk, M., et al. (2008). Design status of the FAIR synchrotrons SIS100 and SIS300 and the high energy beam transport system. In *Proc. of the 11th Eur. Particle Accelerator Conf., June 23-27*, pages 298–300.

[Stokowski et al., 1981] Stokowski, S. E., Saroyan, R. A., and Weber, M. J. (1981). Nd:doped laser glass spectroscopic and physical properties. *Lawrance Livermore Natural Laboratory Report M-095 (Rev.2)*.

[Strickland and Mourou, 1985] Strickland, D. and Mourou, G. (1985). Compression of amplified chirped optical pulses. *Optics Communications*, 55:447–449.

[Suratwala et al., 2000] Suratwala, T., Steele, R., Wilke, G., Campbell, J., and Takeuchi, K. (2000). Effects of OH content, water vapor pressure, and temperature on sub-critical crack growth in phosphate glass. *Journal of Non-Crystalline Solids*, 263-264:213 – 227.

[Tahir et al., 2019a] Tahir, N. A., Neumayer, P., Shutov, A., Piriz, A. R., Lomonosov, I. V., Bagnoud, V., Piriz, S. A., and Deutsch, C. (2019a). Equation-of-state studies of high-energy-density matter using intense ion beams at the Facility for Antiprotons and Ion Research. *Contributions to Plasma Physics*, 59(4-5):e201800143.

[Tahir et al., 2019b] Tahir, N. A., Shutov, A., Piriz, A. R., Neumayer, P., Lomonosov, I. V., Bagnoud, V., and Piriz, S. A. (2019b). Application of intense ion beams to planetary physics research at the Facility for Antiprotons and Ion Research facility. *Contributions to Plasma Physics*, 59(4-5):e201800135.

[Tajima and Dawson, 1979] Tajima, T. and Dawson, J. M. (1979). Laser electron accelerator. *Physical Review Letters*, 43(4):267.

[Tateno et al., 2010] Tateno, S., Hirose, K., Ohishi, Y., and Tatsumi, Y. (2010). The structure of iron in Earth's inner core. *Science*, 330(6002):359–361.

[van Thiel et al., 1966] van Thiel, M., Kusubov, A., and Mitchell, A. (1966). Compendium of shock wave data Lawrence Radiat. *Lab., Livermore, Rep. UCRL-50108*.

[Varentsov et al., 2016] Varentsov, D., Antonov, O., Bakhmutova, A., Barnes, C., Bogdanov, A., Danly, C., Efimov, S., Endres, M., Fertman, A., Golubev, A., et al. (2016). Commissioning of the PRIOR proton microscope. *Review of Scientific Instruments*, 87(2):023303.

[Vargaftik, 1975] Vargaftik, N. (1975). Handbook of physical properties of liquids and gases - pure substances and mixtures. Second edition.

[von Zernike, 1934] von Zernike, F. (1934). Beugungstheorie des Schneidenverfahrens und seiner verbesserten Form, der Phasenkontrastmethode. *Physica*, 1(7):689 – 704.

[Wang et al., 2012] Wang, X., Fan, Z., Yu, J., Shi, Z., Zhao, T., Wang, P., Kang, Z., Lian, F., Huang, Y., and Tang, X. (2012). High Energy, High Efficiency Nd: Glass Regenerative Amplifier. In *Optical, Electronic Materials and Applications II*, volume 529 of *Advanced Materials Research*, pages 105–109. Trans Tech Publications Ltd.

[Wyant and Creath, 1992] Wyant, J. C. and Creath, K. (1992). Basic Wavefront Aberration Theory for Optical Metrology. *Applied optics and optical engineering*, 11.

List of Abbreviations

APPA	Atomic Plasma Physics and Applications.
CPA	Chirped Pulse Amplification.
FAIR	Facility for Anti-proton and Ion Research.
GSI	GSI Helmholtzzentrum für Schwerionenforschung GmbH in Darmstadt.
HIHEX	Heavy Ion Heating and Expansion.
ICF	Inertial Confinement Fusion.
IR	Infrared.
LAPLAS	Laboratory Planetary Sciences.
LED	Light Emitting Diode.
LMJ	Laser Mégajoule.
NIF	National Ignition Facility.
PHELIX	Petawatt High-Energy Laser for heavy Ion Experiments.
PRIOR	Proton Microscope for FAIR Facility for Anti-proton and Ion Research.
SIOM	Shanghai Institute of Fine Mechanics.
UV	Ultraviolet.
WDM	Warm Dense Matter.
WOMBAT	Wavefront Optics Measurement and Beam Analysis Tool.
YAG	Yttrium Aluminium Garnet.
cw	continuous wave.

List of Figures

2.1 Energy level structure of the two archetypes of electron configurations for gain media. . . . 14
2.2 Energy levels and transitions in Nd^{3+} [Brown, 1981]. . . . 17
2.3 Example of an emitted spectrum for a xenon flash lamp at current densities of 1, 2 and 3 kA/cm^2 [Brown, 1981], showing the transition from a line dominated spectrum to a black body dominated spectrum with increasing current densities. . . 19

3.1 Conduction of thermal energy from a hot to a cold area of equal size. . . . 22
3.2 Examples of two wavefronts with various wavefront features. . . . 27
3.3 Seidel aberrations of the wavefront with their associated functional terms and wavefront profiles. . . . 28
3.4 Plots of the first 10 Zernike aberrations for the $|R_n^m(1)| = 1$ normalization with their names, polynomial representation and Noll index [Ohland, 2018]. . . . 29

4.1 Concept of a thin amplifier disc with the coolant in the transmission plane of the laser. . . . 32
4.2 Tow split disc configurations for a total disc thickness of 5 cm, approximating the thickness of the current PHELIX amplifier discs. . . . 33
4.3 Fluid-dynamics simulation of cooling fluids between two amplifier discs using CADFEM ANSYS CFX module on varying coolant flow setups. At this stage no suitable coolant had been identified yet and all simulations were conducted using water as a place holder fluid. . . . 35
4.4 Schematic of the prototype module's central frame with its cutouts for the glass and coolant cavity ①, the nozzle and reservoir cavities ② as well as mountings for coolant seals ③ and retainer clamps ④. . . . 36
4.5 Schematic of the nozzle block with attached cavity spacers ①, nozzles ② with 10 mm separation, attached anti-settling spacers ③ for the bottom nozzle block and the O-ring groove ④ for sealing. . . . 37
4.6 Horizontal shift of the beam due to refraction at ambient-glass and glass-coolant interfaces. . . . 38
4.7 Schematics of the designed sealing solution to contain the coolant in the cavity between the amplifier discs while reducing the stresses on the glass. . . . 40
4.8 Flow diagram of the coolant supply featuring the elevated coolant supply tank ①, the amplifier module ②, the coolant drainage tank ③, the pump ④ to recirculate the coolant and a heat exchanger ⑤ to resupply cool liquid to the supply tank. . . 41

5.1 Excerpt of the measured absorption spectra for various liquids around the targeted laser wavelength of 1053 nm, denoted by the vertical line. Measurements performed with the Jasco V-770 UV-Visible/NIR Spectrophotometer at the Eduard-Zintl-Institut für Anorganische Chemie und Physikalische Chemie. Absorption accuracy specified as $\pm 0.0035\,\mathrm{cm}^{-1}$ between 0 and $1.15\,\mathrm{cm}^{-1}$. 48
5.2 Reflectance at the interface of two media with $n_i > n_t$ with the Brewster angle (red) and the critical angle for total reflection (orange). 49
5.3 Preliminary considerations on the setup and material choices for a total internal reflection refractometer. 50
5.4 Experimental setup of the total internal reflection refractometer consiting of a small cw-laser at 1053 nm ①, two mirrors ② & ③ to adjust the pointing of the beam, the prism with the attached reservoir ④ mounted to a rotating stage, a second rotating stage ⑤ to adjust the position of the detector and an arm holding the detector ⑥. 51
5.5 Angles and relations in the plan-parallel setup of the glass discs and cooling liquid. 53
5.6 Transmittance of the amplifier for a fluid layer of 1.5 mm and wavelength of 1053 nm. Transmittance calculated from (5.11) using absorption data from fig. 5.1 and refraction data from tab. 5.2. The Brewster angle of the amplifier glass with air is denoted as a grey line. 54

6.1 Temperature profile of the coolant and its impact on the cooling time in one-dimensional simulations of the amplifier setup. 58
6.2 Temperature maps of the coolant and the glass, showing the gradual heating of the coolant and its effect on the cooling process of the amplifier discs. 61
6.3 Evolution of the maximum temperature differentials observed in the glass discs over consecutive cooling cycles. Pump event occurs every 300 seconds. 62
6.4 Wavefronts derived from the simulated temperature distributions of a single ten minute cooling phase showing the difference between passive and active cooling on the wavefront evolution. 64
6.5 Difference profiles between the phase shifts at the end of various cooling cycles during a $1/5\,\mathrm{min}^{-1}$ repetition rate simulation, showing the development of a steady state previously observed in figure 6.3. 65
6.6 Evolution of Zernike aberrations caused by simulated thermal distributions in repeatedly pumped glass discs with pump events every 300 s. 66
6.7 Comparison of the different exposure paths of the coolant to the heated glass in the central and side regions of the elliptical thermal distribution. 67

7.1 Setup for testing the seal tightness, with the water supply reservoir ① elevated above the prototype ② for the hydrostatic feeding of water. Further shown are the drainage tank ③ below the prototype module and the spill basin ④. 69
7.2 Different compression states of the red O-ring seal around the glass discs during assembly. Visibility of the O-ring is used as indication for contact between the seal and the glass. 70
7.3 Test bench setup showing the general setup with the prototype and the optical setup for the wavefront analysis. 72

7.4 Simulated deformations of the glass discs under pressure from the coolant and ambient atmosphere using the retainer configuration of the prototype (fig. 7.5a). 74
7.5 Retainer setups investigated to understand and improve the disc deformation due to hydrostatic pressure. 75
7.6 Simulated deformations of the glass discs showing the reduction of deformation magnitude by using modified retainer geometries. 77

9.1 Schematic of a *seesaw-lever force-balancing suspension* for the balanced distribution of force on the discs, avoiding over-definition of the support points. 82
9.2 Prototype setup of the cooled flashlamps, showing an array of ten flash lamps in a single water jacket. 82

List of Tables

5.1 Volumetric heat capacity, required exchange volume, viscosity, estimated flow velocity in the cavity of the amplifier and the resulting Reynold's number. 45
5.2 Compilation of measured refractive indices and literature data 52

Curriculum Vitae

Personal Data

Name	Marco Patrizio
Date, place of birth	20.12.1988, Hanau
Nationality	german

Education

Apr 2013 - Mar 2016	Technische Universität Darmstadt & Deutsches Zentrum für Luft- und Raumfahrt M.Sc. in Physics, ø1.8 Thesis title: Upgrade des Programms IMD zur Simulation von Laser-Materie Wechselwirkung
Oct 2008 - Apr 2013	Technische Universität Darmstadt B.Sc. in Physics, ø2.9 Thesis title: Charakterisierung eines orts- und energieauflösenden Silizium Detektors
Sep 1999 - Jul 2008	Kopernikusschule Freigericht Abitur: ø2.3

Professional Experience

Apr 2010 - Oct 2018	Tutor for the physical laboratory training (Grundpraktikum) at Technische Universität Darmstadt

Conferences

May 2019	Conference on Lasers and Electro-Optics, San José, California, USA
Sep 2018	8th Conference of the International Committee on Ultrahigh Intensity Lasers, Lindau, Germany
Feb 2018	38th International Workshop on High Energy Density Physics with Intense Ion and Laser Beams, Hirschegg, Austria
Feb 2017	37th International Workshop on High Energy Density Physics with Intense Ion and Laser Beams, Hirschegg, Austria
Nov 2016	Laserlab Meeting on Innovative Laser Technologies, Dolní Břežany, Czech Republic